UNIVERSITY OF CALIFORNIA
SANTA CRUZ

Understanding Fault Damage and Slip with Marine Seismic Methods

A dissertation submitted in partial satisfaction
of the requirements for the degree of

DOCTOR OF PHILOSOPHY

in

EARTH SCIENCES

by

Travis Alongi

December 2023

The Dissertation of Travis Alongi is approved:

_____
Professor Emily E. Brodsky

_____
Professor Susan Y. Schwartz

_____
Professor Heather Savage

_____
Research Geophysicist Jared Kluesner

_____
Peter Biehl
Vice Provost and Dean of Graduate Studies

Table of Contents

List of Figures

Abstract

Understanding Fault Damage and Slip with Marine Seismic Methods

Travis Alongi

Over nearly a century, seismology has provided valuable earthquake observation and information. The locations of earthquake hypocenters have helped define the spatial distribution of faults that host earthquakes and helped identify regions that may have large and damaging events in the future. However, exactly how aseismic slip, small earthquakes, and smaller faults are related to large events and the seismic cycle remains unresolved. Recent advances in instrumentation have extended research into the oceanic realm, which is important for at least two reasons. First, it enables the detection of ever smaller earthquakes that provide information about slip behavior on offshore portions of previously unresolved faults. Second, with ever-increasing resolution, marine seismic reflection images provide increasingly precise depictions of fault zones that are unattainable in the terrestrial environment. This dissertation is dedicated to better understanding the spatial distribution of faults and their potential to influence slip behavior and seismic cycle through the use of marine seismic methods. It encompasses two distinct facets of marine seismology: passive recording of earthquakes and the interrogation of subsurface faulting through seismic reflection imaging. These dual areas of investigation offer unique insights into the subsurface structure and the interplay of seismic and aseismic processes.

Chapter 1 explores the enigmatic plate interface in southernmost Cascadia with the application of a dense array of ocean-bottom seismometers complementing traditional

terrestrial seismic stations. A high-quality seismic catalog is created through the meticulous analysis of continuous waveform data and advanced earthquake location techniques. The results reveal a conspicuous absence of seismic activity at seismogenic depths and the shallowest up dip section, indicative of high coupling or locking and strain accumulation increasing the magnitude potential associated with this fault. Notably, a cluster of low-magnitude earthquakes ($M < 3$) is identified near the plate interface, exhibiting a response to nearby strain transient observed in prior studies. These strain transients are interpreted as either the tail end of a slow slip event spanning the preceding one and a half years or a rapid change in coupling. Template matching of these plate interface earthquakes demonstrates their uniqueness, with no recurrence over the observed decade. The correlation between the sudden onset of clustered earthquake activity and strain transient suggests that the two are related, and the interpretation is made that the cluster of earthquakes is a response to local stressing rate changes. Chapter 1 provides critical insights into the southern Cascadia plate interface, shedding light on the complex interactions between seismic behavior and slow slip events.

In Chapters 2 and 3, this dissertation examines the shallow near-surface portion of the fault zone, with a specific focus on the spatial distribution of secondary faults surrounding the primary fault. This damaged area around the main fault provides an important window into comprehending the inelastic response of the Earth's crust to strain, the allocation of fracture energy in the earthquake energy budget, near-fault hydrogeology, and for near-field hazards. The dimensions, both in width and depth of

the damage zone are important in addressing these science questions. The primary objective of these two studies is to gain insight on the in-situ expression of the fault damage with marine controlled source seismic reflection images, an approach which had not been fully explored prior. The advantage of this data type lies in its ability to provide rich and dense sampling of the subsurface and the capability to directly image fault offsets over substantial distances that are often unattainable through other means. To achieve a comprehensive understanding of the damage zone, ranging from the seafloor to the basement, roughly 2 kilometers below, marine active source reflection surveys of varying resolutions are employed. Both Chapters 2 and 3 focus on the San Pedro Shelf region of the Palos Verdes Fault offshore southern California because of the richness in available reflection datasets and the opportunity to address unanswered questions about the generation of fault damage.

Chapter 2 focuses on examining the damage zone of the Palos Verdes Fault using 2 overlapping 3D seismic volumes and demonstrates the development of a workflow for automating fault detections. Automation is achieved through the implementation of multi-trace waveform similarity or semblance-based attribute called thinned fault likelihood (TFL). These results reveal peak fault likelihoods at the location of mapped fault strands, with fault likelihood exponentially decaying with distance from the fault. Importantly, this decay with distance intersects a relatively undamaged region or background at 2 kilometers from the fault across all depths (ranging from 450 m to 2.2 km). Lithological constraints are provided by well tied 3D horizons, and damage decay trends are for each geologic unit. Notably, the findings indicate an

overall increase in background damage with increasing depth. In addition to background damage increasing with depth, it is demonstrated that the decay of damage also decreases with increasing depth. This surprisingly, results in a consistent damage zone width of 2 kilometers regardless of the variability in background damage and decay trends.

Chapter 3 investigates the shallowest portion of the Palos Verdes Fault damage zone which could not be fully explored in Chapter 2. This section leverages newly collected 2D high-resolution sparker multichannel seismic lines and sub-bottom profiles (chirp). Resolving the challenges of imaging in shallow water profiles is achieved through the development of custom seismic processing workflows designed to eliminate the ringing and overprinting of seismic waves trapped in the water column. Similar to Chapter 2, a semblance-based technique is used to identify discontinuities in the seismic images associated with faults and fractures. The analysis of fault perpendicular TFL profiles yields a diverse pattern of damage in the vicinity of the fault on adjacent profiles. In this study we define and map the active fault strand determined by the offset of the near seafloor sediment beds. An average pattern of damage decreasing with distance from the fault is shown by stacking fault perpendicular profiles with respect to the active fault. The stacked profiles reveal that damage decreases with distance both east and west of the fault. Notably, the peak of stacked fault damage occurs within roughly 50 meters of the active fault strand, with splay faults manifesting as secondary peaks in the stacked results. The width of the damage zone along the slope appears to align with power law displacement scaling

relationships established by previous compilation studies. However, the significant reduction in damage zone width and intensity towards the south may be better attributed to the reduced obliquity of fault in that direction. In contrast to canonical strike-slip models, the presented data suggests compelling evidence that the damage zone does not widen as it approaches the surface, a characteristic that may distinguish syndepositional submarine fault's structure. Furthermore, there is an apparent correlation between fault damage and seafloor seeps that are visibly evident in the water column. This correlation strongly implies that damage plays a role in controlling fluid flow around the fault.

Dedication

In the loving memory of my father, Mark Alongi, whose unwavering support, and boundless belief in my potential continue to motivate me, even in his absence. Your wisdom, encouragement, and work ethic have guided me throughout this academic journey. This achievement is a tribute to the values you instilled in me and your encouraging me to follow my own path in life.

"Every life comes to an end when time demands it. Loss of life is to be mourned but only if the life was wasted." – Mr. Spock

Acknowledgements

The text of this dissertation includes reprints of the following previously published material. The co-authors listed in these publications directed and supervised the research which forms the basis for the dissertation.

Chapter 1: Alongi, T., Schwartz, S. Y., Shaddox, H. R., & Small, D. T. 2021. Probing the Southern Cascadia Plate Interface with the Dense Amphibious Cascadia Initiative Seismic Array. Journal of Geophysical Research: Solid Earth, 126, e2021JB022180. https://doi.org/10.1029/2021JB022180

Chapter 2: Alongi, T., Brodsky, E.E., Kluesner, J. and Brothers, D., 2022. Using active source seismology to image the Palos Verdes Fault damage zone as a function of distance, depth, and geology. Earth and Planetary Science Letters, 600, p.117871.

I am deeply grateful for the incredible support and assistance I have received from countless individuals on my journey to completing this dissertation.

I would first like to start by expressing my heartfelt appreciation to my primary advisors Emily Brodsky and Susan Schwartz. Your guidance and support have been invaluable beyond measure. Susan, I am especially thankful for your unwavering belief in my unconventional path to graduate school and for expert guidance in navigating non-traditional routes to success. Your assistance in crafting the first chapter of this dissertation, with your keen eye for error-catching and endless patience, has been instrumental. Your ability to foster connections within the field and provide essential advice has propelled me forward. Emily Brodsky, your

willingness to delve into new scientific questions and adapt to new methods has been a constant inspiration. Working alongside you has not only honed my critical thinking skills but also shaped me into a scientist with a thirst for understanding. I extend my gratitude to my committee member, Heather Savage, for her invaluable responses to all of my questions related to faults and experiments. Her guidance and healthy skepticism have not only improved my scientific projects but also enhanced my ability to communicate more clearly. To my committee member, Jared Kluesner, who has been more of a third advisor to me. I cannot thank you enough for your mentorship in reflection seismology, your constant availability for discussions and assistance, and your unwavering advocacy on my behalf. I would also like to acknowledge Daniel Brothers, essentially my fifth committee member, who played a pivotal role in enhancing Chapters 2 and 3 with geological insights. Both of you were instrumental in securing funding and planning fieldwork that allowed us to collect crucial data that helped shape this dissertation. I owe a depth of gratitude to Thorne Lay for initiating me into the world of seismology. Your inspirational classes and wealth of knowledge have left an indelible mark on my academic journey.

A special thank you to the EPS department office staff, Jennifer Fish and Amy Kornberg, you both are incredibly kind and so willing to help. Also, a big thank you to Sabrina Dalbesio invaluable guidance in navigate the UC system.

I am deeply thankful for the camaraderie and support of my fellow graduate students and postdocs in the seismology lab, including Grace Barcheck, Thomas

Goebel, Heather Crume (Shaddox), Ricky Garza-Giron, Alba Rodrigeuz-Padilla, Kelian Dascher-Cousineau, Kristina Okamoto, Huiyun Guo, Julia Krogh, Litong Huang, Will Steinhardt, Valere Lambert, and Gaspard Farge. Special thanks go to Heather Crume (Shaddox) for her mentorship and friendship, and to Rick Garza-Giron for sharing his passionate pursuit of knowledge and commitment to exploring the intricacies of geophysical theory. To Kristina Okamoto, I offer my sincere appreciation for your friendship and your remarkable problem-solving abilities. I also extend my gratitude to Alba Rodriguez-Padilla for engaging discussions and for co-convening conference sessions on fault damage zones.

My sincere appreciation goes to the United States Geologic Survey, Pacific Coast Marine Science Center, geologic hazards group. Your support, networking, participation in data collection at sea, and scientific insights have been indispensable. I particularly want to thank Alicia Balster-Gee for her exceptional patience in teaching me seismic data processing and her dedication to resolving data processing issues.

I am also indebted to the exceptional instructors at Cabrillo College, whose unwavering passion for STEM education has played a critical role in my academic journey. In particular, I want to acknowledge David Schwartz, Dave Reynolds, and Carlos Figueroa for inspirational teaching and belief in my potential.

Thank you to Michael Hubenthal and all those who made the IRIS internship a reality, this opportunity helped steer me toward geophysical research. I am grateful to

my cohort of fellow 2017 interns, particularly Claire Doody, Jimmy Atterholt, and Anant Hariharan, with whom I have continued to build lasting friendships and professional relationships. I'd also like to extend my appreciation to Shawn Wei and Donna Blackman for their mentorship during this initial foray into the world of science. Their guidance has not only been instrumental in my development but has also nurtured my passion for scientific exploration.

To my family, mom, and my sister, your unwavering support and stability have been a cornerstone of my academic pursuit.

Finally, to my wife, Katie, your unwavering support, patience, and guidance has been my rock throughout this journey. Your willingness to accommodate my passion for science and your help maintaining our connections with friends and family means more to me than words can express. Thank you most of all for showing me how to face challenges with compassion and grace.

Thank you all for being an integral part of my academic and personal growth. Your contributions have shaped this dissertation and my journey in immeasurable ways.

Chapter 1 – Probing the Southern Cascadia Plate Interface with the Dense Amphibious Cascadia Initiative Seismic Array

1.1 Introduction

Fault coupling is a critical component of the overall seismic cycle because regions of enhanced strain accumulation have frequently been spatially correlated with high coseismic slip. Relative plate motion is accommodated in earthquakes, slow slip transients, and longer-term coupling or creep. The interaction of these different modes of motion are still not well understood (Walton et al., 2020). The canonical model of the subduction zone includes a highly coupled megathrust, composed predominantly of large velocity weakening asperities that are surrounded by velocity strengthening regions that may slip aseismically (Bilek et al., 2004; Lay et al., 2012). The moment of the earthquake scales with the area of slip on the fault. Cascadia has sparse seismicity and infrequent historic great earthquakes, however when great events occur, they rupture a significant area of the margin (Satake et al., 2003). It is unsurprising that in Cascadia the seismogenic section is highly coupled extending to depths of ~ 20 km (Hyndman, 2013; Schmaltze, 2014; Li et al., 2018, Pollitz and Evans, 2017). Coupling models show that the degree of coupling is spatially variable along strike, and it is thought that regions of elevated coupling are stress concentrations and have more available strain energy and could be potential

nucleation sites for future earthquakes (Lapusta and Rice, 2003; Dieterich, 1986; Segall and Bradley, 2012).

The seismogenic portion of the megathrust may be bound both up-dip and down dip by a zone exhibiting transitional behavior of conditional stability and heterogeneity (Gao and Wang, 2017; Schwartz and Rokosky, 2007). The down dip transition zone has been shown to host spatio-temporal coincident slow slip events and tremor, known as episodic tremor and slip events (ETS) in Cascadia (Dragert, 2001; Shelly et al., 2007; Brudzinski & Allen, 2007, Barlow et al., 2011). This model is supported by time averaged geodetic locking models that indicate that the Cascadia megathrust is less coupled at depths deeper than 20 km (Shmalzle et al., 2014; Pollitz and Evans, 2017; Bartlow 2020). The level of updip offshore locking is poorly determined by land based Global Navigation Satellite System (GNSS) stations, and there is much uncertainty concerning the shallow updip plate interface coupling (Wang and Trehu, 2016). The extent and magnitude of shallow coseismic slip controls tsunami excitation. The amount of updip coupling is critical in determining the absolute amount of strain accumulated along the megathrust and thus the magnitude of the impending great Cascadia earthquake.

In early 2014, southern Cascadia experienced a significant strain transient in the gap between the ETS and the highly coupled megathrust. (Materna et al., 2019; Haines et al., 2019; Nuyen and Schmidt, 2021). The 2014 strain transient was observed as a rapid increase in east-ward GNSS displacements, and interpreted as a

time-dependent increase in coupling (Materna et al., 2019) or the end of a long-term slow slip event that began 1.5 years prior (Nuyen and Schmidt, 2021). The precise timing of velocity changes is poorly resolved with uncertainty of several months. Improving the time resolution of such long-term strain changes may be beneficial in determining their mechanism.

Seismicity is an indicator of strain rate changes, or a perturbation to the stress field (Dieterich, 1994, Nadeau and McEvilly, 2004). This concept is demonstrated by the spatio-temporal correlation of geodetically determined slip and seismic observations of slip by tremor and near repeating earthquakes. This strong correlation has been leveraged to increase resolution and detection of smaller amplitude transient slow slip events (Burgmann, 2018; Frank and Brodsky, 2019; Rouet-Leduc et al., 2019; Shelly et al., 2007; Bartlow et al., 2011; Uchida et al., 2020; Walter et al., 2013; Shaddox and Schwartz, 2019; Igarashi et al., 2003). It follows that if there is a change to the stress field through a strain transient (long-term slow slip event or plate interface coupling change) that it may have an observable seismic signal.

To address the outstanding scientific questions of the level of updip coupling and whether long-term strain transients can be observed seismically in southern Cascadia (Fig. 1-1), we generate a high-resolution catalog and critically analyze events near the plate interface. We use our catalog of microseismicity to characterize the mechanical behavior of the plate interface and show that the shallow plate interface is likely highly coupled due to scarce seismicity. We also compare our catalog of plate

interface seismicity to geodetic long-term strain transient observations and show a temporal correlation, providing support for the utility of seismic observations to detect and refine timing of strain transients.

1) 1-1 Regional Map - Mendocino Triple Junction

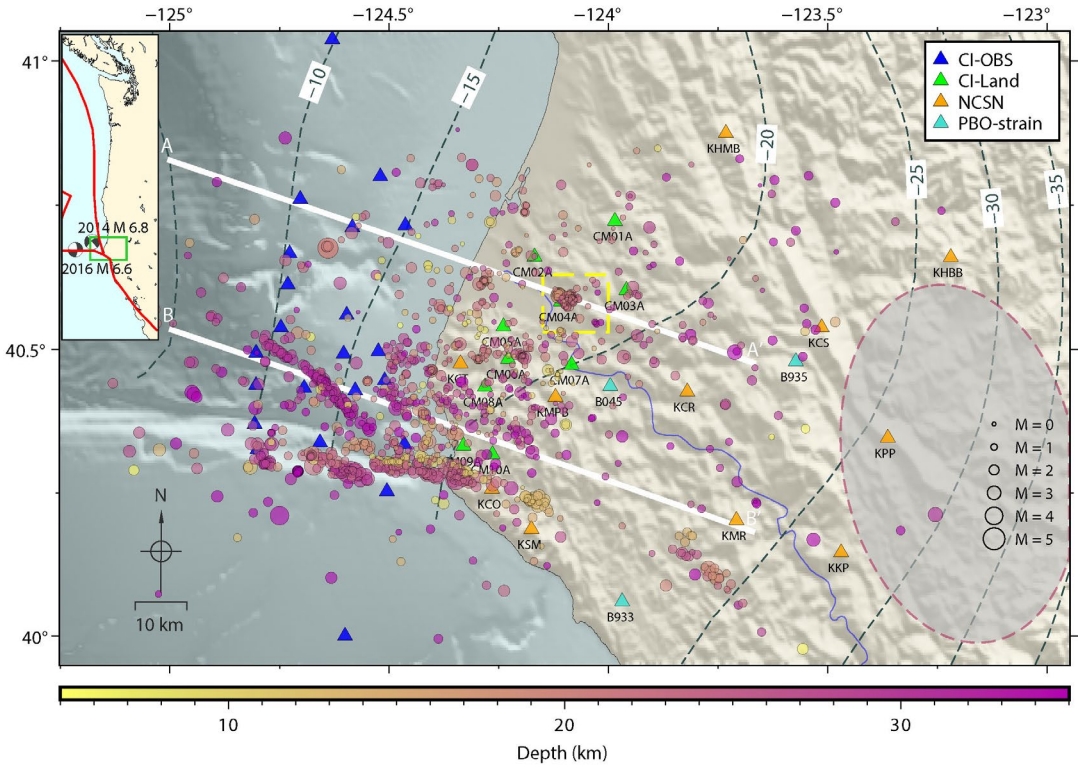

Fig. 1-1. Regional map of the Mendocino Triple Junction area in Northern California. Inset map shows the northern west coast where the study region is indicated by the green box, plate boundaries are shown in red, and two regional earthquakes that occur outside the time of the study are indicated(see discussion 4.4). Main map region showing shaded relief topography and bathymetry. Plate interface contours indicated with dark dashed lines and annotation are depth to interface (McCrory et al., 2012). Earthquake locations (this study) are circles that are scaled by magnitude and colored by depth. White cross section lines as shown in Fig. 1-2. Gray ellipse with pink dashed outline indicates area of strain transiets(Materna et al., 2019; Nuyen and Schmidt, 2021). Dashed yellow box shows the Fortuna Cluster. Triangles denote seismic stations used; blue for Cascadia Initiative (CI) ocean bottom seismometer (OBS), green for CI-short period land stations, and permanent Northern California

Seismic Network Stations (NCSN) shown in orange. PBO-strain meters shown in light blue.

1.2 Tectonic Setting and Data

1.2.1 Tectonic Background

The Cascadia Subduction Zone is in the Pacific northwest of the US and Canada. The oceanic Juan de Fuca Plate (JDF) subducts obliquely beneath the overriding continental North American Plate at a rate of 30 - 45 mm/yr, from the south to the north, respectively (McCaffrey et al., 2007 or Demets et al., 2010). The Cascadia trench trends approximately north-south and spans nearly one thousand kilometers, extending from the Queen Charlotte triple junction, offshore Vancouver Island in the north to the southern terminus at the Mendocino Triple Junction offshore Northern California. The Cascadia Subduction Zone is proximal to the spreading ridge compared to other subduction zones. It represents the warm subduction zone endmember, and as such, the JDF is young, warm, thin, and buoyant as it enters the trench. In southern Cascadia, the spreading center is closer to the trench resulting in distinct behavior. This portion of the JDF is known as the Gorda plate. The Gorda plate's dip varies near the Mendocino Triple Junction, shallowing at about 15 km and increasing again at 25 km (McCrory et al., 2012), clearly seen in the plate interface contours in Fig. 1-1. A significant portion of Cascadia seismicity occurs in the southernmost region, within the highly deformed Gorda plate. The largest Gorda plate earthquakes occurring as strike-slip events accommodating north-south compression (Gulick et al., 2001).

1.2.2 Data

The Cascadia Initiative (CI), a community-driven, National Science Foundation funded experiment, deployed a temporary, transportable array of onshore/offshore seismometers to understand the Cascadia Subduction Zone plate boundary (Toomey et al., 2014). Here we utilize the data from the fourth and final leg of the experiment, focused on southern Cascadia with approximately 10 km seismic station spacing (Fig. 1-1). The deployment consisted of 19, 3-component broadband ocean bottom seismometers (OBS - network code 7E) atop the continental shelf and slope recording at sampling rates between 50-125 Hz, depending on the instrument design. The OBS operated continuously from July 2014 – September 2015, and six of the instruments were equipped with absolute pressure gauges, though not used for this study. The onshore deployment included 11, 3-component short period instruments sampling at 100 Hz, focused near the coast, near the Mendocino Triple Junction and operated from September 2014 – September 2015 (network code 5E). Continuous waveform data from 14 permanent Northern California Seismic Network (NCSN) stations closest to the triple junction were also used throughout January 2010 – January 2020.

1.3 Methods & Results

1.3.1 Catalog Generation

1.3.1.1 Manual Pick and Initial Locations

We build a catalog by manually picking P-phase arrivals on continuous waveform data by visual inspection of vertical components of the seismograms. The events were initially located using the dbgenloc algorithm in Antelope (Pavlis et al. 2004) using a

1D velocity model befitting a subduction zone setting. We calculate local magnitudes within Antelope (mlrichter) and retain these magnitudes throughout the subsequent relocation steps. Manual picking of events resulted in 1900 earthquakes identified during the deployment (July 2014 – Sept 2015).

2) 1-2 Cross Section of Plate Interface Events

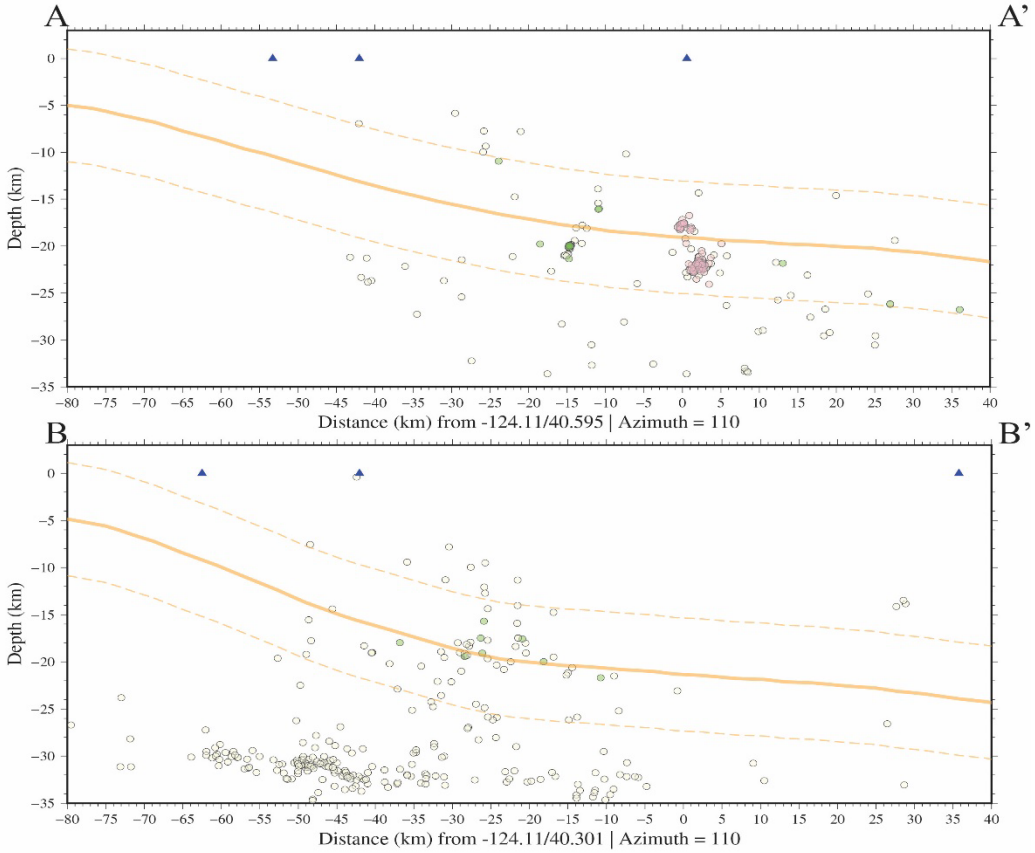

Fig. 1-2. Cross sections as indicated in Fig. 1-1. The solid yellow line indicates the location of the plate interface (McCrory et al., 2012). Dashed lines show +/- 5 km from the plate interface. Cross sections include all relocated events within 7 km of the cross section as open circles. Colored circles indicate template events that occur within the +/-5 km around the interface that found matches, in match filtering. The pink circles denote events that were used for template matching of clusters of events located below temporary station CM04A that represent a significant fraction of

interface events (Fortuna Cluster). The green circles indicate other template events that found matches. A - A' (top) B - B' (bottom).

3.1.2 Relocation using a 3D Velocity Model

Strong regional lateral velocity contrasts exist due to proximity to the Mendocino Triple Junction. For improved absolute locations, events were relocated using a 3D velocity model (Hole et al., 2000), determined in an active source seismic refraction survey. Only events within the bounds of the velocity model (east of -125W and south of 41N) were relocated and retained. We assigned velocities in a cubic lattice at nodes with horizontal and vertical spacings of 7 and 3 kilometers, respectively and performed the relocation using the simul2000 algorithm (Evans et al. 1994). Velocities deeper than 27 km were set to a constant 8.55 km/s. At this step, 1452 of the manually picked events were relocated and retained. The median root-mean-square misfit for the dataset at this step was 0.16 seconds.

3.1.3 Relative Event Relocation

Relative locations were refined with the GrowClust algorithm (Trugman and Shearer, 2017). This method clusters events hierarchically then relocates them relatively using inter-event cross-correlation values and differential travel times. Unmodeled velocity perturbations and outliers are mitigated with this method. Since the algorithm minimizes against the L1 norm, it is less sensitive to outliers. We only cluster and relocate events that meet the criteria for cross-correlation ($cc > 0.2$ for event pair at common station) and distance (max station distance 200 km). At this step, 1134 of the events were relocated and others retained their initial location (a

final event count of 1452). GrowClust uses the non-parametric resampling technique (Efron and Tibshirani, 1994) to estimate location uncertainties. The median horizontal and vertical errors are roughly 400 m. Our final locations are shown in Fig. 1-1.

1.3.2 Template Matching Plate Interface Events

Events near the plate interface may be a probe into the stress state of the neighboring plate boundary. The focus of our study is earthquakes on or near the plate interface and their temporal behavior and potential relationship to other modes of slip on the interface. We use the high-quality locations to identify events that are within the approximate uncertainty (5 km) of the plate interface model from McCrory et al. (2012). There are 526 events that meet these criteria. Fig. 1-2 shows events plotted in cross section, and most events near the interface are deeper than 15 km (see Fig. A-1 for a histogram showing the distribution of event depths that are within 5 km of the plate interface). Since we are interested in investigating the long-term temporal behavior of the interface region (beyond the limited 15-month duration of the CI deployment) we select only those events that have at least three P-phase arrivals on permanent NCSN seismic stations to perform template matching. Using 3 or more stations increases confidence that a template matched detected event has a similar location as the template. Two hundred events meet this requirement and serve as template waveforms for match filtering over continuous waveform data (a map showing template event locations is shown in Fig. A-2). Match filtering techniques exploit the fact that seismograms are a convolution of source, path, and receiver filters, and it follows that the seismogram of two events with similar location and

faulting recorded at the same station will have a similar ray path, and thus similar waveforms and high inter-event cross correlation values. The plate interface template events help identify other nearby events over the timespan of January 2010 - January 2020, allowing us to explore the temporal and evolution behavior of these plate interface events.

We carry out the template matching using the EQcorrscan python package which has the advantages and capabilities of parallelization, several quality control methods to limit spurious detections, and performs normalized multi-channel cross correlation over day-long waveform segments (Chamberlain et al., 2017). We preprocess all waveform data, templates, and continuous waveform data, by applying a zero-phase 4th order 3 to 10 Hz bandpass filter, down sampled to 25 Hz. The template events are trimmed to 0.15 seconds before the P-pick to a total duration of 4.6 seconds. Our criteria for detections are that the matched event must have an average cross-correlation coefficient greater than 0.6 and a median absolute deviation greater than 10. We set these criteria to ensure that templates and detections are nearby (Geller and Mueller, 1980; Fremont and Malone, 1987). In the template matching routine, we remove channels with spurious data-spikes as they will cause errors in the cross-correlation calculation. Following match filtering, the detection catalog is post-processed. We remove duplicate detections that occur when multiple templates match with the same detection and retain the detection with the highest inter-event cross-correlation value. Additionally, we scan the catalog for detections that occur within 2

seconds of each other, again saving the event with the highest inter-event cross correlation value. See an example of detection and template in Fig. 1-3.

Template matching of the 200 templates finds 2363 unique detections over the time span of January 2010 - January 2020 (see Fig. A-3 for a time series showing all detections). 1519 of these detections are made with 106 templates that occur clustered below CI station CM04A near Fortuna, northern California (and clearly anomalous in Fig. A-4), while the remaining 94 plate interface template events identify 844 unique detections. There are roughly the same number of templates generated within the cluster as there are in aggregate around the remaining plate interface; however, the cluster templates identify nearly 2 times more detections. The cluster of events accounts for roughly 10% of our catalog's total number of events and is confined to a small volume approximately 3 km in radius (Fig. 1-1) The cluster exhibits noteworthy temporal clustering as well. There were no detections prior to February 2013, and only a handful of events occurred before activity abruptly increased in February 2014 and continued for 2 years. This cluster of events, hereon referred to as the Fortuna cluster, is anomalous in temporal behavior and in the density of events in space. The Fortuna cluster’s association with other plate interface observables are discussed in further detail in the Discussion section.

3) 1-3 Example Template Matched Event

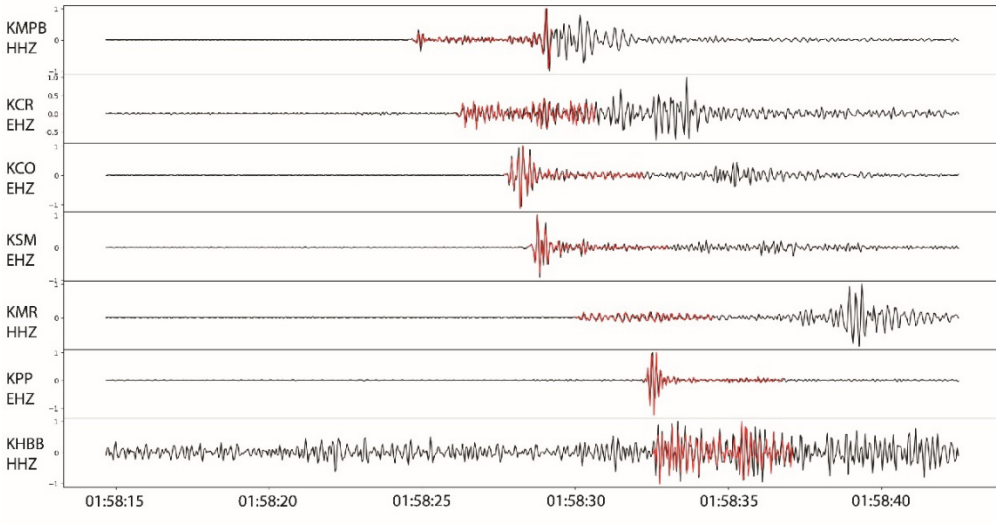

Fig. 1-3. An example of template matching results. Template waveform shown in red overlain on detecting waveform in black. Amplitudes are normalized by their maximum. This match was detected on seven channels of permanent Northern California Seismic Network stations, the detection has an average cross correlation value of 0.9. The template event occurred on 2014-12-23 and this event was detected 2014-3-2, which is the approximate time that the Fortuna cluster initiates.

1.3.3 Determining Faulting Geometry

To discriminate interplate from intraplate events within the Fortuna cluster, we generate focal mechanisms. We employ the first motion polarity inversion method of HASH (Hardebeck and Shearer, 2002), which is a routine method of small mechanism determination and accounts for errors in location, velocity model, and possible polarity mis-picks. Here we specify a maximum azimuth gap of 90° and a minimum of 7 polarities to grid search for preferred double couple solutions. We presume that most of our polarities are accurate (0.05 polarity errors) due to manual

inspection on all stations (CI & NCSN) in the snuffler - pyrocko package (Heimann et al., 2017), which allows for fine tuning filters actively while examining the waveforms, allowing us to ensure stability of the polarity from lower to higher frequencies. The magnitude of these events ranges from magnitude 0 - 3. Mechanisms were successfully calculated for 37 of the 106 template events, though we only interpret events that are “C” quality and better. We generate 8 and 5 C and B quality mechanisms respectively, refer to Hardeback and Shearer (2002) for a description of mechanism quality. Fig. 1-4 shows a map with these event focal mechanisms. There is a diversity of faulting geometry with both strike slip and dip slip events occurring, and examples of each plotted with first motion arrivals on a stereonet can be found in Fig. A-5.

4) 1-4 Fortuna Cluster Focal Mechanisms

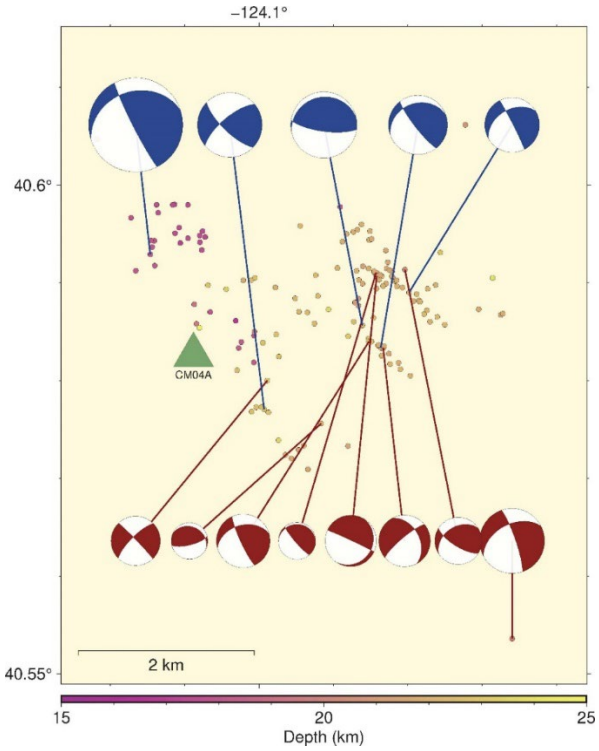

Fig. 1-4. Zoom in of the Fortuna seismicity cluster (location indicated by yellow box in Fig. 1-1). Focal mechanisms are first motion determined and inverted with HASH. Blue mechanisms indicate "B" Quality, Red are "C" quality. Also included are all relocated events in the area colored by depth.

1.4 Discussion

1.4.1 Comparison with Other Catalogs

We create a high-resolution catalog of 1452 events to help identify earthquakes that occur near the plate interface, including smaller events not identified previously. Over the same time (July 2014- October 2015) and region (40 to 41N / -123 to -125W) as this study, the NCSN high-quality double-difference catalog contains 446 events, and the Advanced National Seismic System (ANSS) catalog includes 552 events. We increased the number of identified events by a factor of 3 (Fig. A-6, for a

comparison of the catalog from this study and ANSS catalog). Our catalog also improves the magnitude of completeness over the ANSS catalog from 1.75 to 1.5 (Fig. A-8). Completeness was calculated using the maximum curvature method. This newly created catalog is a clear improvement on the existing routinely generated catalogs.

This catalog is the first to fully include the year 4 densely spaced CI amphibious data. The events in our catalog were picked manually by human analysts and include low magnitude events (ML 0-3.5) that are easily missed by automated methods. Our events are located with the best available 3D velocity model (Hole et al., 2000), and event locations are improved with cross-correlation based relative relocation methods. Chen and McGuire (2016) investigated seismicity in southern Cascadia using CI data; however, the data they used were from the September 2012 to February 2013 phase of the deployment which had much larger station spacing and did not include the additional land stations deployed in 2014. Using STA/LTA ratios the same 3D velocity model and TomoDD double difference relocation method they created a catalog of 1137 earthquakes. Their area of investigation extended much further west and included many more events along the seismically active Mendocino Fracture Zone, which were not the focus of this study. Stone et al. (2018) used data from the complete 4-year duration of the Cascadia Initiative to explore the distribution of seismicity along the entire Cascadia Subduction Zone, though the study focused on latitudes north of 41°N, thus omitting southern Cascadia (40°N - 41°N). Our newly

generated catalog fills and complements the existing Cascadia Initiative experiment studies.

1.4.2 Seismicity Trends

Our high-resolution earthquake catalog illuminates many interesting seismicity features and trends. Diffuse clouds of seismicity generally relocate to tight and linear clusters (highlighted in Fig. A-7). Seismicity delineates the Mendocino Fracture Zone, which is partially creeping (Materna, et al., 2018). Relatively few events are located within the upper plate, and it is challenging to associate events with mapped USGS quaternary active faults. However, several of the events and linear features are consistent with the trend of many of the mapped quaternary faults (Fig. A-7).

Apart from the Mendocino Fracture Zone, other linear trends of seismicity are at depths consistent with occurring within the Gorda slab and are oriented sub-parallel to the trend of the San Andreas Fault, upper plate mapped active faults, and strike-slip faults on the incoming Gorda plate. The most notable of these features appears near the Mendocino Triple Junction in the Gorda slab as a continuous band of seismicity extending over 30 km in length (Fig. A-7). These events are observable in existing catalogs but as diffuse seismicity; here they clearly delineate a fault. Chen and McGuire (2016) also noticed this localized region of earthquakes and pointed out that events along this fault, within the oceanic mantle, had an order of magnitude higher stress drops than events located shallower near the plate interface. These trends of

seismicity may be delineating a fabric within the Gorda slab that is also expressed in faulting in the upper plate.

There is a general absence of seismicity near the shallow interface (shallower than 15 km) during the period of investigation (Fig. 1-2), indicating that the plate boundary is either highly coupled and accumulating strain or stably sliding. If the interface were stably sliding without earthquakes, it would require homogeneous velocity strengthening materials and no velocity weakening asperities, which has not been documented. Alternatively, the interface could have velocity weakening asperities that are too small in area or slip that the magnitude would be below the limits of our observations. Another possibility is that the shallow updip region is in a stress shadow of high coupling in the seismogenic zone below this depth and thus kinematically locked (Lindsey et al., 2021). While we acknowledge that the shallow region could be sliding completely aseismically, we favor locking because the configuration of the seismic array provided excellent coverage offshore and maximum detectability of events and a thorough examination shows extremely sparse seismicity. The probable high coupling of the megathrust from the trench to the downdip limit of locking has implications for earthquake and tsunami modeling efforts. The larger area of locking implies that there is a larger area accumulating strain and a larger impending rupture area, and thus a larger magnitude than if this updip area was less coupled and creeping. Additionally, if the toe of the subduction zone is accumulating strain, then more shallow slip will occur and displace a greater volume of the overlying ocean, exciting a larger tsunami (Lay et al., 2019).

Although the shallowest portion of the megathrust is mostly devoid of seismicity, there are 526 events that are located within 5 km of the plate interface. These near plate interface events are small with magnitudes between 0 and 3.4, the mean magnitude for these events is 1.2 +/- 0.6. Most events near the plate interface occur deeper than 15 km, with a mean depth of 20.8 +/- 3.2 km (see Fig. A-1). The depth of the majority of the near plate interface events coincides with the transition from a high to low coupled plate interface at about 20 km (the lower limit of the seismogenic zone) (Hyndman, 2013; Schmalzle, 2014), as well as shallowing of the dip of the plate interface (see interface contours on Fig. 1-1). The most noteworthy near plate interface events occur in the Fortuna cluster of 146 earthquakes, which is 10 % of the entire catalog, located at 40.6 N / 124.1 W, 20 km beneath Fortuna, California (yellow box in Fig. 1-1). This cluster accounts for a significant fraction of the seismicity in the study area and is spatially concentrated, confined to an ~30 km^2 area.

1.4.3 Fortuna Earthquake Cluster

The Fortuna cluster is located directly beneath the temporary CI station CM04A, near the interface. Locations are well determined due to the close station spacing and good azimuthal coverage in this area. The events appear to form two distinct clusters, one centered at a depth of 17 km and the other at 22 km depth (Fig. 1-2a). To determine if this cluster is unique in time, we examined seismicity in the area from the ANSS catalog over the last 40 years from 1980 to 2020 (Fig. 1-5). This cluster of seismicity is clearly visible in the ANSS catalog only during the 2014-15 time period

(indicated in Fig. 1-5a). A closer examination of the volume surrounding this cluster reveals that it may have had a burst of seismicity toward the end of 1982 (Fig. 1-5b) but is quiet at all other times. The cluster straddles the plate interface (pink circles in Fig. 1-2) of McCrory et al., 2012. The event locations and depths are consistent with the proposed downdip limit of high coupling in Cascadia (Hyndman, 2013; Schmalzle, 2014). Near this cluster, the McCrory slab morphology is unusual dipping concave up rather than continuous concave down geometry observed elsewhere along the Cascadia margin.

There is a diversity of faulting geometry for well-constrained focal mechanisms in this cluster, in that there are both strike-slip and dip-slip earthquakes (Fig. 1-4). The strike-slip mechanisms are oriented similarly to large strike-slip earthquakes that have been observed in the incoming Gorda plate (Gulick et al., 2001; Chaytor et al., 2004) and oriented sub-parallel to the strike of the San Andreas fault, suggesting a reactivation of a preexisting structure or merely response to the regional stresses. The thrust focal mechanisms are consistent with the relative plate motion between the subducting and overriding plates. The variety of focal mechanisms leads to tenuous seismotectonic conclusions. However, the complexity of focal mechanisms indicates that these events do not occur on a single fault with a consistent sense of motion; they do not represent rupture of a single repeating asperity. The diversity of focal mechanisms indicates that the events are responding to a complex regional stress field and possibly reactivation of a pre-existing fabric.

5) 1-5 Fortuna Cluster is Anomalous in Time

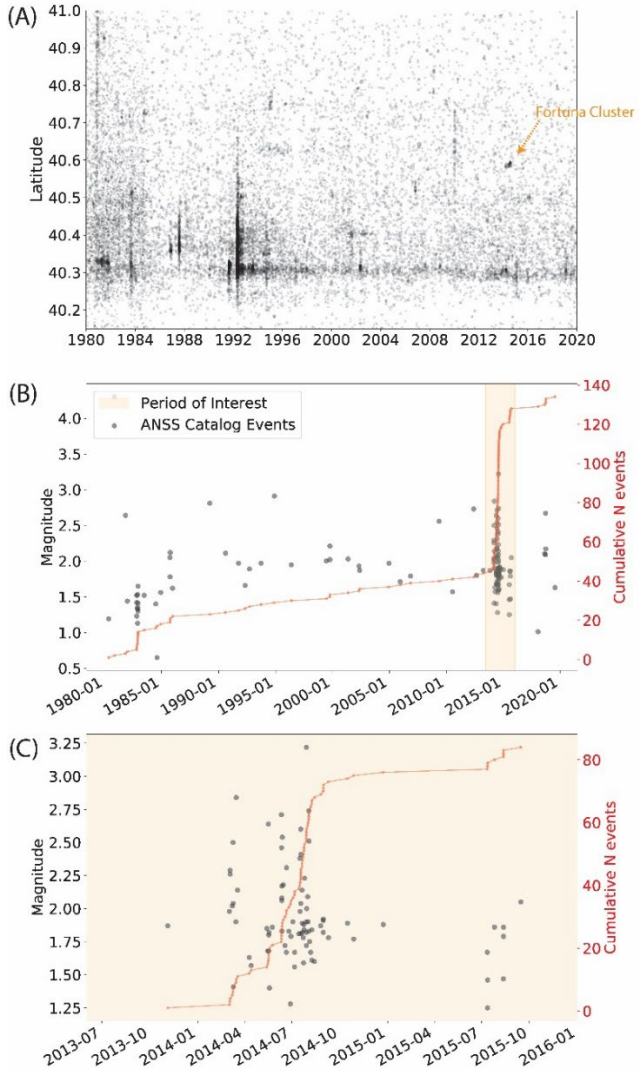

Fig. 1-5. (a) Advanced National Seismic System (ANSS) Comcat catalog over the bounds of the study area 40°N to 41°N/125°W to 123°W, showing event latitude as a function of time. Fortuna cluster (40.6°N) clearly anomalous in 2014. (b) Plot showing events from ANSS 1980–2020 activity in 10 × 10 × 10 km3 volume centered on Fortuna cluster (40.6°N/123.1°W/20 km depth). Note the sparse activity prior to 2014, which drastically increased starting March 2, 2014, which is shown clearly on the (c) plot.

Magnitudes of events within this cluster are between 0 and 3.5, and events do not show a clear mainshock-aftershock magnitude distribution nor an Omori like

aftershock sequence (Fig. 1-5c), suggesting swarmogenic behavior (Mogi, 1963; Vidale and Shearer, 2006; Nishikawa and Ide, 2017). Our catalog reveals that the duration of this cluster is several years (2014-2017, Fig. 1-6) which is longer than swarm activity occurring in other regions. Swarms have been reported to typically last on the order of weeks to a few months (Xue et al., 2018; Miller et al., 2004; Lohman and McGuire, 2007; Roland and McGuire, 2009; Vidale and Shearer, 2006). However, recently a long-lived swarm, ~4 years in duration, has been documented in southern California (Ross et al., 2020) that is closer to the duration of the persistent activity in this study. The swarm in Ross et al. (2020) exhibits a clear expanding migratory pattern that is inferred to be fluid driven and structurally guided. Our study differs vastly in that we have identified many fewer events and only weak northwest to southeast migratory behavior (Fig. A-9). Cascadia does not have any documented tectonic swarm activity (Holtkamp and Brudzinski, 2011; Nishikawa and Ide, 2017). The long duration of activity, absence of clear fluid induced migration, and lack of spatio-temporal correlation with documented slow slip events make us hesitant to classify the localized seismicity here as a swarm. Instead, we prefer to refer to it as a seismicity cluster. Another example of an isolated seismicity cluster in space and time was recently documented in northern Cascadia. Merrill and Bostock (2019) identified an earthquake nest located in the Juan de Fuca mantle at depths greater than 60 km and concentrated in a 30 x 10 x 10 km^3 volume. Generally, nests are classified as intraslab intermediate depth seismicity that persists for decades (Prieto et al., 2012). Our cluster is confined to a ~ 6 x 6 x 6 km^3 region with depths between 17 - 23 km,

therefore it does not fit the definition of an earthquake nest. The proximity of this locus of events to the plate interface suggests that it is likely experiencing a similar stressing field as the plate interface.

6) 1-6 Fortuna Cluster Template Matched Detection Time Series

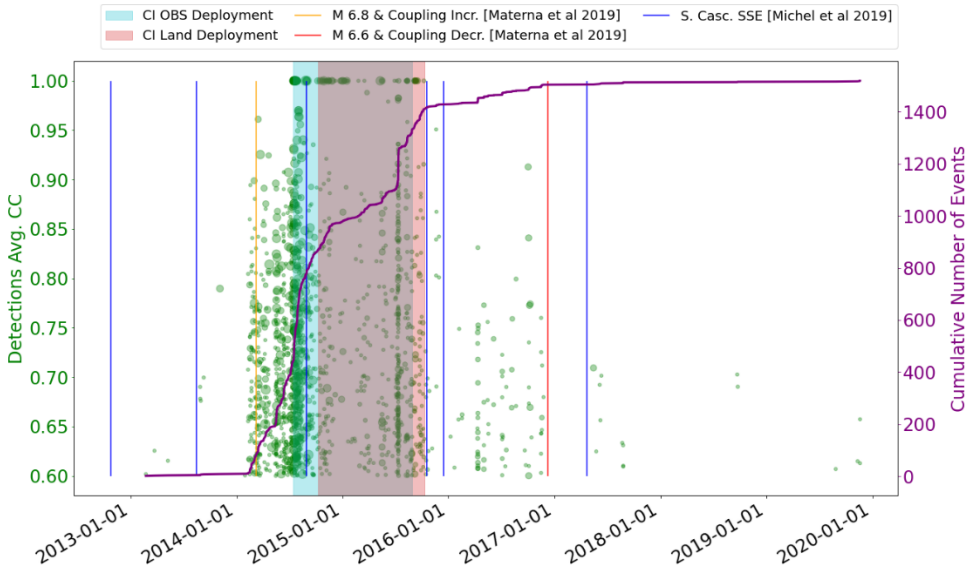

Fig. 1-6. Time series showing template matched detections for templates in the Fortuna cluster. Template matching was performed over the time period of Jan. 2010 through Jan. 2020; the first detection occurred in Feb. 2013, and detections increased significantly in Feb. 2014. There were 106 template events used here to identify 1519 unique detected events. The green markers are detections where marker size is scaled by the number of channels used in detections, ranging from 3 to 11 channels, smallest to largest respectively. The events with cross-correlation values = 1 are templates finding themselves in continuous data. Purple curve shows the cumulative number of detections. Blue vertical lines indicate the approximate timing of maximum moment of Southern Cascadia slow slip events from Michel et al., 2019. Yellow and red vertical lines indicate the timing of large regional earthquakes (Fig. 1-1) and approximate timing of long-term strain transient from Materna et al. (2019). Light blue region highlights Cascadia Initiative OBS deployment, light pink region highlights Cascadia Initiative land deployment, and the purple area is the overlap of both datasets.

1.4.4 Fortuna Cluster and Strain Transients

Template matching of the 106 events within the Fortuna cluster over the timespan of 2010 - 2020 identifies over 1500 newly detected events (Fig. 1-6). Most of these new detections are concentrated in time. This confirms the finding of the ANSS comprehensive catalog (Fig. 1-5c) that the cluster region was primarily active during a short interval of time around 2014-2016 with little to no seismic activity outside of this period. The timing of this near-interface seismicity does not appear to correlate with southern-Cascadia slow slip events (Fig. 1-6) that occur down-dip of this cluster (Michel et al., 2019); suggesting that the cluster is not sensitive to or driven by downdip slow slip events.

There is a temporal correlation between the Fortuna cluster and long-term regional strain transients (Fig. 1-6) (Materna et al., 2019; Haines et al., 2019; Nuyen and Schmidt, 2021). Materna et al. (2019) and Nuyen and Schmidt (2021) identified two abrupt velocity changes (early 2014 and early 2017) in the southern Cascadia GNSS

time series. They modeled these velocity changes as variations in slip on the megathrust at a depth of ~30 km in the gap between the episodic tremor and slip zone and the down-dip limit of the highly coupled zone (Gao and Wang, 2017), ~ 40 km from the Fortuna cluster. These changes bracket the time that the Fortuna seismicity cluster is active, and seismicity rate rapidly increases in February 2014. Nuyen and Schmidt (2021) propose that the 2014 GNSS velocity change was the rapid arrest of a long-term slow slip event, which started in mid-2012. Alternatively, Materna et al. (2019) attribute the 2014 regional GNSS velocity change to a dynamically triggered increase in megathrust coupling occurring in response to the 2014 March 10, M 6.8 offshore strike-slip earthquake (Fig. 1-1). Before the 2014 earthquake, Materna et al. (2019) observe steady velocities. Materna et al. (2019) speculate that the 2014 velocity change occurs as fluids are liberated from the region in response to the passage of seismic waves that reduces pore-pressure and increases effective normal stresses, decreasing the ability of the plate interface to slide stably (Fig. 1-7). The most substantial GNSS velocity change occurs in early 2014 and reflects either an increase in coupling or the termination of the 1.5-year long-term slow slip event. A more recent long-term strain transient occurred near the end of 2016 and beginning of 2017, indicated by a reduced eastward velocity and interpreted as a decrease of coupling on the plate interface (Materna et al., 2019) or the onset of a long-term slow slip event (Nuyen and Schmidt, 2021). This motion change also conspicuously coincides with a large M 6.6 regional earthquake on 2016 December 8 on the Mendocino Fracture Zone (Fig. 1-1). As with the previous strain transient, Materna et

al. (2019) speculate that this has occurred in response to dynamic triggering by a large regional earthquake. This velocity change occurs as the Fortuna cluster seismicity rate decreases.

Since the Fortuna seismicity cluster is unique in time and temporally correlated with GNSS strain transient observations, we surmise that the two observations are related and that we can therefore obtain better temporal resolution of the long-term strain transient using the onset time of the seismicity cluster. The cluster suddenly initiates about one month before the 2014 M 6.8 earthquake and continues through early 2017, at which time Fortuna cluster seismicity terminates (Fig. 1-6). An abrupt strain transient on nearby borehole strainmeter stations B045 and B933 (locations shown in Fig. 1-1) occurs in February 2014 when the seismicity cluster initiates (Fig. A-10) and supports that the onset of the 2014 strain transient precedes the M 6.8 2014 earthquake. However, exactly how the Fortuna seismicity cluster and increased eastward motion relates to the strainmeter transient is unclear from only two observations.

7) 1-7 Schematic Relating Seismicity to Potential Causes

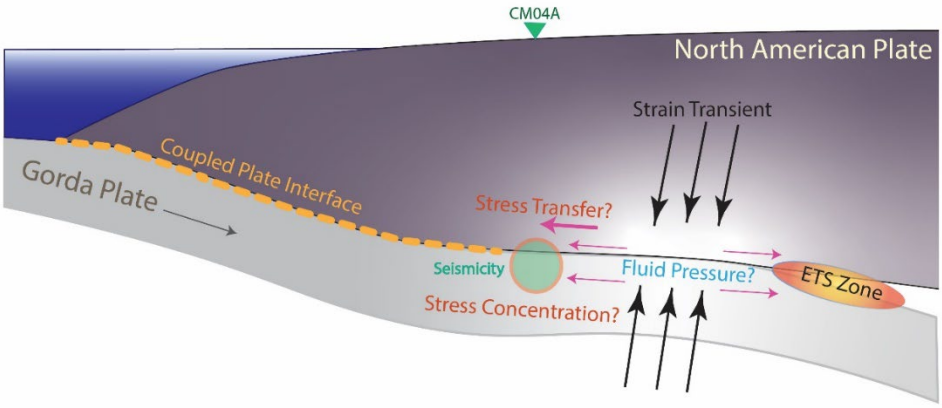

Fig. 1-7. Cartoon schematic cross section representation of observations described in the discussion section. Region of strain transient (coupling increase or the termination of a long-term slow slip event) is intermediate between the downdip limit of locking and the episodic tremor and slip region (ETS). Seismicity clustered near the downdip limit of locking is activated contemporaneously with the strain transient. The two observations are temporally correlated and we speculate that the cluster is the seismic manifestation of the strain transient. Also shown is the coupled region of the plate interface extending all the way to the trench, which is suggested by the lack of plate interface seismicity. Modified after Materna et al., 2019.

What is clear is that the Fortuna seismicity cluster occurs on and close to the megathrust in a region of slab distortion that is sensitive to plate interface stress perturbations. It is uniquely bracketed in time by a period of increased eastward GNSS velocity, attributed to a period of increased locking or between long-term slow slip events. The diversity in faulting geometry suggests that this cluster occurs in a region of a stress concentration. Although we cannot conclusively determine the Fortuna cluster's driving mechanism, it is likely either driven by fluids liberated from the region of coupling increase or by stress transfer attributed to relocking following a

long-term slow slip event (Fig. 1-7). In either case, the Fortuna cluster appears related to and may indicate the long-term plate interface strain transients. Similar to the way tremor is used as a timing proxy for slow slip events, earthquake clusters may be useful as a timing proxy for coupling changes and provide further insight into the range of plate interface behavior.

1.5 Conclusions

We construct a 15 month (July 2014-October 2015) high resolution earthquake catalog for the southernmost Cascadia margin near the Mendocino Triple Junction. This catalog demonstrates a clear lack of seismicity in the shallow updip plate interface region. This absence of seismicity along the shallow interface suggests that the interface is highly coupled. We also observe a cluster of events that locates near a contortion in the plate interface at the downdip limit of the highly coupled seismogenic zone. Using template matching, we investigate this cluster's activity during the extended period between 2010-2020. We detect over 1500 events that occur within a 3-year period (2014-2017) bracketed in time by an abrupt GNSS increase in eastward velocity that has been interpreted as a coupling increase, or between long-term slow slip events. We speculate that the seismicity is a response to the strain transient on the interface, as either a result of stress transfer reactivating pre-existing fabrics or fluid migration and can therefore provide constrains on the onset and termination time. This is particularly useful since the precise timing of the long-term strain transients are not well determined from the GNSS time series. We

propose that seismicity clusters may be used to help delineate the onset and termination of long-term changes in plate interface slip behavior.

Chapter 2 – Using Active Source Seismology to Image the Palos Verdes Fault Damage Zone as a Function of Distance, Depth, and Geology

2.1 Introduction

Earthquakes release accumulated elastic strain energy. Part of that energy is consumed in the fracturing of rock both on the fault and in the surrounding damage zone. The damage zone is broadly defined as the area where fracture density is higher than the surrounding background fracture density (Chester and Logan, 1986; Kim et al., 2004; Mitchell and Faulkner, 2009; Faulkner et al., 2010) and forms a halo of increased fracturing around the highly localized principal slip surface (Chester et al., 1986; Caine et al., 1996; Choi et al., 2016; Rodriquez Padilla et al., 2022). Damage zones are significant in earthquake physics for at least four reasons. First, the damage process itself is potentially a sink of energy during earthquake rupture (Wong, 1982; Martel and Pollard, 1989; Wilson et al., 2003; Chester et al., 2005; Abercrombie and Rice, 2005; Brodsky et al., 2020). Constraining the extent of the damage zone at depth is important for evaluating the relative importance of fracture energy in the overall energy budget of the fault system. Secondly, damage zones are highly permeable and particularly important in controlling the distribution and mobility of fluids around faults (Caine et al., 1996). Since fluid pressure can be a major factor in earthquake nucleation (Hubbert & Ruby, 1959), understanding the structure of the damage zone is a prerequisite for modeling how fluid flow can contribute to initiating and propagating earthquakes. Thirdly, the rheology of the damage zone is distinct

from the surrounding media and plastic deformation in the damage zone can alter the rupture dynamics of an earthquake (Dunham, 2011; Thakur et al., 2020). Finally, the extent of the damage zone reflects the aggregate seismic deformation across a particular fault and thus could potentially be used to guide hazard investigations. Offset features are typically measured over a relatively narrow width on either side of the fault and may not capture all of the coseismic deformation and thus measuring damage provides a potentially important alternative window into the seismic history. Establishing the extent of the damage zone in three-dimensial (3D) space is therefore an important goal for both fundamental science and pragmatic reasons.

Despite its importance, basic knowledge of the systematics of the 3D damage zones is limited, and much of what is known is from geologic outcrop exposures and related observations (Scholz et al., 1993; Wilson et al., 2003; Shipton et al., 2006; Mitchell & Faulkner, 2009; Savage & Brodsky, 2011 Keren & Kirkpatrick, 2016). In these studies, the damage zone width has been shown to scale nonlinearly with various fault parameters such as length, displacement or throw, and number of strands (Childs et al., 1997; Cowie and Shipton, 1998; Savage and Brodsky, 2011; Torabi and Berg, 2011). Outcrop studies of exhumed fault zones and surface rupture are limited to surficial measurements of fracture density and lack the means to quantify the damage in-situ at depth. Limited availability of fault exposures has made it difficult to disentangle the contributions of lithology, depth, and distance from the fault. Undoubtedly all three factors play a role in controlling the relative damage, but they are seldom separable in outcrop studies.

Passive seismic data have provided some insights on the in-situ fault damage zones. Some studies have shown a reduction in seismic body wave velocities near faults and were interpreted to be due to reduced elastic moduli, a proxy for damage (Ben-Zion et al., 2003; Vidale & Li, 2003; Cochran et al., 2009;). However, these studies are limited by access and deployment logistics on land as well as sparse and often clustered earthquake sources to sample the fault zones. Extent and velocity changes often trade-off in inversion methods, thus establishing variations with depth, distance and lithology are again challenging by these methods.

Active source marine seismic data can provide a higher-resolution view of the fault damage zone because they do not rely on proxies to infer elastic moduli and is a more direct approach for detecting faults and fractures. Three-dimensional seismic reflection techniques, typically used in hydrocarbon exploration, have long been used to infer faulting in-situ through offsets in reflectors. Similarity attributes have been used to improve and guide the interpretation of faults in seismic data (Bahorich and Farmer, 1995; Marfurt et al., 1998; Chopra and Marfurt, 2005). These methods use measures of multi-trace similarity over a moving window and have been validated with forward modeled synthetic faults in seismic volumes (Botter et al., 2016). Faults have been identified using similarity attribute methods (Iacopini et al., 2016) and subsequently used to study the fault damage zone on fault perpendicular cross sections in seismic volumes (Torabi et al., 2017; Liao et al., 2019; Ma et al., 2019). Rather than analyzing the damage zone at representative cross sections, the present study aims to examines the damage zone in the full 3D volume. Additionally,

machine learning approaches have implemented supervised neural networks to set the weights of ensembles of discontinuity-detecting attributes to highlight faults and possible fluid pathways associated with fault junctions (Kluesner and Brothers, 2016).

Here we apply a previously developed modern fault detection and localization algorithm to existing 3D marine seismic data along the Palos Verdes Fault to extract a 3D fault network from the data. Prior studies have suggested that fracture density follows well-defined statistical distributions that need to be well-sampled in order to be quantified (Mitchell & Faulkner, 2009; Savage and Brodsky, 2011). Reflection seismic data provide a powerful way to define these distributions using averaging in large volumes to seek generalizable behavior. We follow this approach by detecting fractures, measuring systematics, averaging volumes, and then pursuing the spatial and lithological controls on damage.

2.2 Tectonic Setting and Data

2.2.1 Palos Verdes Fault in Context

The Palos Verdes Fault (PVF) is mainly located offshore southern California in the Inner Continental Borderland and accommodates a portion of the distributed shear zone between the Pacific and North American Plates (Fig. 2-1). Current estimates suggest that the California Borderland accommodates 6 - 8 mm/yr of right lateral motion, and the Palos Verdes Fault slip rate is between 1. 6 - 4 mm/yr (Ward and Valensise, 1994; McNeilen et al., 1996; Brankman and Shaw, 2009; Brothers et al., 2015). The northwest southeast striking fault stretches over 100 km in length, from

Lausen Knolls in the south to Santa Monica Bay in the north and its connectivity with other faults remains a topic of interest. The Palos Verdes Fault has very few recorded earthquakes in the San Pedro Shelf region (Fig. 2-1). Uncertainties in fault dip and connectivity to nearby faults yield uncertainty in maximum earthquake magnitude potential (Mw 6.5 - 7.5). There is clear vertical separation of the sedimentary units across the fault where units west of the fault are closer the seafloor, and there is decreasing vertical separation toward the south. Seismic data show that the fault is near-vertical in the upper 2 km, but debate continues about whether the fault becomes listric at depth (Fisher et al., 2004; Brankman and Shaw, 2009; Brothers et al., 2015). It has been suggested that the Palos Verdes Fault soles into a master décollement below the Los Angeles basin and may be a component of a larger fault system (Webb and Kanamori, 1985; Hubbard et al., 2014).

The geological history of the region is largely controlled by the transition from a convergent to transform plate boundary that occurred as the Farallon Plate was completely subducted beneath the North American Plate during the Oligocene (~30 Ma) (Atwater, 1970; Bohannon and Geist, 1998). The plate boundary transition led to several stages of faulting, deformation, and stress reorientation over the history of the Palos Verdes Fault. Pre-Miocene Borderland (~25 Ma) tectonics are characterized by flat slab subduction and intense contact metamorphism. By the early Miocene (~23 Ma) the margin had reorganized to transform tectonics, and that was followed by late-Miocene oblique extension, leading to rifting of the Borderland and vertical axis clockwise block rotation of the western transverse ranges (Crouch and Suppe, 1993).

Seismic stratigraphy of Monterey Formation sediments suggests that the Palos Verdes Fault was active by at least the middle to late Miocene (~15 Ma) (Brankman and Shaw, 2009; Sorlien et al., 2013). In the early Pliocene (~ 6 Ma) the plate boundary stepped inland and created a major left step restraining bend (known as the Big Bend) changing the Borderlands from a transtensional to a transpressional system. This transition led to reactivation of extensional normal faults as oblique thrust faults (Yeats and Beall, 1991; Wright 1991). The existence of the uplifted Palos Verdes Peninsula anticlinorium and associated marine terraces suggests that this topography is supported by oblique convergence (Plesch et al., 2007), a transpressional restraining bend, or a combination of the two (Ward and Valensise, 1994; Shaw and Suppe, 1996; Fisher et al., 2004; Sorlien et al., 2013). The geologic history includes the superposition of several different tectonic and stress regimes that cumulatively contribute to the damage zone. There is a clear difference in the deformation history on the west versus east side of the Palos Verdes Fault. The anticline west of the fault appears to be decoupled from the relatively horizontal sediments in the basin east of the fault that are observable in the data to ~ 10 km from the fault.

8) 2-1 Map of Palos Verdes Study Area

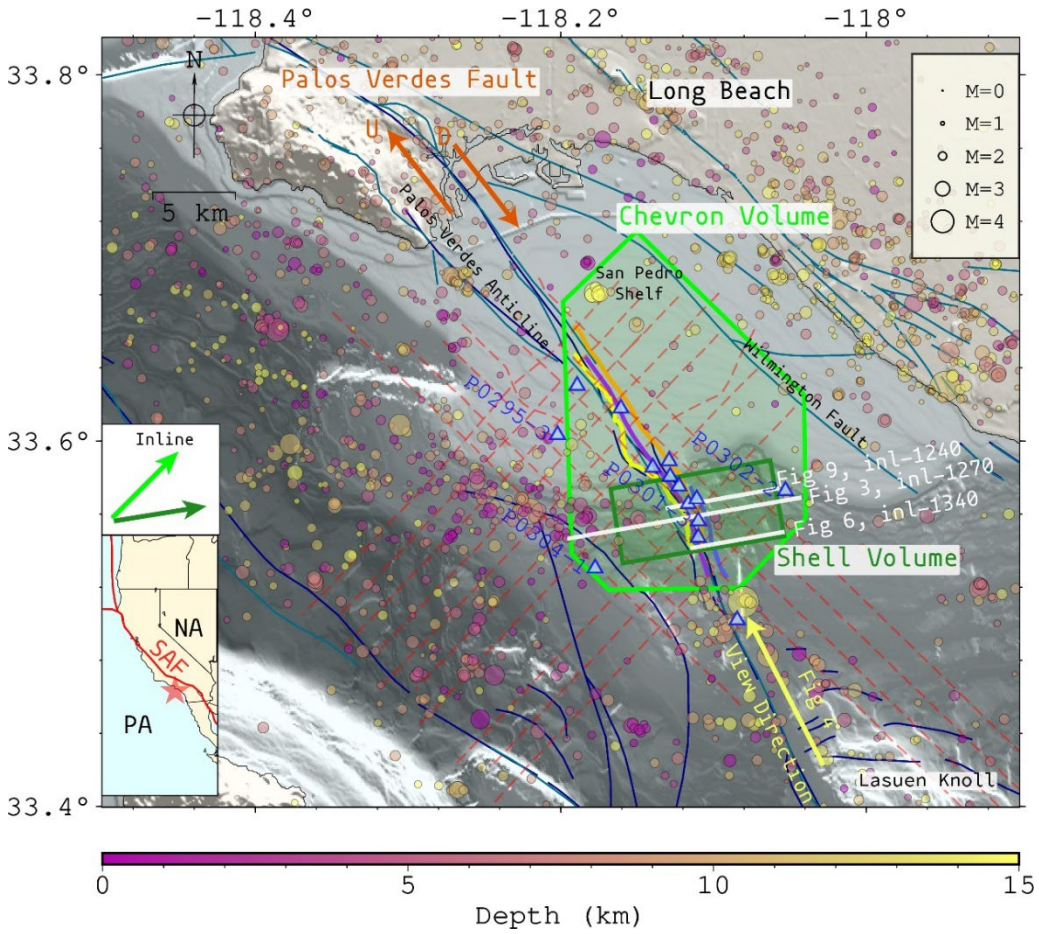

Fig. 2-1. Map of southern California Inner Continental Borderland and San Pedro Shelf. Inset map shows western North America with the red star indicating the study area offshore southern California, NA - North American Plate, PA – Pacific Plate, SAF – San Andreas Fault. Main map shows location of mapped fault traces, where the navy-blue lines are mapped offshore Quaternary faults (Walton et al., 2020) and the turquoise lines are onshore Quaternary faults (U.S. Geological Survey and California Geologic Survey, Quaternary fault and fold database for the United States, accessed August 2019). The green polygons depict the bounds of the three-dimensional (3D) marine active source datasets, lime green for Chevron volume and forest green for Shell volume. The solid yellow, purple, orange, and blue lines within the seismic volume footprint are the western, central, eastern and eastern 2 fault strands respectively mapped in this study. Dashed red lines indicate the two-dimensional (2D) lines used in the study. The blue triangles indicate the surface location of the geophysical well logs, named logs are outside of the fault zone and referred to in the text. White lines are the location of cross-sections of lines shown in other figures. Yellow arrow is the view direction from Fig. 2-4. Circles represent

earthquakes colored by depth (purple to yellow, shallow to deep) and scaled by magnitude from the Southern California Earthquake Data Center alternate catalog [1981 - 2018] (Hauksson et al., 2012).

2.2.2 Data

To examine the damage zone in-situ we utilize existing marine seismic reflection data that are available through the USGS at the National Archive of Marine Seismic Surveys (Triezenberg et al., 2016). We use two overlapping legacy exploration 3D marine seismic reflection datasets along with 2D multi-channel seismic lines collected offshore of Los Angeles over the San Pedro shelf and slope, spanning ~ 17 km along strike distance of the Palos Verdes Fault (Fig. 1-1). The larger of the two seismic volumes survey is bound by a 7-sided polygon with a 350 km^2 footprint and was collected by Unocal in 1976 (C-01-76SC-3D). The airgun seismic source was recorded by a multichannel streamer sampling at 4 ms with bin spacings of 50 m and 25 m in the inline and crossline directions, respectively. Additionally, we analyze a smaller higher spatial density dataset collected by Shell in 1984 (B-388-84SC-3D) that overlaps the Chevron volume. The 69 km^2 survey footprint is rectangular and oriented with the longer dimension sub-parallel to the shelf break and nearly perpendicular to the Palos Verdes Fault strike with bin spacings of 25 and 12.5 m, respectively in the inline and crossline directions. The seismic processing was previously completed on both volumes and are post-stack and migration was performed, with spectral ranges of 5 - 60 Hz. Additionally, the data had gain correction applied to equalize the intrinsically attenuated signal with depth before public release.

In addition to the 3D seismic data, we use higher resolution 2D airgun multi-channel seismic lines that intersect the 3D volumes to quality check structural and stratigraphic features observed within the 3D volumes. The 2D profiles were collected by WesternGeco in 1981 (W-30-81SC-2D, 20 m shot spacing, 6 s record length, 4 ms sample rate). Lastly, we use exploratory geophysical well logs and lithology logs (Fig. 2-1 & B-1) that were acquired from the Bureau of Safety and Environmental Enforcement through a Freedom of Information Act request (See Appendix 1-B). In order to incorporate well lithology logs recorded in depth into the seismic volumes in two way travel time 1D velocity models were calculated for each well located within the volume (see Appendix 1-B & Fig. B-1.). With well lithology logs (unconformity contacts) converted to two-way travel time seismic horizons could be mapped within the 3D volumes.

2.3 Methods & Results

2.3.1 Data conditioning

The methods and workflow are outlined schematically in Fig. 2-2A. First, all seismic SEGY navigation headers were converted from North American Datum 1927 State Plane Zone 6 to Universal Transverse Mercator Zone 11 N and imported into seismic interpretation software, OpendTect. The seismic data were preprocessed using dip-steered diffusion filtering in order to reduce noise and increase lateral continuity of reflectors while retaining discontinuities (Chopra and Marfurt, 2008). This attribute applies median filtering in a moving 3D window (inline, crossline, and time-window) following structural dip in areas with shallow to moderate dipping

reflectors and areas with very steep dips are not median filtered. This approach reduces smearing of median filtering across faulting discontinuities and retains sharp images of faults (Marfurt et al.,1998; Tingdhal and de Rooij, 2005). The Palos Verdes Fault is clearly delineated by vertical offset of reflectors and folding surrounding the fault (Fig. 2-3).

9) 2-2 Workflow for 3-Dimensional Fault Detections

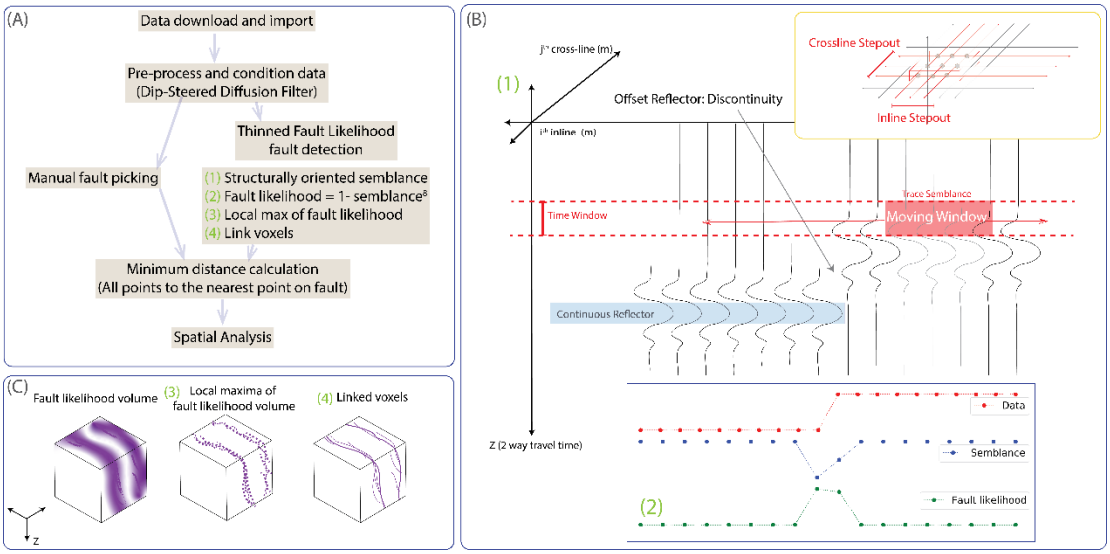

2.3.2 Manual Fault & Horizon Mapping

Three dominant fault strands that are a spatial reference for the study were manually mapped throughout the volume in the sedimentary rock. The fault could be

mapped continuously with high confidence in the depth range 350 m - 2.2 km, we selected this depth range to avoid low signal-to-noise in the basement (depth > 2.2 km), and processing artifacts related to multiple suppression in the shallow section (< 500 ms two-way travel time). High resolution 2D seismic lines were used to guide manual picking and for quality control (Fig. 2-1, B-2). The first fault picking pass was completed picking on 500 m spaced inlines (roughly perpendicular to fault) then refined using the combined 2D and 3D datasets (Fig. B-2). The fault picks were interpolated to form three continuous 3D fault surfaces which is consistent with detailed geomorphic and sub-bottom mapping (Brothers et al., 2015; Walton et al., 2020).

Six key horizons were mapped throughout the volumes, in order to evaluate the damage zone by sedimentary lithology. These horizons were carefully constrained in depth by tying to lithologic boundaries identified in 13 lithological and paleontological well logs (Fig. 2-1, B-1, B-3). The lithology contacts in measured depth were converted to two-way travel time by integrating the coincident velocity logs for each well and were then used as constraints on horizon mapping (Fig. B-3). Horizon mapping was done by manually picking laterally continuous reflectors that begin at well contacts that are outside of the fault zone and carefully mapping and connecting to well equivalent contacts within the fault zone, but not crossing the central fault strand. Six horizons (Pico Lower, Repetto Upper, Repetto Lower, Monterey Delmontian, Monterey Mohnian, and Catalina Schist Basement) were mapped east of the fault starting at well P0302-2 (Fig. 2-1) and are relatively flat

lying throughout most of volume east of the fault, but are concave up near the fault. Only the 3 oldest contacts (Monterey Delmontian, Monterey Mohnian, and Catalina Schist Basement) were mappable west of the fault because the younger units have been uplifted with the Palos Verdes Anticline and subsequently eroded away (Wright, 1991; Sorlien et al., 2013). The mapping of the units on the west side of the fault started at wells P0304-1 and P0295-3 (Fig. 2-1) at the western edge of the Chevron volume, continuing east to the central fault strand. The morphology of the horizons west of the fault are more complex and folded as part of the anticline, with the axial surface sub-parallel to the Palos Verdes Fault and plunging to the southeast.

2.3.3 Automated Fault Detection

We use the thinned fault likelihood algorithm to automate identification of faults and fractures within both seismic volumes (Hale, 2013) and compare these results with the manually interpreted fault strands (Fig. 2-2). Thinned fault likelihood uses structurally guided semblance (a measure of multitrace similarity over a time-window) to scan adjacent traces and identify discontinuous regions, over a moving space-time window (Fig. 2-2b). Here we use a filter window size of 2 inline / 2 crossline and 32 ms. The local maxima of the semblance volume are preserved, thinning the discontinuous regions (Fig. 2-2c.). These local maxima voxels are then scanned over geologically reasonable dips and azimuths (strikes within +/- 40 degrees of the Palos Verdes Fault and dips in the range of 70 - 89 degrees) for adjacent high dissimilarity voxels which are then linked, forming a fault and fracture network. An example of the results of thinned fault likelihood can be seen in Fig. 2-3. The

resultant thinned fault likelihood volume has a likelihood (0-1) for each 3D voxel of being a fault or fracture.

10) 2-3 Comparison of Conditioned Data with Fault Detections

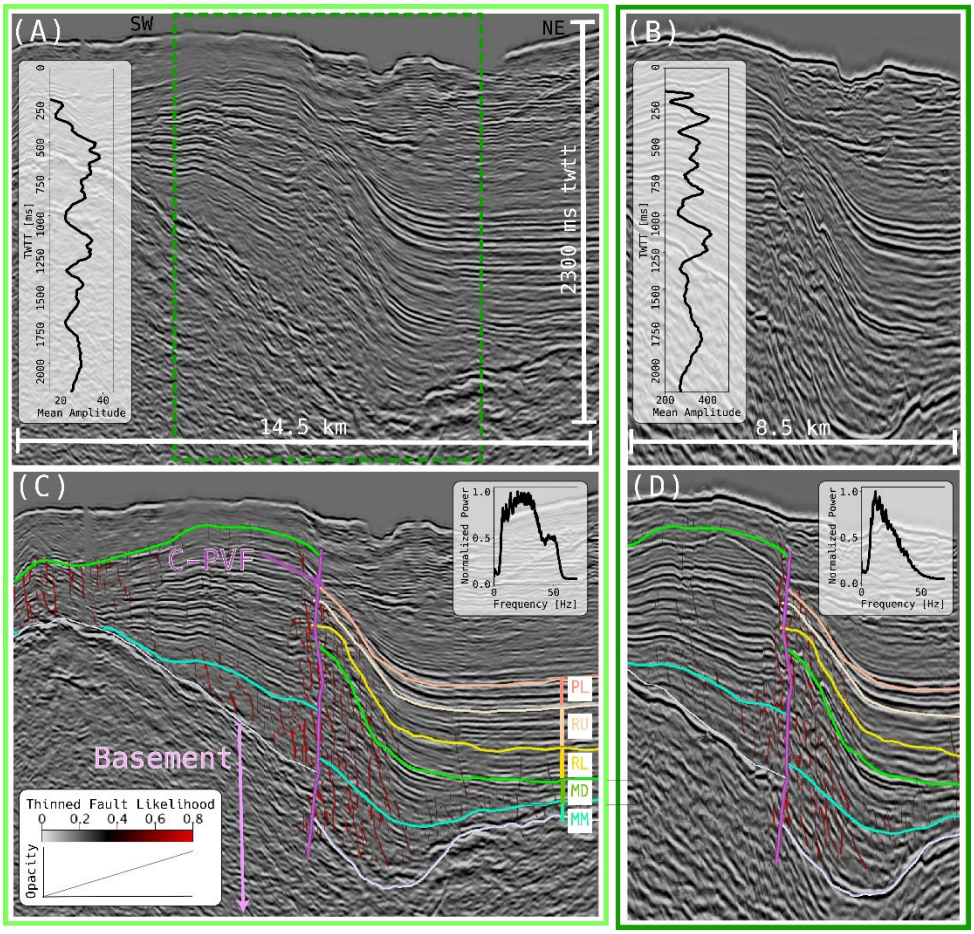

Fig. 2-3. Comparison of conditioned data and thinned fault likelihood results from overlapping portions of the Chevron (left panels) and the Shell (right panels) seismic volumes. Showing processed (dip-steered diffusion filtered) seismic inline number 1270 both uninterpreted (A & B) and with manual interpretation and fault detection (C & D). Map view of line location is shown in Fig. 2-1. The dashed dark green line in the (A) shows the extent of the Shell line. There is a 9000 m/s vertical exaggeration applied to help highlight the vertical offsets along the fault. The Palos Verdes Fault is clearly shown by offset reflectors, folding, and deformation features. (A & B) Dimensions are indicated by the white bars, and the inset indicates the mean amplitude as a function of two-way travel time (depth). (C & D) transparent to red overlay is the thinned fault likelihood attribute, where red is the high dissimilarity or

high likelihood of being a fault. Purple sub-vertical line is the central Palos Verdes Fault strand (C-PVF) and the rainbow-colored sub-horizontal lines are three-dimensional (3D) horizons at the inline (PL - Pico lower, RU - Repetto upper, RL - Repetto lower, MD - Monterey Delmontian, MM - Monterey Mohnian). The inset shows the normalized power spectra for each survey.

2.3.4 Spatial Analysis

To examine how fracturing varies spatially, we calculate the binned average probability of a fracture being present as a function of distance from the central fault strand and each of the horizons. Given the large dataset, efficient calculation of distances is important to implement. We calculate the minimum distance from each voxel ($N_{Chevron}$ = 4.8 x 10^8; N_{Shell} = 1.2 x 10^8) in the volume to the mapped fault surface (N = 2 x 10^6) and each of the horizons (N = 8.9 x 10^5 / horizon), using a nearest neighbor ball-tree approach. This is an unsupervised learning method designed to find a point in a given set that is closest (in this case, Euclidean distance) to the given point. The ball tree method subdivides the dataset into a tree structure of overlapping spheres that increases the efficiency of the nearest neighbor calculation. As with manual fault mapping (section 2.3.2), we limit our analysis to depth ranges of high-quality data that are above the basement and below the pico-middle/pico-lower unconformity due to low signal to noise ratios in the basement and artifacts introduced in the shallow subsurface due to multiple suppression efforts.

11) 2-4 Perspective View of Fault Detections in 3-Dimensions

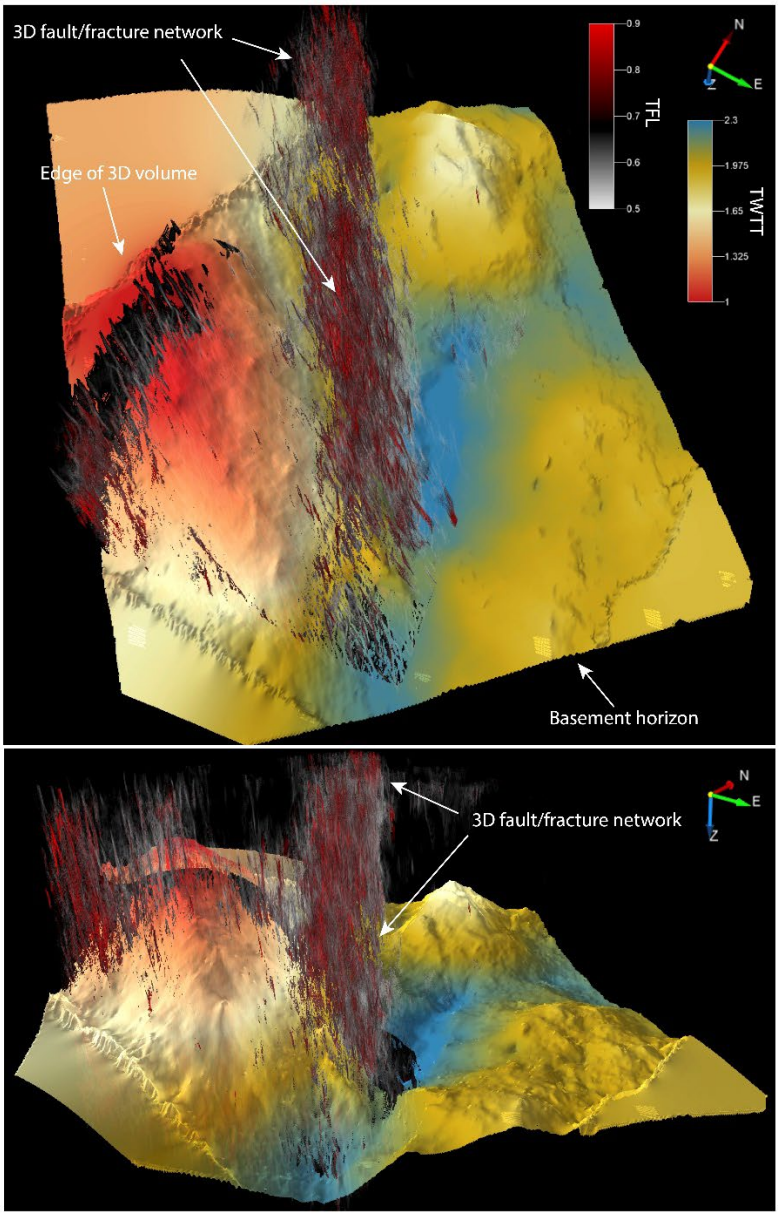

Fig. 2-4. Perspective view of thinned fault likelihood (TFL) attribute results for the Chevron volume along the Palos Verdes Fault Zone. The transparent to red color scale range indicates probability of a fault, where fault probabilities < 0.6 are transparent. The basement horizon surface is shown with a blue to red color map indicating depth in two-way travel time (twtt in seconds). (top) Map view (bottom look direction pointed out in Fig. 2-1) is an along strike perspective view. Note the width variability of the damage zone along strike, and the complex detected fault geometry and structures.

We bin the data spatially by distance from fault to examine spatial relationships of thinned fault likelihood probability. In each bin, the mean probability *P* is,

$$(1)\quad \langle P \rangle = \sum p_i / N$$

where *p* is the probability of the *ith* voxel being a fault (within prescribed spatial bin), *N* is the number of voxels in the spatial bin and angle brackets denote the mean. Note that the bins have varying numbers of voxels, thus the normalization by *N* is necessary. For conciseness, we will refer to the bin-averaged value *P* as simply fault probability for the rest of this study.

First, we examine the data as a function of this distance from the fault, to explore the lateral distance dependence of damage. The large number of data points (~ 10^8) allows for narrow bin widths, here we use a bin width of 25 m and find that different bin sizes do not impact the results (Fig. B-4). Fig. 2-5 shows a clear relationship between fracture probability and lateral distance from the fault in which the fracture probability decays to a stable background value at 2 km distance from the central strand of the fault for both seismic volumes. This macroscopic damage zone is likely the superposition of the damage decays of all faults near the central strand (section 2.4.5). The data appear to obey exponential scaling up to ~ 2 km, and can be well represented in this region by,

$$(2)\quad P = C10^{(-x/x0)}$$

where x is the perpendicular distance from the fault surface, $x0$ is an exponent that we will call the decay distance and C is a fault specific constant. A least square fit to the data yields $x0$ = 3540 m and 3200 m for the Chevron and Shell volumes, respectively. We calculate the background fracture probability, B as the mean of fracture probability of distances between 2000 – 3500 m. We bootstrapped the error on the parameters $x0$, C, and B, and these are provided in table 1 (see Fig. B-5 & B-6 for distributions).

12) 2-5 Relationship of Fracture Probability with Fault Distance

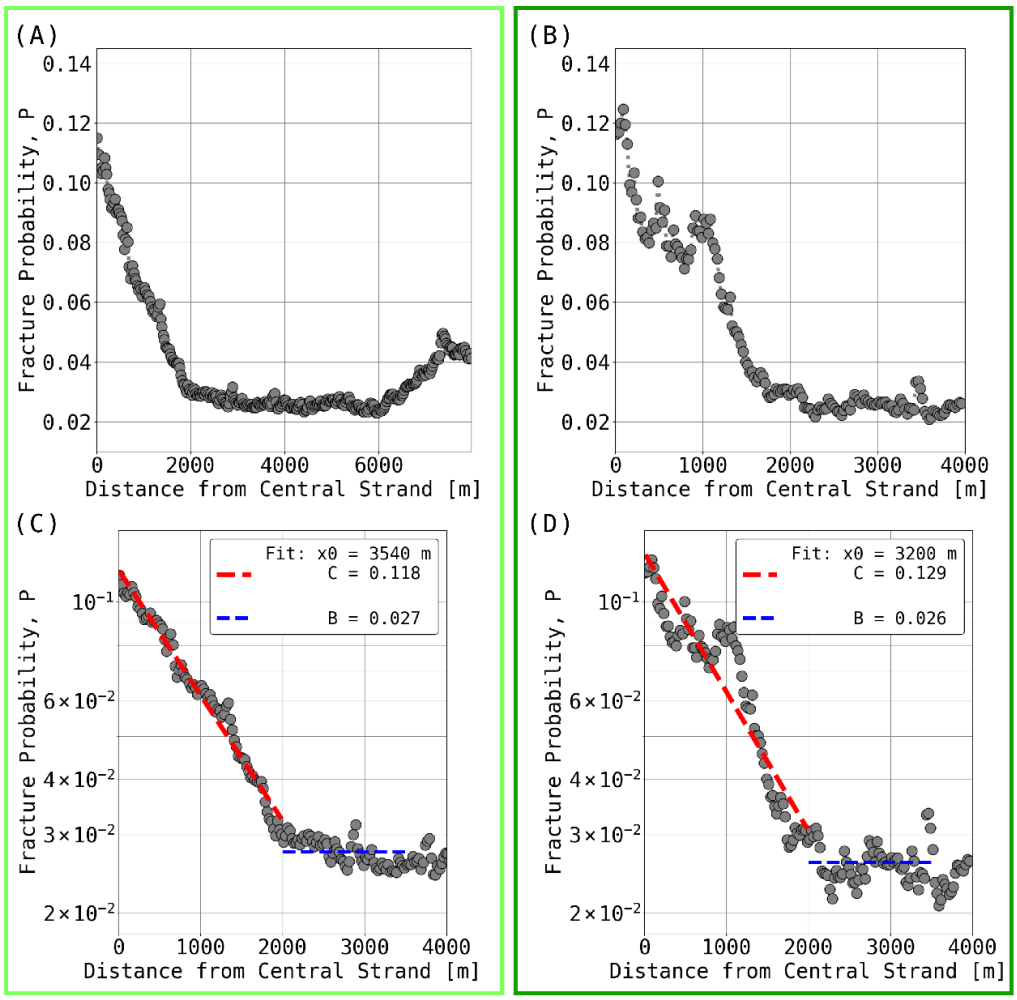

Fig. 2-5. (top) Fracture probability relationship with distance east of central mapped strand. Fracture probability decays with distance east from the central strand to ~2 km from the fault. (A & C) shows the Chevron volume results (B & D) show the Shell results. (A & B) are in linear space and (C & D) the Y-axis are in log space. The background, low fracture probability, begins at 2 km and at distances greater than 6 km fracturing likely increases due to the Wilmington Fault (and its damage zone, see Fig. 2-1) at the eastern edge of the seismic volumes. (C & D) Shows the exponential relationship between fracture density and distance from the central strand. Red line indicates the least squares exponential fit through the damaged region to 2.0 km, and the blue line shows the background level. The outer edges (2 km) were chosen as the clear change in slope. Variables *x0* and *C* are defined in equation 2.

Next, we investigate the effects of lithology on damage surrounding the fault. The mapped lithology contact horizons (see section 2.3.2) were used to constrain voxels in 3D space and to analyze fracturing between vertically adjacent horizon surfaces (Fig. B-7). We calculate fault probability binned by distance from the central fault, for each of the 5 sedimentary lithologies using equations 1 & 2. Fig. 2-6 shows the results, and each lithologic unit is again well fit by an exponential relationship, similarly to the bulk trend (Fig. 2-5), and the general decay and background trends are similar between the two volumes. There are unique exponential trends and background fracture probabilities for each unit. The larger Chevron volume represents 17 km along strike averaged results and the smaller Shell volume represents 4.5 km along strike and exhibits increased variance in the damage decay and the background, to be discussed more in section 2.4.4

13) 2-6 Fracture Probability by Lithology

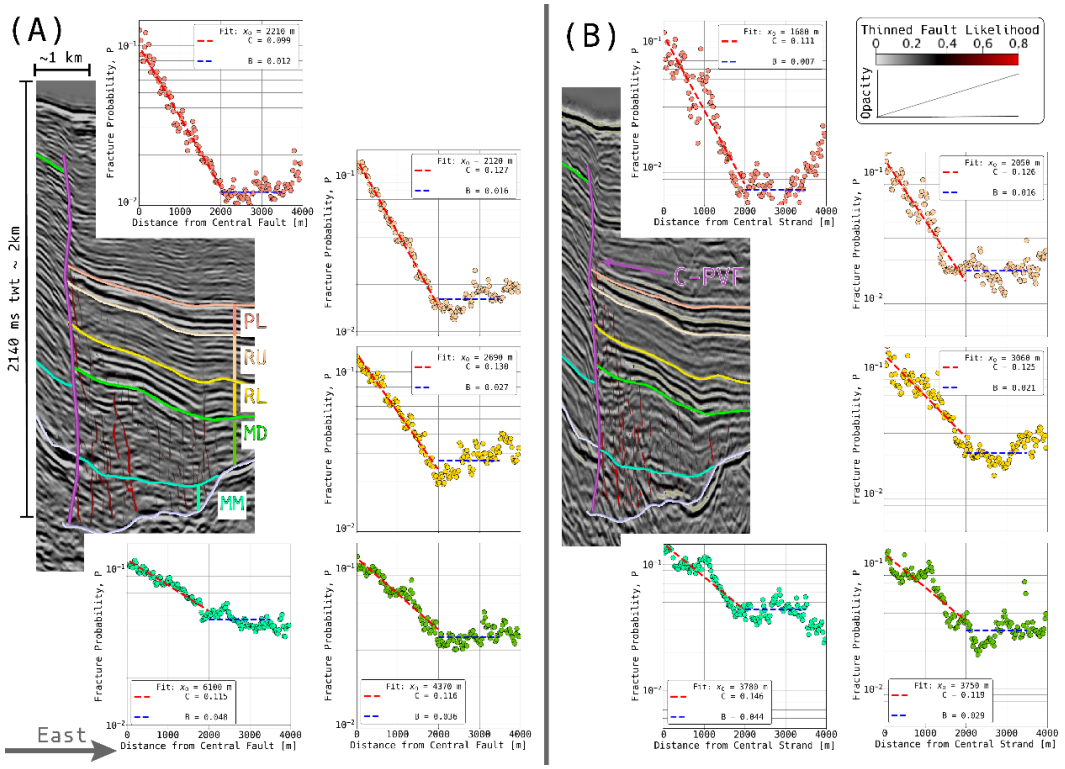

Fig. 2-6. The left side of each figure shows a representative example of dip-steered diffusion filtered seismic inline 1340 data in black and white color scale (line location shown in Fig. 2-1). The overlain vertical purple line represents the manually mapped central strand. The transparent to red is the thinned fault likelihood fault detections and transparency indicated. The multi-color horizontal lines are mapped three-dimensional (3D) horizon-surfaces and mark lithological contacts or unconformities that have been tied to well logs (PL - Pico lower, RU - Repetto upper, RL - Repetto lower, MD - Monterey Delmontian, MM - Monterey Mohnian). These horizons are used as upper and lower bounds to constrain the fracture probability as a function of distance away from the fault for each lithology in full 3D space, not just at the example inline. (A) are the Chevron volume results, which are shown in the semi-log plots on the right of the seismic line, colors match the lithology units indicated on the seismic line, and data are averaged over - 17 km along strike. (B) shows the results for the Shell volume and are averaged over 4.5 km. Note the different exponential fit slopes (red line) and background (blue line) for each geologic unit (horizontal portion).

The pervasive fracturing observed in the Monterey Formation is consistent with previous studies that show that the Monterey Formation is brittle (Bramlette, 1946;

Behl, 1999). There appears to be a tradeoff between damage decay and overall background damage (horizontal portion of the plots) that yield a remarkably consistent damage width (intersection of decay slope with background) in all units, which is discussed in greater detail in section 2.4.4.

Finally, we compare the damage zone on the east and west sides of the fault in the two Monterey units (Delmontian & Mohnian) that are mappable on both east and west sides of the fault (Fig. 2-7). We analyze the Delmontian and Mohnian, Monterey Formations, on an east versus west comparison and the results are shown in Fig. 2-8. Here we calculate the fault probability in the Chevron and Shell volumes over 11 km and 4.5 km of fault length, respectively. We find increased variability in the decay trends and the background as we examine shorter segments of the fault. The shorter fault length analyzed in the smaller Shell volume exhibits more complexity in the decay of fracturing with distance in the units. When we search for the optimal background distance D it becomes apparent that we are resolving 2 fault strands, which present as peaks in fracture probability at 0 and about 1 km distance east of the central fault strand. For the short 4.5 km section (Shell volume) of the fault we fit from the eastern trend using the peak in fracture probability east of the central fault strand (1 km distance away), while the western trend is fit with respect to the central strand. This results in east and west fits for the slopes X_o and distance cutoffs D that are similar on both sides of the fault.

2.4 Discussion

2.4.1 Validity of P as a measure of fracturing

The thinned fault likelihood method appears to successfully identify faults and fractures within the 3D seismic volumes (Fig. 2-3, 2-6 & 2-7) and identify features within the data that seismic interpreters would routinely identify as a fault zone, such as offset reflectors and change in reflection characteristics (Iaccopini et al., 2016; Alcalde et al., 2017) (Fig. 2-3). Additionally, the highest fault likelihood regions localize around faults identified in this study and independent mapping efforts as the Palos Verdes Fault (Brankman and Shaw, 2009; Sorlien et al., 2013; Walton et al., 2020). There is also good agreement on the location and the identification of the damage zone with thinned fault likelihood in both 3D volumes and on the 2D seismic lines (Fig. B-2), that were independently collected and processed, reducing the possibility that the method is measuring a data artifact. Finally, the fundamental finding that fault probability is highest at the location of the primary fault strand supports the validity of using this method to measure fault structure.

14) 2-7 Fracture Probability on Horizons (Unconformities)

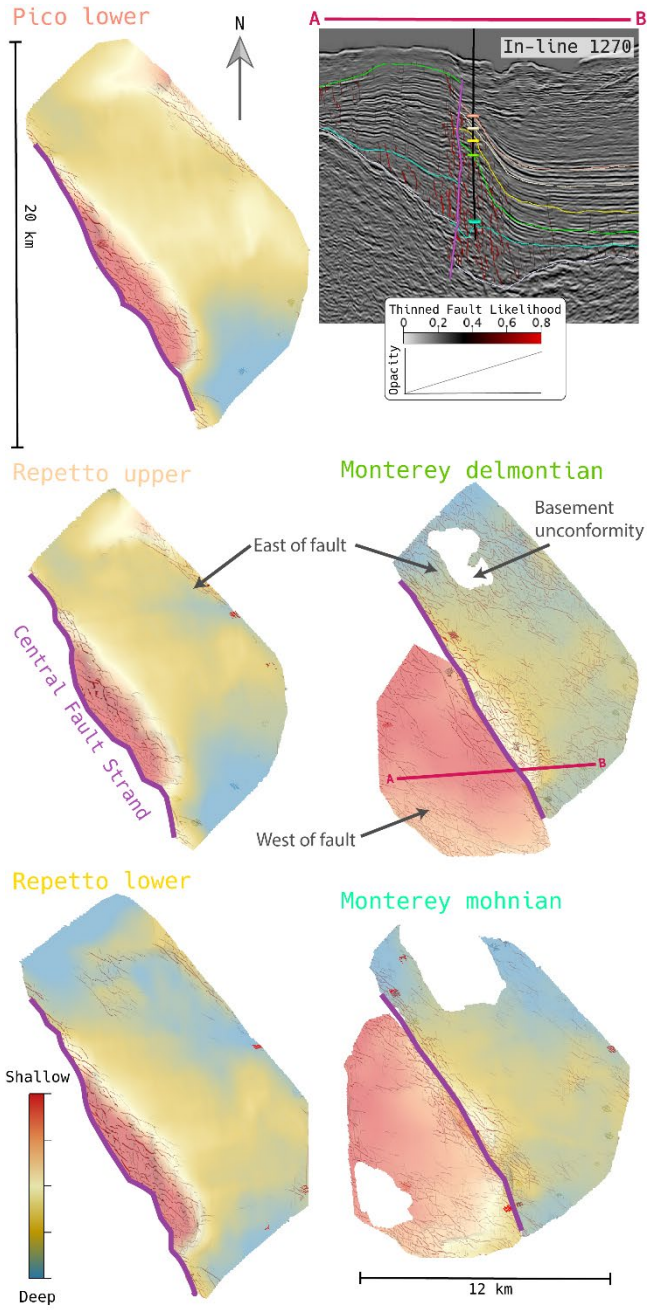

Fig. 2-7. Showing the results of thinned fault likelihood fault detection projected on mapped three-dimensional (3D) horizons, shown in map view. The thinned fault likelihood color map grades from transparent at 0 to red at 0.8 chosen to highlight the localization around the fault. The color map on the Chevron horizon surfaces ranges

from red to blue, indicating shallow to deep in two-way travel time relative to each layer. The horizons have been cropped in-lines (500-1400) and crosslines (950-1900). The central fault strand is colored purple, the western fault strand in dark purple, and the eastern fault strand in navy blue. (Upper right) inset shows a Shell volume inline 1270 (location shown in Fig. 2-1) cross-section through the data where the gray scale seismics that have dip-steered diffusion filtering applied. The colored lines represent mapped horizons, and the colors correspond to the labels on the map view horizons.

2.4.2 Density – Distance Relationship

We find that the fracture probability decreases with distance from the fault and is best fit by an exponential curve, with a decay distance of ~ 3000 m. This observation is of the same functional form as those observed in outcrop studies though cannot be compared directly because of different metrics and methods used in fracture characterization (Faulkner et al., 2003; Mitchell and Faulkner, 2009). Distinguishing exponential and power-laws relationships is not straightforward, and it is advised to span several orders of magnitude before determining the appropriate functional form (e.g., Bonnet et al., 2001). Results from this study span 3 orders of magnitude (10^1 - 10^3 m) of distance and an order of magnitude of fault probability, and as we extend our study up to 8 km from the fault for the Chevron dataset and 4 km for the Shell dataset. These observations are at distances from the fault that are seldom accessible in outcrop studies (typically hundreds of meters in rare cases up to a few kilometers) (Faulkner et al., 2003; Savage and Brodksy, 2009). Seismic acquisition and binning results is a low-pass filter on the data and smaller scale fractures, commonly counted in outcrop transects, are not recoverable (see Appendix 2-B). Unique to this method and study is the clearly defined edge of the fault damage zone, which agrees with damage zone models, where the damage decay intersects a stable background (from

tectonic stresses). This edge occurs at ~ 2 km east of the central strand (Fig. 2-5), and provides a robust distance cut off for fitting.

In this study the damage zone is examined fully in 3D and is not restricted to the 1D or 2D surfaces of previous surficial studies (Chester and Logan 1986, Berg and Skar, 2005; Sagy et al., 2009). We show that the along-strike averaged faulting and fracture probability, over the depth ranges bound by the pico-lower and the basement contacts (~ 400 - 2200 m depth, several kilometers above the seismogenic zone) exhibits exponential scaling. We are capturing the behavior of the damage zone at large length scales and show that the exponential decay relationship extends to at least 10^3 m length scale from the central fault strand.

2.4.3 Damage Zone Width

The data indicate the half width of the Palos Verdes Fault is 2 km, or 4 km total width. The width determined is indicated by the clear break in slope shown in Fig. 2-5 defining a clear boundary between the fault and the relatively undisturbed basin to the east. As shown in Table 1 and Fig. 2-6, there is an apparent tradeoff between the decay of fault and fracture probability with distance and the fracturability of the background that result in a surprising stability of the damage zone width throughout different depths and lithologies. The intersection of the damage trend with the background occurs at ~ 2 km from the center of the fault for all layers that differ in composition, age, and depth (Fig. 2-6). This indicates that the overall along-strike average (17 km along strike) width is instead a function of an attribute intrinsic to the

Palos Verdes Fault (e.g., length, fault maturity, or number of active strands). The damage zone width identified here is wider than may be inferred from studies of the damage zone width's dependence on displacement (Fig. B-8).

The width identified in this study is slightly wider than the 1-2 km widths inferred in some passive seismic tomographic studies (Thurber et al., 1997; Cochran et al., 2009; Yang et al., 2011). These studies approximate the damage zone as a zone with up to 50% reduction in P and S wave velocities, that extend to depths of at least 5 km. These studies also find an increase in Vp/Vs ratios within the seismically identified damage zone suggesting that the fractured damage zone is fluid filled. The similar width of these studies to our present study is reassuring given the differences in methods and resolution (tomographic grid sizes are typically ~ 1 x 1 km compared to bin sizes of 50 x 25 m and 25 x 12.5 m in this study, see Appendix 2-B). The passive seismic studies hinge on seismic body wave ray paths to sample the fault zone and thus are limited in their resolution and spatial sampling. In contrast the present study has uniform sampling throughout, thus may be more resolving of the outer bounds of the damage zone. In addition, tomography studies use deviations in wave speed that may evolve with fault healing as a proxy for damage, whereas in our study we use high fold (high source/receiver sampling) direct reflection imaging to identify the damage zone. We are directly imaging the damage associated with the fault, through reflection discontinuities and abrupt changes in amplitude character, and propose that this method may be more sensitive to more subtle damage and thus delineates a wider damage zone.

Our measurements of fault zone width are also larger than those inferred from passive seismic studies that utilize fault-zone trapped head waves that are critically reflected at the boundary between damaged and undamaged rock (Li et al., 1997; Ben-Zion et al., 2003; Li et al., 2004; Yang et al., 2014; Li et al., 2016). These studies find a narrower, several hundred-meter-wide damage zone, that extend to at least 5 km depth. One could speculate that the fault zone trapped wave is sampling the width of an inner fault damage zone rather than the outer edge of the fault damage zone. Lewis and Ben-Zion (2010) showed that fault trapped waves are not ubiquitous along strike in the mature (Parkfield) section of the San Andreas Fault. These studies rely on forward modeling of the waveform and travel times and may be non-unique in their parametrization (Ben-Zion, 1998). In addition, the inherently sparsity of passive seismic studies leads to spatial averaging of parameters.

The damage zone width in this study is about a factor of two wider than the 2-km compliant off fault damage zones inferred in other studies based on geodetic measurements (Fialko et al., 2002; Fialko, 2004). The geodetic studies used the response of terrestrial strike-slip faults to nearby earthquakes to infer reduced elastic moduli near the faults that were interpreted as indicative of damage zones. Like in this study, the geodetically inferred damage zones on the order of kilometers.

Most geologic outcrop studies find a narrower fault damage zone width than the present study. Outcrop studies are a direct ground truth of the geology; however, exhumed surficial exposures are scarce, limited in scope, and transects are 1D in most

cases. We speculate that many of these studies are missing the outer edge of many superposed damage zones, and in some cases may mis-interpret a local minimum in damage as the background fracture density (outer limit of the damage zone). In many cases exposure and sampling prohibit observation of the true damage zone edge, which we find to be several kilometers from the fault core along the Palos Verdes Fault.

The damage zone width in this study is similar to the width identified in another active source attribute study of a strike slip damage zone (Liao et al., 2019). Liao et al. (2019) found a damage zone width of ~1600 m using structurally oriented seismic coherence (analogous to semblance) of the El Reno Fault in Oklahoma and fit an exponential to their data (Fig. B-9). The approach of the Liao et al. (2019) study maps coherence on 11 2D cross sections in an on-land 3D seismic volume of similar spatial resolution to this study (bin spacing 33.5 x 33.5 m) and show 2 distinct along strike trends that are fit with an exponentials that decay more steeply with distance from the fault than our analysis (Fig. B-9). The discrepancy in the width between these two studies may be due to the maturity of the faults. The El Reno Fault is 32 km in length and the Palos Verdes Fault is 100 km. Another similar study of 6 immature normal faults (<3 km in length and 100s of meters of displacement) in the Bohai Bay Basin in China, which also used similarity-based attributes on 2D cross sections in 3D volumes, found damage zones in the range of 200 - 400 m (Liao et al., 2020). Their damage decay with distance was fit using a power law, and the comparatively narrower damage zone width is again potentially a function of fault maturity.

2.4.4 Sedimentary Rock and Damage

Lithology along the Palos Verdes Fault appears to play a role in the decay of fracture probability with distance from the fault and the level of background fracturing. The background fracture probability (stable region beyond 2 km) increases with increasing stratigraphic depth. Background fracture probability generally increases from shallow to deep. This result suggests that the first-order impact of damage in sedimentary rock in depths ranging from 400 - 2000 m is determined by depth, age, or fault growth. The systematic change in damage decay and background with increased depth and normal stress may support the prediction that damage is controlled by confining pressure from of overburden (Scholz, 2000).

The Monterey Formations (Delmontian and Mohnain) are the thickest and have the greatest integrated damage. One plausible explanation could be the effect of unit thickness on joint spacing correlation (Hobbs, 1967; Narr and Suppe, 1991). Large joint or fault spacing could be more detectable with seismic methods, however, the overlying lower Repetto Formation is one of the thinnest units and has high integrated damage. Alternatively, the documented enhanced brittleness intrinsic to the Monterey Formation (Eichhubl and Behl, 1998; Behl, 1999; Eichhubl and Boles, 2000) may allow it to accumulate more damage. Additionally, these formations have experienced more cumulative displacement, thus accumulating more damage.

The importance of geology on fault damage has been suggested (Caine et al., 1996; Shipton and Cowie, 2003; Kim et al., 2004; Berg and Skar, 2005). However, it

is not clear how lithology impacts the damage trends in this study. Here the units are all siliciclastic sedimentary rock and maybe too similar to differentiate a lithologic dependence at the resolution in this study.

Table 1 - Exponential Fracture Probability Parameter Fits

Data	*x0 (m)*	+/-	*B*	+/-	*C*	+/-	Description
Chevron volume	3540	64	0.027	0.0002	0.118	0.001	Complete volume from Pico to basement
- Pico – lower	2210	48	0.012	0.0002	0.1	0.003	Pliocene interbedded silt and sandstone
- Repetto upper	2120	27	0.016	0.0003	0.127	0.002	Pliocene sandstone and conglomerate
- Repetto lower	2690	72	0.027	0.0006	0.13	0.003	Pliocene medium to coarse sandstone and siltstone
- Delmontian	4370	172	0.033	0.0006	0.116	0.002	Miocene diatomaceous & high silica
- Mohnian	6100	251	0.047	0.0006	0.115	0.002	Miocene thinly bedded chert and shale
Shell volume	3200	115	0.033	0.0003	0.103	0.004	Compete volume from Pico to basement
- Pico – lower	1680	67	0.007	0.0002	0.111	0.008	Pliocene interbedded silt and sandstone
-Repetto upper	2050	70	0.016	0.0004	0.126	0.006	Pliocene sandstone and conglomerate
- Repetto lower	3060	195	0.021	0.0005	0.125	0.007	Pliocene medium to coarse sandstone and siltstone
- Delmontian	3750	206	0.029	0.0011	0.119	0.005	Miocene diatomaceous & high silica
- Mohnian	3700	176	0.044	0.0009	0.146	0.005	Miocene thinly bedded chert and shale

2.4.5 East vs West Comparison

It has been argued that observations of a broad distributed damage zone are a result of the superposition of multiple sub-parallel fault strands with a cumulative effect resulting in a wider zone of damage (Mitchell and Faulkner, 2009; Savage and Brodsky, 2011). Our data may support this model because there are at least 3 continuously mappable fault strands and other subsidiary strands identified by the algorithm. We find a particularly smooth decay of damage with distance (Fig. 2-5 & 2-6) in the Chevron volume that is averaged over longer along strike distances (~17

km) and more variability in the decay trends in the Shell volume that represents a shorter fault length (~4.5 km). There is a distinct peak in fracture probability at 1 km distance from the central fault strand in the Shell volume (Fig. 2-5, 2-6 & 2-8) that corresponds to the eastern fault strand that has been previously documented (Walton et al., 2020). This additional fault strand is apparent in the portion on Chevron data that overlaps Shell volume (Fig. B-10). Resolving multiple fault strands suggests that the damage zone superposition model is likely accurate, and that the additive impact of multiple anastomosing secondary fault strands and associated damage zones creates a smooth decay.

The variability of the damage decay trend at shorter distances makes comparing east versus west a bit tenuous; however, it is clear that on both sides of the fault fracture probability decreases with distance from the central fault strand. The decay on both sides may be fit with an exponential, and for the 4.5 km fault length segment that displays a clear influence from the eastern fault (right side of Fig. 2-8), we can fit the western trend and the outside of the eastern fault strand with roughly the same parametrization. One could argue that the similarity in the decay trends tells us that both strands have a similar faulting history (displacement, number of slip events, etc.) or that these two strands have similar damage decays independent of their history, though this effect cannot be determined from the data. Finally, we find that the background fracture probability is higher on the west side of the fault. We think that this could be due to the increased deformation associated with the Palos Verdes anticline uplift that includes more time integrated tectonic damage.

15) 2-8 Fracture Probability East & West of Fault

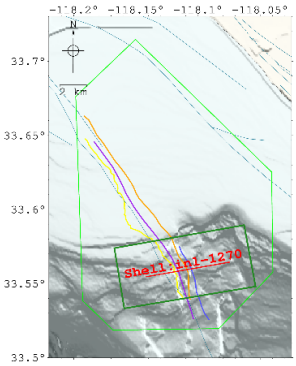

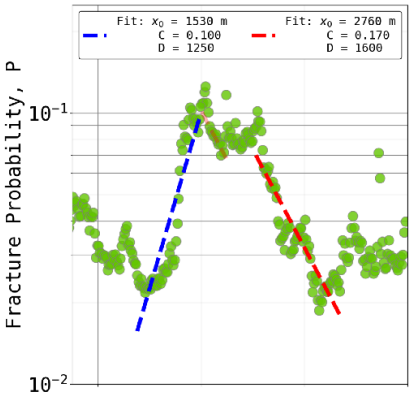

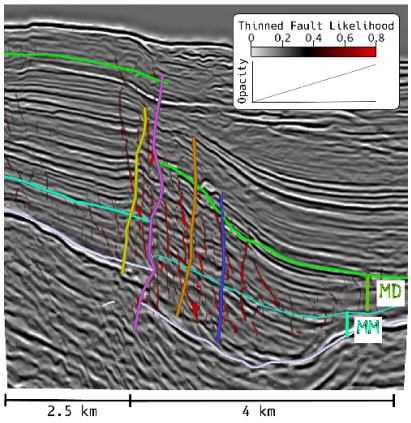

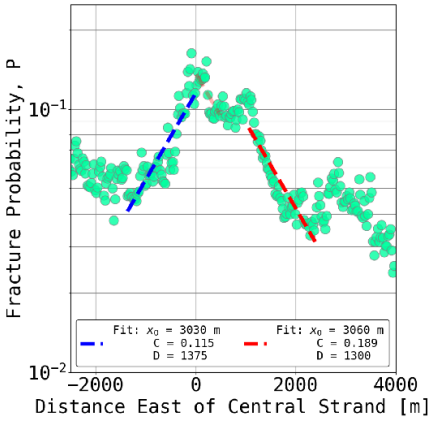

Fig. 2-8. Showing fracture probability as a function east of the central fault strand. The inset map in the upper left shows the bounds of the shell volume in dark green which the data are averaged over. The solid yellow, purple, orange, and blue lines on the map show the western, central, eastern, and eastern 2 fault traces respectively. The dark redline indicates the location of the example seismic line below (lower right). Where the mapped green (MD – Monterey Delmontian) and cyan (MM – Monterey Mohnian) sub horizontal lines indicate the unit boundaries or unconformities, mapped to the central fault strand shown as the sub vertical purple line. The top plots with green circles are the Monterey Delmontian Formation. The middle panels show example inlines for the volumes, Indicated on the map. The bo–tom plots with teal circles show the fracture probability results for Monterey Mohnian Formation. See text for more details.

2.4.6 Folding and Damage

Like most faults, the Palo Verdes is accompanied by folding yet our discussion thus far has only focused on the faulting and its brittle damage. Visual inspection of the data (e.g., Fig. 2-3, 2-7 or 2-8) suggests that the edge of the fold abutting the fault corresponds to the edge of the damage at about 2.1 km from the central strand (Fig. 2-9). We can further refine this initial observation by measuring dip and comparing it to damage. Specifically, we calculate polar dip in full 3D space at each voxel using inline and crossline dips calculated in section 2.3.1 with dip steering (Tingdahl and De Rooij, 2005) and utilize the square root of the sum of the squared inline and crossline dips. This provides us with the magnitude of the apparent dip since the seismic volumes are in time, and dips are in units of [us/m]. This provides the magnitude of the dip, but no direction information; however, the morphology of the bedding contacts is simple and generally dips to the northeast with dip decreasing away from the fault (Fig. 2-7.) Fig. 2-9 reinforces the inference that the fold and damage are co-located.

Thus, some natural questions emerge about the relationship between the damage and folding. Is the damage only indirectly controlled by the fault and more directly created by the fault-generated fold? Alternatively, is the extent of the fold controlled by the extent of the weakened, damaged zone?

If the folding is the direct cause of the damage, we would expect the damage to be tensile and highest where the strain produced by folding is highest. The detected damage features are sub-vertical, thus a sub horizontal tensile strain would be required. Folding produces such strains that are proportional to curvature. The data do not support this possibility. Fig. 2-9 suggests that curvature is not well-correlated with damage in this particular 2D section. In fact, the edge of the fold is the locale of highest curvature, and it corresponds to reduction, rather than increase, of damage.

This preliminary interpretation is supported by a more thorough analysis considering the potential 3D aspect of the geometry (Fig. 2-9). The mean curvature (mean of the maximum and minimum curvatures) is an appropriate measure for this situation (Roberts, 2001). An alternative metric would be Gaussian curvature (Lisle, 1994), but Gaussian curvature is inappropriate for a cylindrical fold because it is very unstable when the minimum curvature measure is close to zero (Mynatt et al., 2007; Nabavi & Fossen, 2021). Here we calculate mean curvature in a spatial kernel of 10 inline and crossline bins assuming a constant velocity of 2,500 m/s. Other velocities and spatial kernels were tested and did not change the results. We compare the along strike averaged mean curvature to fracture probability from section 2.3.4 (Fig. 2-9).

The results reinforce the preliminary interpretation. The curvature is not highest where the damage is highest. The bending strains are unlikely to be the primary cause of the damage.

Instead, we suggest that the width fold is likely limited by the damage. Damage weakens the rock and makes it more susceptible to ductile deformation.

16) 2-9 Correlation of Fault Damage and Fold

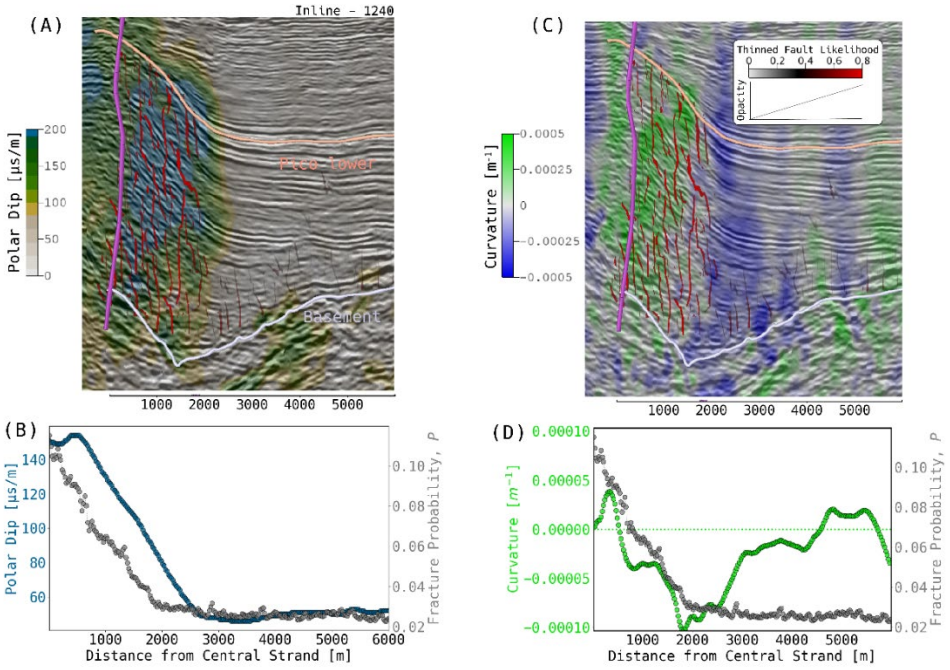

Fig. 2-9. showing the correlation between the nearby fold and the damage zone. (A & C) shows a single two-dimensional (2D) example seismic inline with polar dip and curvature shown, respectively. Note, (B & D) are averaged over the volume. (A) depicts polar dip for the 2D example line where tan, green, blue color map transparency (50%) shows the calculated polar dip that decreases with distance from the fault into the sub-horizontal basin to the east. Overlain in transparent to red color are fault likelihood probabilities, displayed between the lower Pico horizon and the Basement that are shown in pink and light purple. The darker purple sub-vertical line is the central strand of the Palos Verdes Fault. (B) shows the binned along strike averaged values for polar dip in navy blue and fracture probabilities in gray. (C) same example seismic line as (A), where colormap (transparency 50%) green colors

indicate negative curvature or concave down and blues indicate positive curvature or concave up. Overlain on the curvature colormap are the results for thinned fault likelihood. (D) is the along strike binned average mean curvature in green and fracture probabilities in gray. Note the most negative curvature makes the edge of the damage decay trend.

2.5 Conclusion & Implications

Using three-dimensional (3D) seismic attribute techniques, we find that the fault damage zone is observable and identifiable in seismic reflection datasets collected along the Palos Verdes Fault, offshore southern California. The seismic attribute computed from the data is representative of the damage zone and areas with elevated fault and fracture probability are consistent with areas of mapped faults both in this study and independent fault mapping efforts.

Due to the large acquisition footprints and large amount of data, we extend observations to greater distances and with more continuous sampling than is typically possible at the outcrop scale and with increased resolution over passive seismic methods. Additionally, the large datasets allow for a well-defined background and edge of the damage zone, which is ~ 2 km away from the central fault strand.

The method allows us to distinguish fracturing trends as a function of distance from the fault, lithology, and depth. We find that the level of fracturing decreases systematically with lateral distance from the fault. This trend is best fit by an exponential with a decay distance of between ~ 2000 and 4000 m, depending on lithology. We find that lithological variations and depth have the strongest control on damage decay and background fracturing.

The new window into damage as a function of lithology and depth provides a new insight into the trade-off between background damage and decay. Interestingly, these factors counterbalance each other resulting in a consistent damage width across the units. The data indicate that width can be a more stable feature of damage zones than might be anticipated from observed variations and trends in individual units. This new observation invites future modeling work exploring the role of rock strength in controlling damage zone width. Apparently, the relationship involves non-trivial feedback mechanisms that need to be fully explored.

Chapter 3 - Fault Damage Zone Insights from High-Resolution Seismic Imaging and the Relationship with Fluid Seeps Along the Palos Verdes Fault

3.1 Introduction

The distribution and intensity of fault damage zones provide valuable insights into the behavior and response of the Earth's crust to earthquakes. These fault damage zones are characterized by increased faulting, fracturing, and deformation around a fault's principal slip surface, and their presence has been documented in numerous field and geophysical studies (e.g., Chester and Logan, 1986; Caine et al., 1996; Choi et al., 2016; Scott et al., 2018; Rodriguez Padilla et al., 2022). Studies have revealed that fault damage zones are most pronounced and observable in the uppermost kilometers of the Earth's crust (Li et al., 1997; Thurber et al., 1997; Ben-Zion et al., 2003; Li et al., 2004; Cochran et al., 2009; Yang et al., 2011; Yang et al., 2014; Li et al., 2016a,b; Alaei and Torabi, 2017; Liao et al., 2019; Ma et al., 2019; Liao et al., 2020; Atterholt et al., 2021; Qui et al., 2021; White et al., 2021; Alongi et al., 2022). Although observed fault damage predominantly occurs at depths shallower than where earthquakes nucleate, these zones still undergo inelastic processes during coseismic rupture that alter the bulk rock properties. These changes significantly impact near-field seismic hazards, potentially amplifying ground motions during future earthquakes and affecting the distribution of seismic energy (Spudich and Olsen, 2001; Wu et al., 2009; Kurzon et al., 2014).

Furthermore, fault damage zones are essential to understanding fundamental earthquake physics problems. They can form a vital energy sink in the earthquake energy budget (Wong, 1982; Martel and Pollard, 1989; Chester et al., 2005; Abercrombie and Rice, 2005; Brodsky et al., 2005; Ke and McLaskey, 2022). Another key aspect is the impact of fault damage zone rheology on dynamic earthquake rupture. The properties of fault damage zones, such as their strength and frictional behavior, can influence the propagation and evolution of earthquake ruptures (Kame et al., 2003; Dunham et al., 2011). The heterogeneity of the fault damage zone can significantly affect the rupture behavior, the seismic cycle and seismic wave propagation (Ben-Zion and Sammis, 2010; Huang et al., 2014; Thakur et al., 2021). Furthermore, fault damage zones exhibit high permeability and play a crucial role in fluid flow around faults. Fluids stored within fault damage zones affect stress conditions and can potentially control nucleation and slip behavior (Hubbert and Rubey, 1959; Caine et al., 1996; Bense et al., 2013; Guo et al., 2021).

Numerous key questions remain unanswered despite the pervasiveness of fault damage zones and associated studies. For example, the relationship between the fault zone damage and current fault activity is unclear. It is possible that fault zone damage could be a valuable proxy for fault activity. This arises from the idea that repeated slip events on the fault cause the pattern of rock damage. If this notion were correct, then the characteristics of the damage zone could be used to infer the total offset with a thorough understanding of fault history, unit age, and slip rate. On the other hand, it is equally plausible that accumulated damage may reflect geological history rather

than present-day fault behavior. Resolving which of these scenarios is true is vital for interpreting the geologic record and assessing the potential use of fault zone damage as a meaningful indicator of fault activity with broader societal implications.

While the effects of bends along strike-slip faults on surface topography have been explored, their impact on inelastic deformation at depth remains largely unexplored. The impact of fault obliquity expressed as uplift and crustal shortening caused by restraining bends, as well as subsidence induced by releasing bends, have been widely investigated (Segall and Pollard, 1980; Aydin and Nur, 1982; Dooley and McClay, 1997; McClay and Bonora, 2001; Mann et al., 2007). Analog models have provided valuable insights, demonstrating that transpressional restraining and transtensional releasing bends generate more faults and wider zones of faulting and deformation than simple linear faults (Naylor et al., 1986). Importantly, transtensional settings tend to facilitate simpler fault structures with less folding (Dooley and Shreuers, 2012). Observationally, the connection between surficial fault geometry and the width or complexity of fault zones has been hinted at in surface rupture maps following large intraplate earthquakes (Aydin and Du, 1995; Teran et al., 2015) and recent studies using optical image correlation techniques have also indicated an increase in strain and surface cracking at fault bends (Scott et al., 2018; Milliner et al., 2021). However, it remains to be demonstrated how fault geometry might influence the distribution of faults and damage at greater depths.

Another critical issue involves understanding how the fault damage zone responds to accumulated fault offset. Existing research has demonstrated that the width of the fault damage zone tends to increase with greater displacement along the fault (Savage and Brodsky, 2011; Faulkner et al., 2011; Torabi and Berg, 2011). Additionally, conventional wisdom suggests that strike-slip fault zones should narrow and localize with depth in what is known as a flower structure (Harding, 1985; Sylvester, 1988). However, these models may not apply within a sedimentary basin setting, where sediment aggrades atop an active fault. In this scenario, the youngest sedimentary rock near the surface may have the narrowest damage zone because it has experienced the least offset. Whether a flower structure develops in an active depositional environment remains unclear.

In addition, the lateral extent of the fault damage zone is the subject of ongoing debate. Field studies commonly observe a fault damage zone that is 10s - 100s of meters wide (Chester and Logan, 1986; Shipton and Cowie, 2001; Berg and Skar, 2005; Choi et al., 2016). Conversely, geophysical indicators of fault damage find damage zones wider by an order of magnitude. These indicators include fault zone trapped waves (e.g., Li et al., 1997; Ben-Zion et al., 2003; Li et al., 2004; Yang et al., 2014; Li et al., 2016a,b), low-velocity zones(e.g., Thurber et al., 1997; Cochran et al., 2009; Yang et al., 2011; Atterholt et al., 2021; Qui et al., 2021; White et al., 2021), geodetic studies (e.g. Fialko et al., 2002; Fialko, 2004; Materna and Burgmann; 2016; Xu et al., 2023), and controlled source seismic reflection studies (Alaei and Torabi, 2017; Liao et al., 2019; Ma et al., 2019; Liao et al., 2020; Alongi et al., 2022).

Understanding the factors that control the disparity in results across methods is crucial for a unified depiction of the fault damage zone.

Lastly, the link between damage zones and hydrological features needs to be clarified, particularly in marine environments. While multiple studies have proposed that fluids generated at depth are structurally controlled and guided by faults to seep at the seafloor, direct in-situ data establishing a conclusive link between faults and seeps is lacking (Trehu et al., 1999; Kluesner et al., 2013; Prouty et al., 2020; Rudebusch et al., 2023;). Therefore, connecting measurements taken at the seafloor with the extent of damage at depth is essential for extrapolating insights from data-rich bathymetry and water column measurements to less abundant MCS seismic reflection data.

To address the knowledge gaps outlined above, the present study focuses on the offshore portion of Palos Verdes Fault in southern California. It utilizes newly collected 2D high-resolution multichannel seismic (MCS) and chirp sub-bottom profiles. The seismic survey design, acquisition equipment, and seismic processing techniques provide an opportunity to investigate fault damage at a mesoscale (~ 3 m horizontal and vertical resolution). This approach enables mapping the fault damage zone in the context of depth, activity, and hydrological seeps, providing critical insight into this complex system at an unprecedented scale.

In this study, it is shown that automated fault detection proves to be effective in accurately identifying faults within high-resolution MCS datasets. The fault

detections successfully localized around the active fault strand, even in the presence of a well-documented anastomosing fault network, demonstrating the reliability and applicability of the automated fault detection approach in capturing the actual fault location. The study establishes relationships between the fault damage zone, obliquity of the active fault trace, and displacement. Furthermore, the study employs fault damage and fluid seep proxies to explore the role of tectonic history in controlling fluid mobility around the fault zone.

3.2 Tectonic Setting and Data

3.2.1 The Palos Verdes Fault and Tectonic Context

The Palos Verdes Fault (PVF) spans approximately 100 km in length and exhibits a northwest-southeast strike (Fig. 3-1). It extends both onshore and offshore across southern California within the Inner Continental Borderland tectonic province, and it accommodates a portion of the dextral shear between the Pacific and North American Plates (Fig. 3-1). Slip rate studies indicate that the Palos Verdes Fault slips 1.1 - 5.9 mm/yr accounting for a significant percentage of total right lateral motion distributed amongst faults within the Continental Borderland (6 - 8 mm/yr) (Ward and Valensise, 1994; McNeilan et al., 1996; Brankman and Shaw, 2009; Sorlein et al., 2013; Brothers et al., 2015; Wolfe et al., 2022). Studies employing controlled source seismic reflection data have revealed that the fault is near vertical in the sedimentary rock above the basement, which occurs at a depth of approximately 2 km (Fisher et al., 2004; Brankman and Shaw, 2009; Sorlien et al., 2013; Brothers et al., 2015; Alongi et al., 2022).

Over the past 25 million years, the crust surrounding the Palos Verdes Fault has experienced various stress states and stages of faulting in response to the plate boundary's evolution. Before the Miocene (~ 25 Ma), the margin served as a convergent boundary between the Farallon and the North American Plates. The landward migration of the mid-ocean ridge led to the gradual introduction of progressively hotter and less dense oceanic crust entering the trench causing the Farallon slab dip to gradually decrease over time (Atwater, 1970; Bohannon and Geist, 1998). The increased subduction zone temperature caused by the proximity of the spreading center to the trench, led to the metamorphosis of the Cretaceous accretionary prism rock to the Catalina schist, which forms the basement rock in this region.

By the early Miocene (~ 23 Ma), the plate boundary underwent reorganization, transitioning into a transform system (Crouch and Suppe, 1993). Later in the Miocene, oblique extension, rifting, and normal faults led to the development of basins in the Borderlands, as evident by fault-ward thickening of Miocene units east of the fault in seismic reflection data (Fisher et al., 2004; Brankman and Shaw, 2009; Alongi et al., 2022).

During the early Pliocene (~6 Ma), the plate boundary stepped inland, forming the big bend, and the Borderlands faults underwent a transition from transtensional to transpressional systems (Yeats and Beall, 1991; Wright, 1991). This led to an uplift west of the Palos Verdes fault, juxtaposing older rock on the west and younger rock

east of the fault (Ward and Valensise, 1994) and is discussed in further detail in section 3.4.2

17) 3-1 Palos Verdes Fault Map with Track Lines

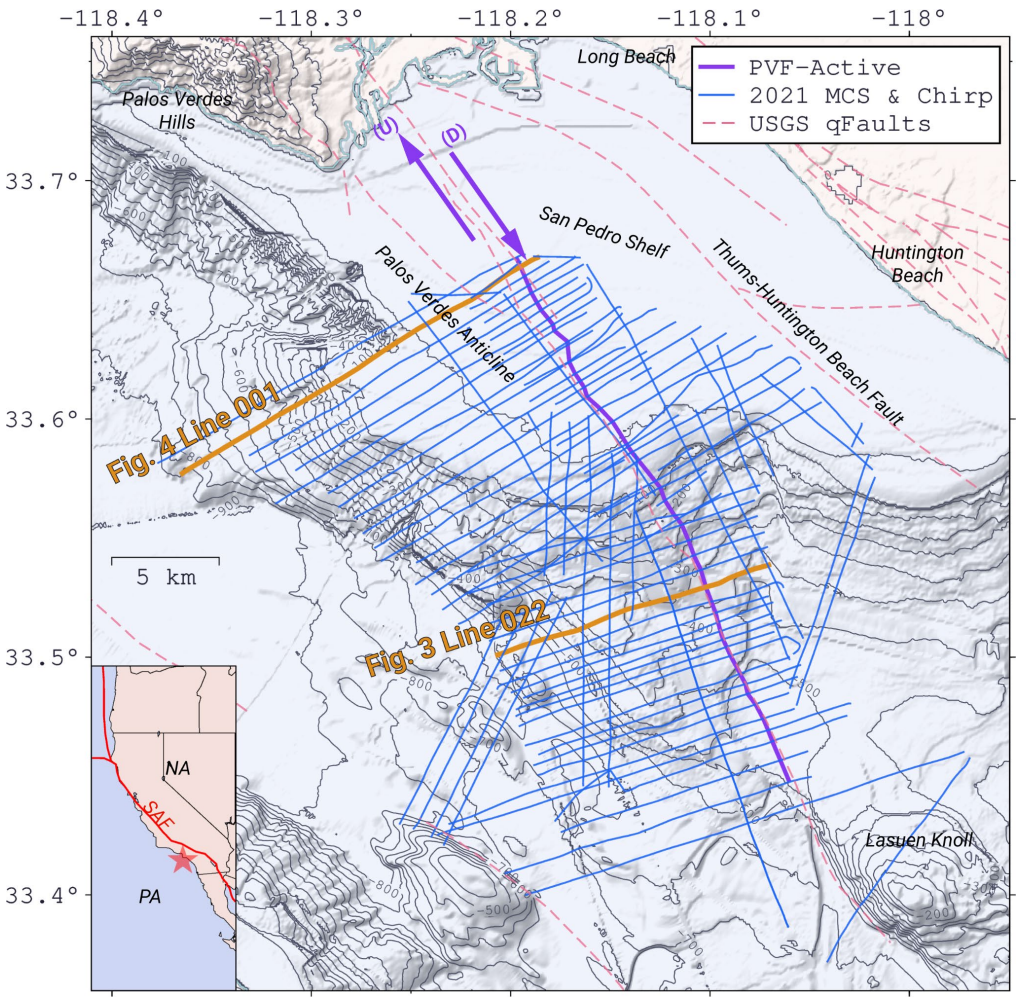

Fig. 3-1. Map of the Inner Continental Borderland and San Pedro Shelf in southern California. The inset map shows western North America with the red star indicating the study area offshore southern California; NA represents the North American Plate, PA represents the Pacific Plate, SAF represents the San Andreas Fault. Main map displays the location of mapped fault traces, with dashed pink lines representing the United States Geological Survey's Offshore Quaternary faults (Walton et al., 2020). The solid purple line depicts the mapped location of the active Palos Verdes Fault (PVF) strand identified in this study. The blue lines indicate the track line locations of coincident multichannel seismic (MCS) and sparker sub-bottom (Chirp) profiles used

in the study. Yellow lines represent the location of cross-sectional profiles shown in detail in other figures.

3.2.2 Data

Previous studies investigating the offshore portions of the Palos Verdes Fault have used various controlled source seismic reflection datasets to map the fault (Rigor et al., 2003; Walton et al., 2020; Alongi et al., 2022; Wolfe et al., 2022). However, data acquisition, survey design, and processing limitations have hindered the resolution of secondary faults that comprise the fault damage zone at shallow depths (less than 400 m below the seafloor). As a result, there is a lack of understanding regarding the extension of the fault damage zones to the seafloor, their relationship with bathymetric features, and their influence on seafloor fluid flow.

To address this knowledge gap and provide an improved fault zone analysis, we conducted a comprehensive study incorporating in-situ observations of the damage zone at depth up to the seafloor. The United States Geological Survey led a nine-day survey aboard the R/V Sproul to acquire high-resolution multichannel seismic (MCS, using a SIG 50-tip mini sparker sound source) and EdgeTech 2300 516 0.5 - 16 kHz (chirp) sub-bottom profiles. 97 coincident MCS and chirp track lines covering 975 line-km were acquired along the San Pedro shelf and slope (Fig. 3-1 & C-1).

The processed MCS data has a frequency range of approximately 100 - 300 Hz (Fig. C-2) and was recorded with ~ 120 m Geometrics GeoEel 40-channel streamer featuring group spacings of 3.125 meters and a sampling rate of 0.25 ms. The data

acquisition was conducted at a vessel speed of ~ 4 kts, with the streamer depth maintained at 2 m below the sea surface using Geospace Navigator birds.

For precise measurements of the shallow expression of the fault and its associated damage zone, most (81 out of 97) of the track lines were oriented perpendicular to the PVF fault strike, spaced at ~500 m intervals (Fig. 3-1 & C-1). This approach allowed us to accurately assess the fault and associated damage zone over 30 km. The newly collected high-resolution MCS data provides sub-bottom imagery with sufficient signal quality down to about 400 ms two-way travel time (TWTT) below the seafloor reflector.

3.3 Methods & Results

3.3.1 Multichannel Seismic Processing

The newly collected data underwent a rigorous workflow development phase using Shearwater Reveal software. The goal of the processing was to increase horizontal and vertical resolution, minimize the impact of source and receiver ghosts, and mitigate the impact of sea surface multiples. The seismic processing steps are outlined in Fig. 3-2, and further details can be found in Appendix 1-C.

The initial steps involved importing the raw SEGD files and calculating the source and receiver geometry using shipboard GPS navigation. The seismic data collected in shallow water were affected by water column multiples, which can overprint and limit the interpretation of reflection data at depth (Dondurur, 2018). To remove these multiples, we used a modern surface-related multiple elimination workflow that

mathematically predicts multiples by autoconvolution and then removes them through adaptive subtraction (Verschuur et al., 1992).

We estimated the source signature and performed pre-stack deconvolution to improve vertical resolution and reduce source ghosts and bubble-pulse (Sheriff & Geldart, 1995; Kluesner et al., 2019). Next, a critical step in high-resolution MCS data processing involves addressing along-streamer variations in receiver depths (Kluesner et al., 2019); without this step, destructive interference of high-frequency energy occurs during stacking and reduces the vertical resolution. This was addressed by applying pre-stack time shift static adjustments calculated from the cross-correlation of the windowed seafloor reflection on shot gathers. We also obtained 2D track line velocities using semblance-based velocity analysis workflows and then applied them to normal move-out correction on common mid-point (CMP) gathers. The resulting CMP gathers were stacked to increase signal-to-noise and further suppress seafloor multiples (Yilmaz, 2001).

In order to account for wave propagation effects and more accurately image the subsurface, and move reflected energy to its proper location, migration was done in the frequency domain using a phase shift migration method (Gazdag, 1978). We migrated the data at 1400 m/s, muting data above the seafloor and 1200 ms TWTT below the seafloor. Finally, we removed noise introduced in the deconvolution step by applying a structurally oriented denoising workflow to depths less than 400 ms TWTT below the seafloor (Hale, 2009).

18) 3-2 Processing Workflow and Fault Detection Schematic

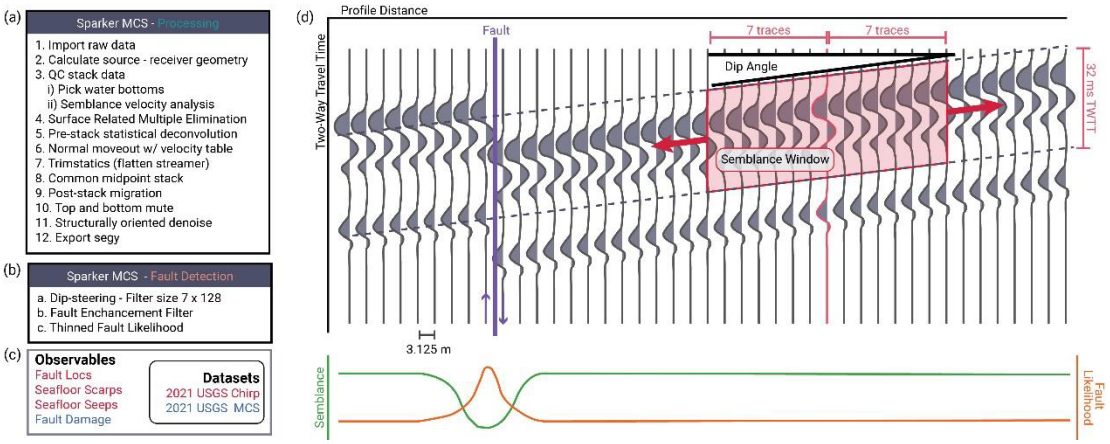

Fig. 3-2. Schematic workflow diagram illustrating the fault detection process. (a) Processing steps for the newly collected multichannel seismic data. (b) Explanation of the fault detection workflows performed on the processed data. (c) Linking the observables and the datasets used in the study, color coded accordingly. (d) Cartoon view of semblance and fault likelihood calculation on a dipping reflector with a faulting discontinuity (highlighted by the purple line, left side up). The dip-steered semblance window follows the dip of the reflector over a moving window of 7 lateral traces and 32 ms two-way travel time. The green curve schematically shows semblance value of the profile tracking the dashed gray lines. The orange curve depicts the equivalent fault likelihood value as a function of profile distance, and high fault likelihood at the discontinuity.

3.3.2 Mapping the Active Fault Strand

To accurately map the active strand of the Palos Verdes Fault and establish it as a reference for measuring fault damage, we utilize multiple datasets, including MCS and chirp sub-bottom profiles and high-resolution multibeam bathymetry. Our initial effort to map the fault involved strike perpendicular MCS profiles and interpreting various seismic faulting indicators such as reflector offsets, truncations, and amplitude reductions (see Fig. 3-3). This allowed us to map the fault from the seafloor to a depth of 300 ms two-way travel time (TWTT) below the seafloor,

providing insight into its subsurface geometry and properties. We observed that the fault is nearly vertical within this depth range.

19) 3-3 Comparison of MCS with Fault Detections

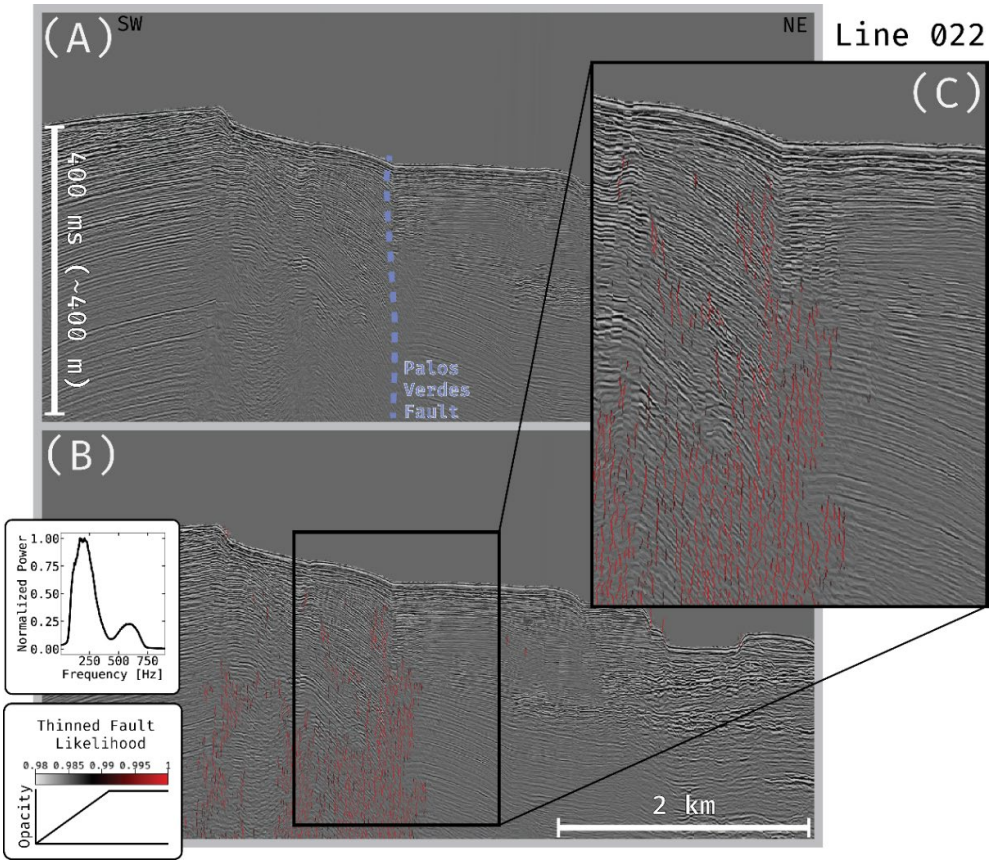

Fig. 3-3. A comparison of the preprocessed multichannel seismic (MCS) profile and with the thinned fault likelihood (TFL) attribute results for line 022, as indicated in Fig. 3-1. The view angle is from the southeast looking down the strike of the active strand of the Palos Verdes Fault (PVF) (shown in purple), which is identifiable by offset reflectors, folding, and near fault deformation features. The dimensions for the figures are indicated by the white bars. (a) Presents the processed dip-steered diffusion filtered results for comparison with transparent-to-red overlay of thresholded TFL in (b). The TFL attribute is truncated to highlight high fault likelihoods (TFL > 0.98) which is consistently used throughout the study and represent high fault likelihood or dissimilarity in seismic data. (c) Provides a zoomed-in view of the fault detections around the PVF active fault strand. Insets in the lower left display the frequency spectra of the MCS data used (top) and the color bar and transparency ramp for the TFL attribute (bottom).

In addition to MCS data, the chirp sub-bottom profiles played a crucial role in our study, particularly in examining the upper 25 ms TWTT of the fault zone and helping

to identify the fault strand with the most recent surface breaking rupture. These profiles not only revealed offset reflections but also unveiled seafloor offsets to provide additional evidence of recent fault offsets (see Fig. 3-4). The chirp profiles reveal a fault-related scarp, with the west side of the fault appearing elevated by as much as 3 meters (refer to Fig. 3-4 and Fig. C-3).

20) 3-4 Chirp sub-bottom Profile - Seeps & Scarp

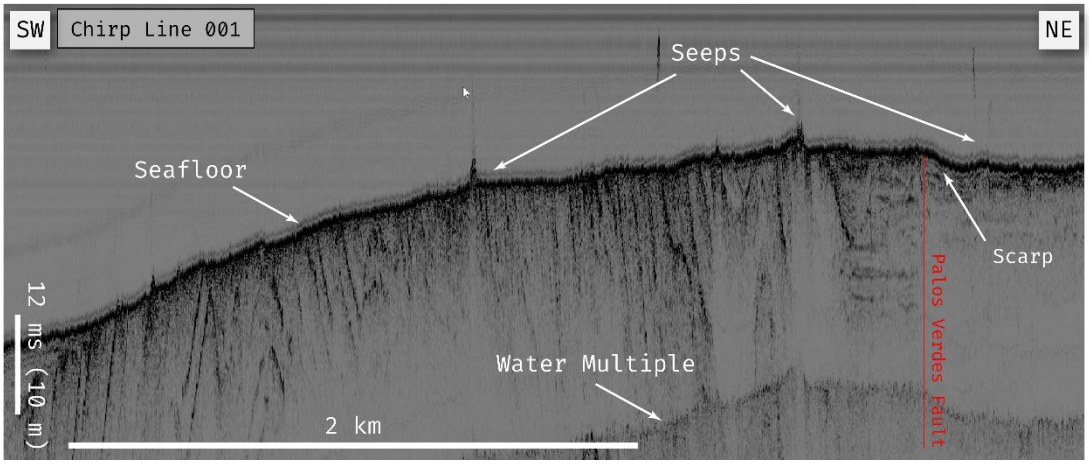

Fig. 3-4. Chirp sub-bottom profile example for line 001, as indicated in Fig. 3-1. The white bars indicate the length and depth with extreme vertical exaggeration of the profile to highlight the fault scarp and fluid seeps. The Palos Verdes fault is represented by the red vertical line, clearly marked by a sharp boundary between horizontally continuous Quaternary sediments to the northeast and deformed Miocene lithologies to the southwest. Along the shelf, all profiles crossing the fault exhibit a notable scarp at the fault location that helps determine activity. In this example, three actively flowing seafloor seeps are visible, identified by reflections in the water column created by fluid of different densities.

The scarp produced by fault offsets observed in the chirp sub-bottom profiles was also evident in the high-resolution bathymetry data. Once we had fully mapped the fault using the combined MCS and chirp profiles, we could trace the fault in finer detail by following geomorphic features on the seafloor. This meticulous mapping,

conducted at 50-meter intervals, provided us with the opportunity to test the potential impact of fault bends or variations in obliquity on the pattern of fault damage. In this context, we define the reference fault strike as 143°, which is the statistical mode of the fault azimuths (see Fig. C-5) along this segment. The term “obliquity”, denoted as α, is calculated as the difference between the reference strike minus the azimuth. Consequently, azimuths greater than the reference (oriented more north-south or clockwise rotation) have a negative obliquity, signifying right steps and corresponding to releasing or transtensional bends. Conversely, positive obliquities are counter-clockwise rotations and are more east-west of the reference, indicating left steps and compressional or transpressional bends.

21) 3-5 Obliquity of the Active Strand

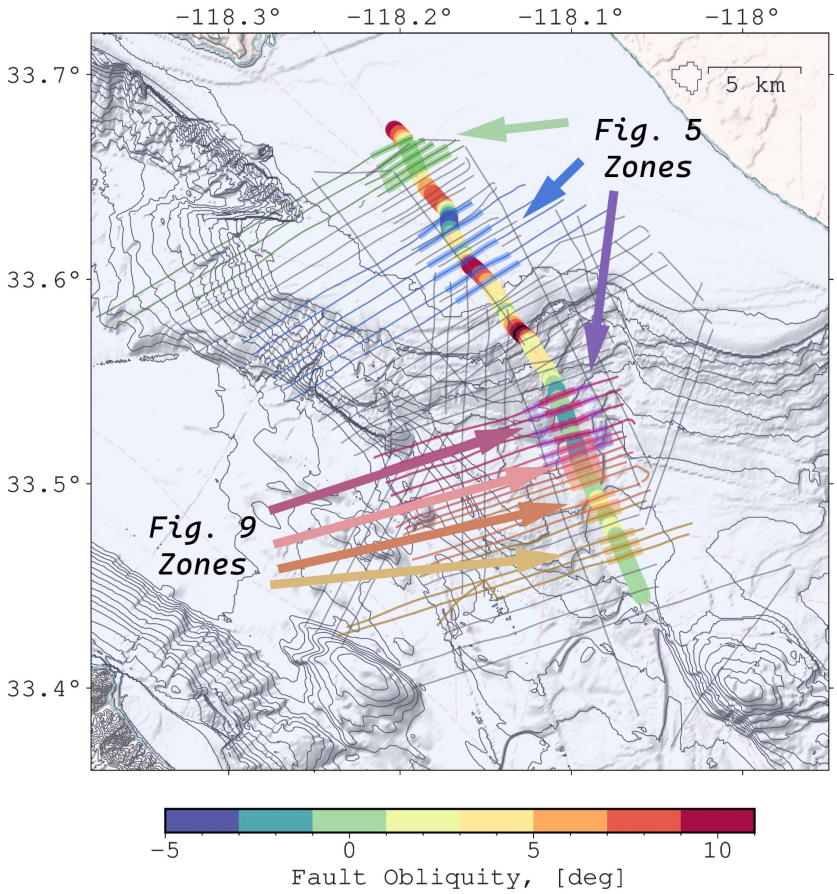

Fig. 3-5. Illustration of the variation in obliquity along the mapped Palos Verdes Fault. The colormap transitions from purple to red, representing the relative obliquity of the fault. Green hues indicate azimuths aligned with the reference strike (143 degrees), see 3.3.2. Cooler colors (blue and purple) indicate right bends and are transtensional, while warmer colors (orange and red) are left bends, indicating transpressional. The green, blue, and purple lines depict the location of profiles referenced in Fig. 3-6. The red, pink, orange, and yellow lines indicate the location of profiles utilized in Fig. 3-9.

3.3.3 Fault Detection

We present a data-driven approach for fault detection in 2-D high-resolution MCS lines, illustrated in Fig. 3-2. This approach utilizes the thinned fault likelihood attribute, calculated using structurally oriented semblance over a moving space-time

window (Hale, 2013). The fault likelihood attribute is derived from the semblance values, which measure multi-trace similarity to infer the lateral continuity of seismic reflectors (Marfurt et al., 1998). Using a filter window size of 7 traces and 32 ms two-way travel time, we calculate the fault likelihood as one minus the eighth power of semblance. The fault likelihood values range from 0 to 1, where 0 is low fault likelihood and 1 is high fault likelihood.

In this approach, high semblance values indicate lateral continuity of horizons or reflectors, resulting in low fault likelihood values. Conversely, low semblance values indicate reflector discontinuities, leading to high fault likelihood values. The resulting fault likelihood image is then subjected to thinning, where local maxima in fault likelihood are connected over apparent dips of 75-89 degrees, assuming a velocity of 2000 m/s, which represents an average seismic velocity of the sedimentary rock at these depths (seafloor – 400 ms TWTT beyond) as determined by geophysical sonic well logging (Alongi et al., 2022).

To enhance the lateral continuity of reflections and reduce noise before calculating thinned fault likelihood, we employ a dip-steered fault enhancement filter. This method applies different filters based on nearby reflector dips, aiming to reduce random noise while preserving the integrity of sharp discontinuities of the fault (Tingdahl and De Rooij, 2005; Chopra and Marfurt, 2008). Specifically, a dip-steered median filter is used in areas where reflectors have shallow to moderate dips, while a dip-steered diffusion filter is applied in regions with high dips. Fig. 3-3 showcases the

result of the fault enhancement filter and the thresholded thinned fault likelihood detections, which will be explored in greater detail.

3.3.4 Metric for Studying Fault Damage

This study investigates the spatial variation of faulting and fracturing in the damage zone related to the active fault strand. To achieve this, we analyze seismic lines that are approximately perpendicular to the fault's strike to quantify fault damage as a function of distance from the fault, spanning approximately 25 kilometers of the length of the Palos Verdes Fault. By selecting the highest faulting probabilities from the thinned fault likelihood attribute (TFL) with a threshold set at 0.98, we focus on fault detections that an interpreter would likely identify (Iacopini et al., 2016; Alcalde et al., 2017; Fig. 3-3). Additionally, we find that this threshold corresponds to an approximate inflection point in the histogram of the TFL data results (Fig. C-4). We conducted tests using other thresholds but found little difference in the results.

Our analysis focused on the depth range extending from the seafloor to 400 ms two-way travel time (TWTT) below. This interval was chosen because it offers a favorable signal-to-noise ratio in the data, as signal-to-noise degrades below 400 ms TWTT. The seafloor was mapped during the processing and was used as a constraint to define the depth and extent of our investigation. Each seismic trace is a 1D z-sampling of the TFL fault detection, consisting of 1600 samples that result from a 400 ms depth span and the 0.25 ms sampling rate of the MCS data. To qualify fault

damage, we counted the number of samples in the trace that exceeded 0.98 TFL. This metric, referred to as thresholded counts, is used throughout the study.

In order to examine how fault damage varies with distance from the fault, we measure the distance from each trace or sample to the precisely mapped location of the active fault. Given the variability in the results of fault damage (thresholded counts) with distance from the fault, we adopt a stacking approach to explore the average properties of the fault damage (Fig. 3-5). To create these stacked profiles, we needed to account for the non-uniform geometry of the track lines and resample the damage curves at uniform 3-meter distance increments. This resampling allows us to median stack the 2-D the curves, effectively collapsing the fault detection results along strike. These stacked results provide insights into the emergent characteristics of fault damage over the scale of the seismic survey. Differences in observed stacked damage curves are discussed in section 3.4.2.

22) 3-6 Distribution of Fault Detections - North, Central, & South

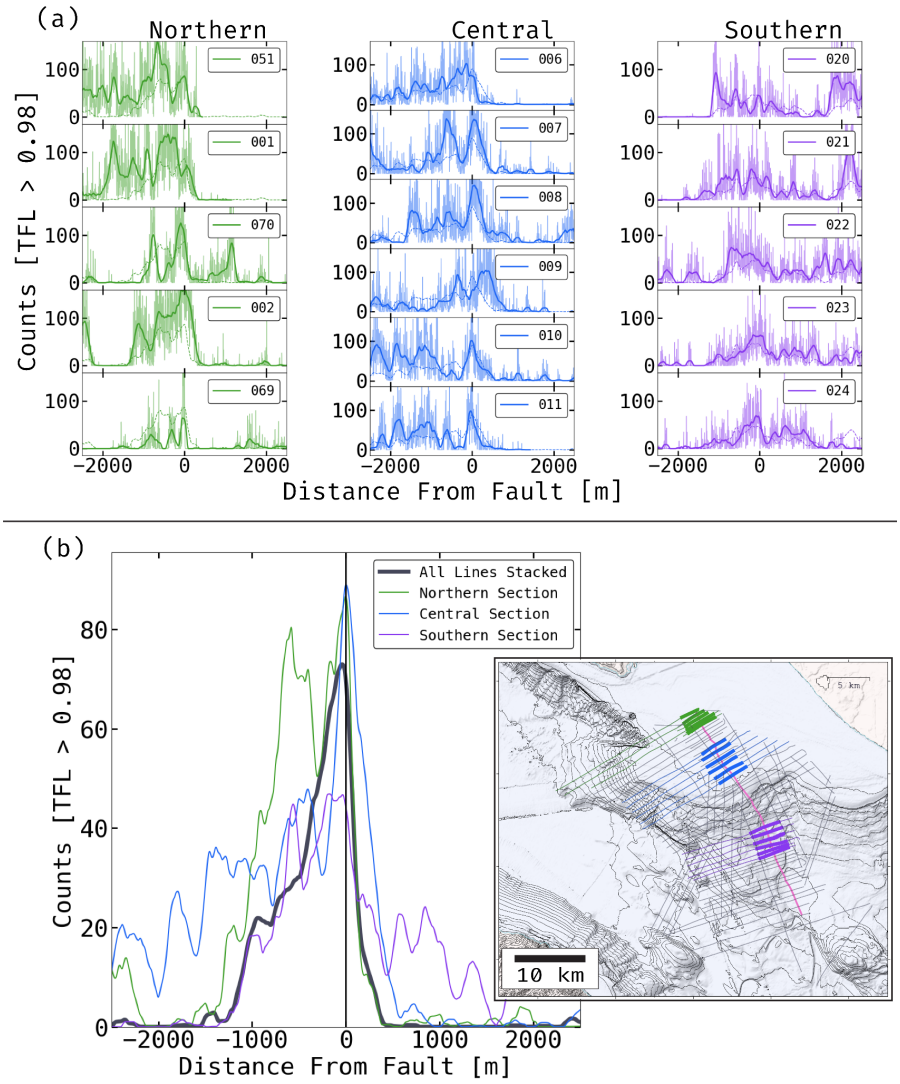

Fig. 3-6. Visualization of the distribution of high probability thinned fault likelihood (TFL) detections variations with distance from the active fault strand, calculated from the multichannel seismic data over the depth range from the seafloor to 400 ms two-way travel time below the seafloor. (a) illustrates individual line curves for different fault sections, as indicated in the inset map in (b). In (a), the lines are arranged in order from north to south for their respective sections, with the line number provided in the upper right corner; see Fig. A-1 for a detailed track line map. The light-weight lines represent the number of samples in the trace (3 m sampling) that exceeded 0.98 TFL. The heavy-colored lines indicate smoothed data using a moving mean with a tapered cosine window (200 m width). (b) The median stack of each section as shown in (a). The heavy-weight dark line represents the median stack of all fault

perpendicular lines. It is important to note the variability in the fault zone in individual profiles compared with the averaged values.

3.3.5 Seafloor Fluid Seeps & Fault Damage

The conventional depiction of fault zone structure often portrays the tabular area around the principal slipping surface as more permeable than the surrounding host rock. This permeability contrast has been recognized as a significant factor in controlling fluid flow around faults (Caine et al., 1996; Guo et al., 2021). This study shows clear evidence of near-fault active fluid flow through observations of acoustic flares detected in the water column on chirp sub-bottom profiles (e.g., Fig. 3-4). These disturbances result from impedance differences caused by density variations between gaseous seeping fluid and ambient seawater (Suess, 2020) and were mapped on all chirp sub-bottom profiles. It is important to emphasize that the observed seeps represent a snapshot in time, portraying their activity during the survey. Additionally, the seeps are identified in 2D profiles, and the actual distribution of seeps is likely much more extensive than what the results depict. We qualitatively compare the seep locations with the fault detection data, and we find that seeps tend to concentrate in areas of high likelihood of faulting, particularly in proximity to the mapped active fault; further details will be discussed in Section 3.4.4.

3.4 Discussion

3.4.1 Damage Highlights Active Fault Strand

Our analysis demonstrates that stacking thresholded fault detections, derived from thinned fault likelihood (TFL), closely aligns with the active fault strand of the Palos

Verdes Fault (Fig. 3-6b). There is a notable alignment between the peak in the stacked TFL results and the location of the meticulously mapped active strand (section 3.3.2), agreeing to within approximately 50 meters. This observation is intriguing because the peak in fault detections occurs at the location of the active strand even in the presence of the well documented multi-stranded Palos Verdes Fault (Brankman and Shaw, 2009; Sorlien et al., 2013; Walton et al., 2020; Alongi et al., 2022) (Fig. 3-6).

We interpret this correspondence between the peak in fault detections and the location of the independently mapped fault as a two-way relationship. It suggests that peaks in fault detection may not only be indicative of fault activity but also useful in aiding fault mapping efforts. This finding has broad implications for accurate identification of the active fault strand, which is crucial for seismic hazard assessment and risk mitigation.

3.4.2 Average Fault Damage Pattern Robustness

The analysis of fault detection using high-resolution MCS data reveals a remarkable degree of variability in damage results along strike, particularly on closely spaced lines. However, this complexity diminishes as we stack an increasing number of fault detection curves (Fig. 3-6). Each seismic profile and fault damage measurement represents an in-situ cross-section through the shallow subsurface. These high-resolution 2D MCS profiles share many characteristics with outcrops of faults in the field, albeit at 3-meter resolution, providing a detailed view of the

structures surrounding the primary slip surface. However, when these lines are stacked or averaged the fault detections along strike, a smoothed pattern of fault damage emerges, as depicted in Fig. 3-6b. These findings imply that the complexity in geologic observations of fault zones and the smoother characterizations of the damage zone often found in geophysical measurements of the damage zone may be reconciled. Stacking the damage profiles is like many geophysical measurements integrating damage information over a distance (i.e., tomography, fault zone trapped waves, geodesy).

In other words, the fault zone exhibits significant variability in cross-section. However, it becomes systematic in its behavior with additional realizations or measures of the fault zone over the length of the fault. This has important implications for interpreting and incorporating fault damage information into models, seismic hazard assessments, and fault mechanics studies.

3.4.3 Interpreting Fault Damage within Geologic Context

There is a clear asymmetry to the stacked fault damage zone trends (Fig. 3-6b). There is a preference for damage to extend further to the west of the fault, while fault damage appears to be more localized east of the fault. We attribute this damage asymmetry to the well-documented tectonic folding and uplift occurring west of the fault (Ward and Valensise, 1994, Brankman and Shaw, 2009; Sorlien et al., 2013). This anticlinal uplift has resulted in older, more deformed/faulted rock being juxtaposed against younger, less deformed rock on opposite sides of the fault.

Consequently, the increased fault damage on the western side of the fault can be attributed to the presence of more deformed and fractured older rocks. These highly fractured rocks provide fluid pathways, which are further explored in section 3.4.6, and may explain the pattern of seafloor seeps.

The northern section of selected profiles, represented by the green curve in Fig. 3-6b, features two distinct peaks in damage detections that can be attributed to the splay in the fault zone here. One peak of fault damage aligns with the fault itself, while the other is located approximately 800 meters to the west. This observation is consistent with the trace locations of the fault provided by the United States Geological Survey's Offshore Quaternary Faults database (Walton et al., 2020) which includes a bifurcation of the fault as it extends northward (Fig. 3-1). The eastern strand is continuous and has been confirmed to extend into Santa Monica Bay, where the western strand is not apparent beyond the Palos Verdes Peninsula (Wolfe et al., 2022). Building upon our earlier suggestion in section 3.4.1 that fault activity is linked to fault detections, we suggest that both strands are likely active. The amplitude of the peak delineating the eastern strand is greater than for the western peak, which makes sense when considering that the eastern strand is longer and has experienced more cumulative slip and thus more damage.

The central section of the study area, indicated by the blue curve in Fig. 3-6b, has the highest peak in fault detections. The damage extends further east and west compared to the all-stack average trend and the north and south sections.

Qualitatively, this section of the fault is the most damaged in terms of fault detections and is evident in seismic profiles themselves. Mapping the active strand in this area was particularly challenging due to the presence of multiple fault strands in the MCS profiles. We suspect that the increased damage observed here is likely due to the left transpressional bend in the fault (Fig. 3-1, 3-5, & C-5). Previous studies have shown that fault bends tend to increase the number of fault strands required to accommodate the obliquity and thus leading to increased damage and width relative to straighter sections of the fault (Kluesner and Brothers, 2016; Alaei and Torabi, 2017), and this will be explored in detail in the next section.

The southern section of the study area, highlighted by the purple curve in Fig. 3-6, exhibits the least amount of damage compared to the north and central sections. This section of the fault is characterized by its relatively straight and simple nature, with minimal influence from other fault strands or splays (Fig. 3-5). Additionally, the proximity to the end of the fault at Lasuen Knoll (Fig. 3-1) may contribute to the reduced fault damage. Further details regarding this aspect will be discussed in more depth in section (3.4.5).

3.4.4 Fault Obliquity Impacts the Fault Damage Zone

Our objective is to understand how local changes in fault strike or fault obliquity manifest as fault damage. We make use of the variations in fault strike that vary by up to 15 degrees (Fig. 3-5, 3-7), that are observable through detailed mapping efforts (see section 3.3.2). Here we explore how these bends in the fault or changes in strike

create zones of transpression and transtension (Sanderson and Marchini, 1984; Sylvester, 1988; Cunningham and Mann, 2007) that may manifest as additional fault strands and deformation patterns.

To assess the impact of obliquity of fault damage, we calculate the deviation from the reference azimuth (143°) which we define based on the statistical mode derived from the distribution of azimuths that constitute a majority of the fault azimuth (Fig. C-5). This azimuth matches the strike of the fault in the southern portion of the survey area where there is a decrease in near fault folding and vertical offset across the fault which provides further clues that the reference azimuth is the preferred orientation of the fault. Obliquity is calculated as the reference azimuth minus the azimuth and defined at 50 m intervals along the fault trace and represents the deviation from the preferred orientation. Fig. 3-7 displays the results of the obliquity calculation as a function of distance along strike.

23) 3-7 Fault Detections and Obliquity vs. Along Strike Distance

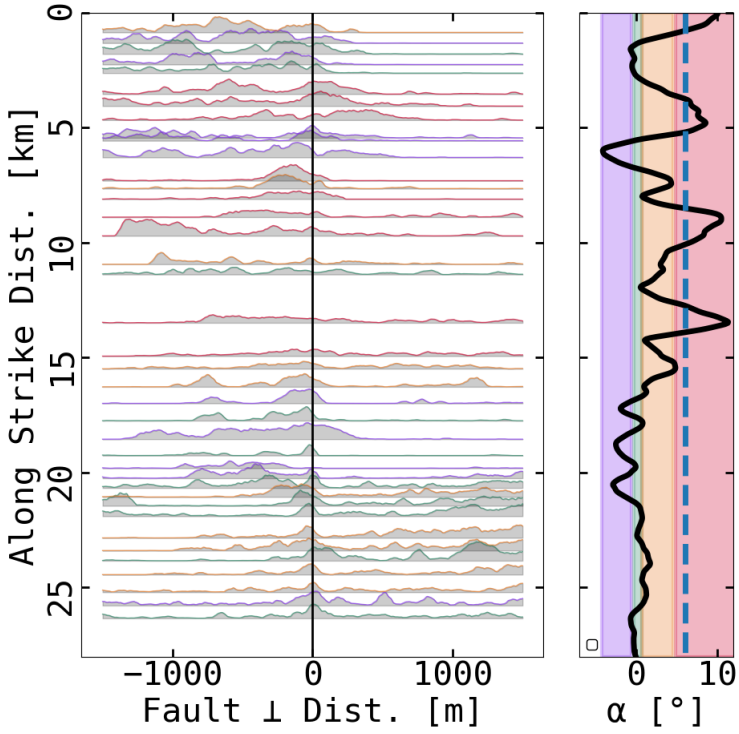

Fig. 3-7. Illustrating the variability in the fault detections and fault obliquity with distance along strike. (Left) the curves depict the counts of thresholded Thinned Fault Likelihood calculation [TFL > 0.98] as a function of distance from the fault. Gray shading under each fault detection curve aids in visualization. Positive fault distances are locations east of the fault and the along strike distance is measured with respect to the north-western edge of the survey (Fig. 3-5). (Right) illustrates obliquity, α in degrees that fluctuates along the fault's length. Positive α values are considered compressional regions, while negative α denotes extensional conditions. The obliquity bins utilized for stacking the data in Fig. 3-8 are highlighted in purple, green, orange, and red accordingly, with curves contributing to the obliquity bin maintaining consistency. The dashed blue line represents the plate motion direction (mean = 137°) from terrestrial Global Navigation Satellite Systems in the Palos Verdes Hills and Long Beach area.

Next, we categorize the 40-fault perpendicular fault detection profiles into four equal sized bins based on obliquity and stack the curves following the method outlined in 3.3.4. In order for a fair comparison between the obliquity stacks we

require an equal number of observations in each. This is because increasing the number of curves in the stack tends to smooth the results (as discussed in 3.4.2) and could bias qualitative comparison. The stacked results are presented in Fig. 3-8.

We interpret the stacked obliquity curves presented in Fig. 3-8 as being influenced by the degree of obliquity. The green curve (Fig 3-8b), representing a very narrow obliquity range (-0.4° to 0.7°), essentially mirrors the reference azimuth and features the most localized and narrow fault damage zone. Many of the individual curves contributing to stacked results are located in the southern region of the survey area, where we observe less near-fault deformation and fewer fault strands. We interpret this obliquity range to be the ideal fault strike because the fault zone is narrow, and it is also the most common fault azimuth. Based on this assumption and interpretation, the qualitatively wider and more distributed purple curve, and orange curves (Fig. 3-8a, c) may be caused by the increased relative obliquity. We find that when obliquity increases further, beyond 4.8° as in Fig 3-8d, we observe an even broader distribution of damage and a less clearly identifiable 'main strand' or peak in damage. The correlation between obliquity and the lateral extent of deformation is consistent with analog experiments (Dooley and Schreuers, 2012) as well as theoretical considerations (Sanderson and Marchini, 1984; Fossen and Tikoff, 1993). We suspect that the increase in damage west of the fault in the divergent curve (Fig. 3-8a) may be due to the superposition basin-bounding normal faults in the pull-apart basin that increase in separation (Fig 3-7 along strike distances between 15 – 20 km).

24) 3-8 Obliquity Fault Detection Stacks

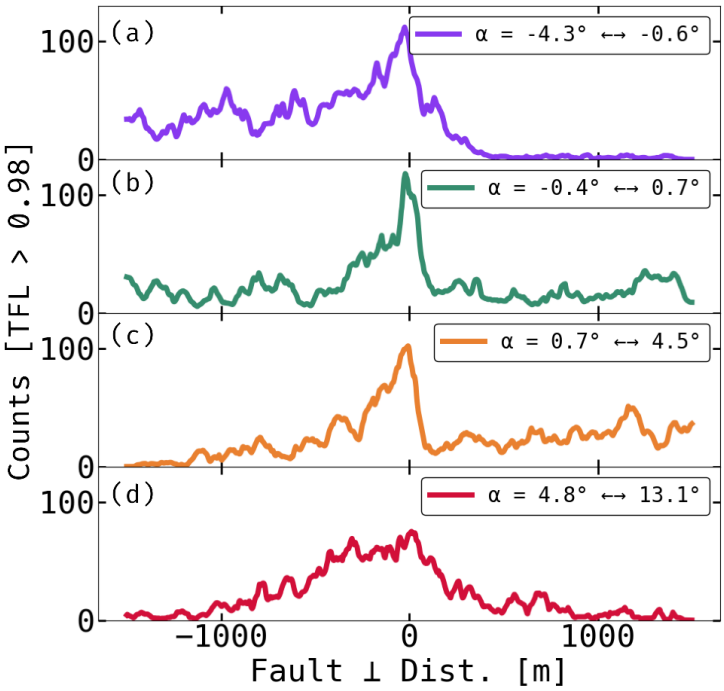

Fig. 3-8. Fault damage data are stacked according to the obliquity of the fault. The different colors represent the obliquity (α) of the fault with respect to the reference, see text in section 3.4.4. (a) The purple curve represents an extensional or divergent fault bend. (b) The green curve is interpreted to be well aligned with the preferred orientation of the fault. (c) The yellow curve represents a compressional or convergent fault bend. (d)The red curve represents the stack of the highest convergent and compressional fault bends that are greater than 4.8 degrees of obliquity.

3.4.5 How Cumulative Fault Displacement Relates to the Fault Damage Zone

In order to investigate the influence of varying cumulative displacement along the PVF on fault damage, we concentrate on the southern section of the surveyed area. This choice allows us to potentially isolate the impact of displacement from obliquity factors discussed earlier. The selected fault segment lies to the south of the shelf break and is relatively straight and features minimal obliquity deviations (Fig. 3-5).

To facilitate our investigation, we consider two key assumptions. First, we exploit the fundamental principle that cumulative slip along the fault profile must ultimately reach zero at the fault's tip (Segall, 2010). Second, we assume that the slip direction has remained constant. This assumption is based on our focus on depth ranges extending from the seafloor to 400 ms two-way travel time below, which corresponds to an approximate depth of 400 meters, assuming 2000 m/s velocity. The sedimentary rock formations we analyze date back to Mid-Pliocene, approximately 3 million years ago, which is well after the documented reorganization of the plate boundary (as detailed in section 3.2.1).

Our methodology relies on the application of linear elastic principles and leverages the elliptical relation between displacement and the distance from the fault tip (Tada et al., 1973; Segall and Pollard, 1987; Burgmann et al., 1994). This relationship is mathematically expressed as:

$$(3) \quad u = 2\,\Delta\sigma\,(\frac{(1-\nu)}{G})\,(a^2 - x^2)^{1/2}$$

where u is the calculated displacement, ν denotes Poisson's ratio, G is the shear modulus, a represents the half length of the fault, x is the distance from the center of the fault, and $\Delta\sigma$ is the scalar stress drop. Our calculation assumes an estimated displacement of 5 km on the mid-shelf (Brankman and Shaw, 2009), while the reference point for zero displacement is anchored at a location devoid of observable fault offsets, as supported by legacy seismic line WSD81-712 (Triezenberg et al., 2016), positioned approximately 50 kilometers along the southwest projection of the

fault (depicted in Fig. 3-9). Subsequently, we employ the relationship outlined in equation (3) to estimate the displacement for four subsections within the southern region, as illustrated in Fig. 3-9. Our aim is to explore how variations in displacement may correlate with changes in the associated damage zone.

25) 3-9 Damage Stacks - Southern Section

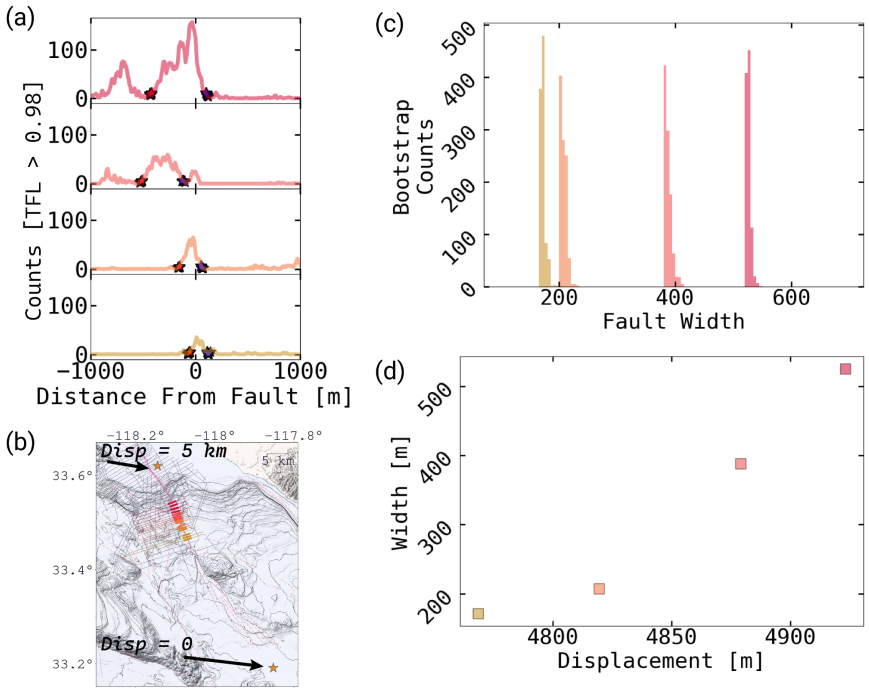

Fig. 3-9. Displaying the decrease in fault damage towards the south. Panel (a) visualizes the variation of stacked and thresholded thinned fault likelihood (TFL > 0.98) with distance east of the active strand of the fault, similar to the plots shown in Fig. 3-6. The stars on the curve represent the edges of the damage zone, defined as where the value equals 5 % of the peak damage with the red and blue stars corresponding to the western and eastern edges, respectively. The locations of each stack subsection are depicted in (b) where colors remain consistent in all subplots. The curves and edges are obtained through 1000 bootstrap iterations, and the results for the measured edge distances and integrated quantities are presented in (c). (d) Showing fault zone width as a function of estimated displacement, details on the displacement estimation are presented in the text, section 3.4.5.

In order to compare estimated displacement along the fault to the damage zone width we seek to determine the lateral limits or width of the damage zone without relying on a functional form. To achieve this, we identify the left and right edges of the damage curve as the location on each side of the peak where the value equals 5% of the maximum value, indicated as stars in Fig. 3-9a. To assess the reliability of our edge determination, we employ bootstrap resampling with replacement of the data, following the approach outlined by Efron and Tibshirani (1994). Through 1000 bootstrap iterations for the edges calculation and find that this metric provides rather stable results (Fig. 3-9c).

The analysis indicates that damage width decreases monotonically to the south-east covering approximately 13 kilometers of fault length. This decline in damage width can be attributed to the known tendency for cumulative fault slip to decrease toward the fault's ends. In this context, the decrease in damage width aligns with scaling relationships that link damage width to cumulative slip (Savage and Brodsky, 2011; Alaei and Torabi, 2017). The results presented here are consistent with compilation studies of damage zone width and displacement (Fig. 3-10, blue points;

Savage and Brodsky, 2011; Alongi et al., 2022). However, it is important to note a deviation from expectation. The pronounced increase in the width of the damage zone with displacement is significantly greater than what one would anticipate solely on the scaling relationship. This leads us to conclude that the overall width extent is governed by fault displacement, however the rapid increase in width to the north may be influenced by the decreasing obliquity observed in Fig. 3-5.

It is worth highlighting that the choice of displacement scaling relationship affects the calculated displacements experienced by each subsection. Some studies favor a linear slip relationship with fault length (Cowie and Scholz; 1992 a, b; Dawers et al., 1995; Cartwright et al., 1995; Manighetti et al., 2001; 2003; 2005; Kim and Sanderson, 2005). If we were to adopt a linear scaling of fault length with displacement, instead of the elliptical relationship used, it would reduce the calculated slip by a factor of 2 (Fig. C-6). Our results, regardless of the slip-scaling relationship used, exhibit a more dramatic increase in the width of the damage zone with displacement than what is observed in the compilation trend (Fig. 3-10).

26) 3-10 Damage Zone vs Displacement - Comparative

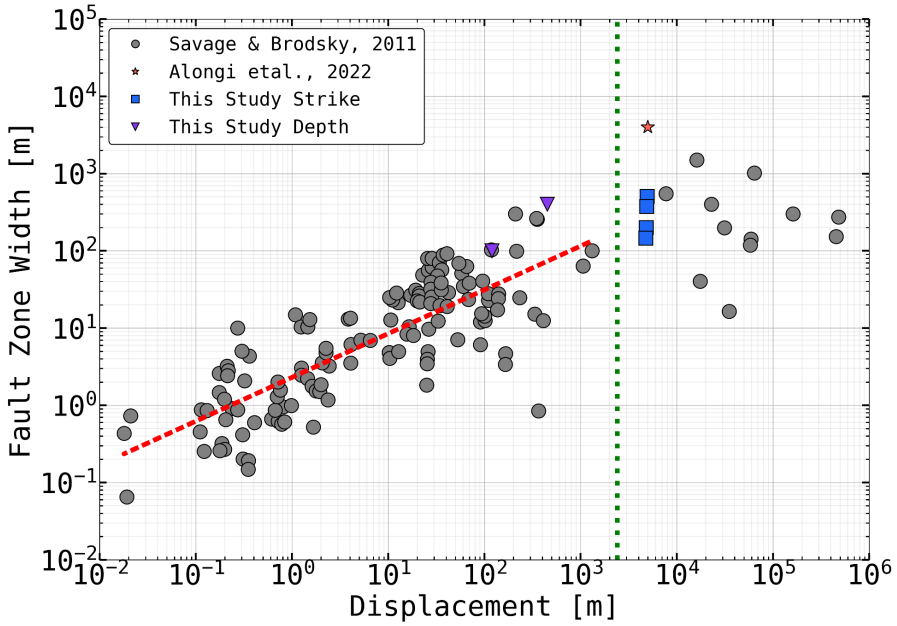

Fig. 3-10. Comparison of the damage zone width versus displacement, along with previous compilation study results. The blue squares indicate widths were estimated from bootstrapping results that were presented in Fig. 3-9. The purple inverted triangles represent damage width estimates shown in Fig. C-7 with displacement estimated using the slip-rate and age, see text.

To further investigate the relationship between fault displacement and fault damage, we examine two different depth intervals. The assumption is made that fault slip rate remains constant through time, allowing us to calculate the displacement experienced by rock adjacent to the fault based on its age. To determine the ages, we use documented sediment ages from Ponti et al. (2007) and extend horizon mapping from Ehman et al., (2014) onto the MCS lines in this study. This information helps establish the approximate age ranges of two depth intervals:

(1) from the seafloor to 100 ms two-way travel time (TWTT). This interval approximately corresponds to the Dominguez and Mesa sequences, dating to 15,000 and 30,000 to 80,000 years respectively.

(2) 100 to 200 ms TWTT below the seafloor. This deeper interval encompasses the Pacific Harbor and Bent Springs sequences, spanning age estimates from 110,000 to 300,000 years.

These age estimates were determined using correlative Marine Isotope Stages with Oxygen 18 isotopes (Grossman & Joachimski, 2020) or more precisely with optically stimulated luminescence dating techniques (Rhodes, 2011).

We calculate the fault offset for these two units given their approximate age and an average slip rate of 3 mm/yr (which is the rounded median of published slip rates that range from 1.8 - 4 mm/yr (Ward and Valensise, 1994; McNeilan et al., 1996; Brankman and Shaw, 2009; Sorlein et al., 2013; Brothers et al., 2015; Wolfe et al., 2022). The damage zone width is determined by measuring twice the distance from the point where the value equals 5% of the peak value shown in Fig. C-7, and the resulting two points are shown as purple triangles on Fig. 3-10.

The data presented here suggests that the width of the damage zone does not significantly narrow with depth. This observation deviates from the typical model of strike-slip faults that exhibit flower structures or a localization of the fault zone with increased depth as described by Sylvester (1988). However, it is important to note that this observation may be unique to syndepositional faults characterized by offsets

that increase with depth. Nonetheless, our findings highlight that differential offset, both along strike and depth, may influence the lateral extent and intensity of fault damage.

3.4.6 Fault Damage Controls Fluid-Flow

Our analysis reveals a clear correlation between the location of active fluid seeps and the thinned fault likelihood (TFL) attribute, as shown in the map in Fig. 8. This correlation suggests that the fault damage, which provides enhanced permeability (Caine et al., 1996; Faulkner et al., 2010; Bense et al., 2013), is facilitating the escape of fluids from the seafloor that we observe in the chirp sub-bottom profiles. Interestingly, we find that seeps are predominantly observable to the west of the fault and are primarily confined to the shelf area. This indicates that fault alone is not the sole control on seafloor seepage. The absence of seeps to the east of the fault as well as on the slope suggest that a young sediment cap may be preventing the free escape of fluid from the seafloor in these areas. We suspect that the series of seeps observed at the eastern edge of the study area are associated with the damage zone of the Thums-Huntington Beach fault.

27) 3-11 Fault Detections and Seafloor Seeps

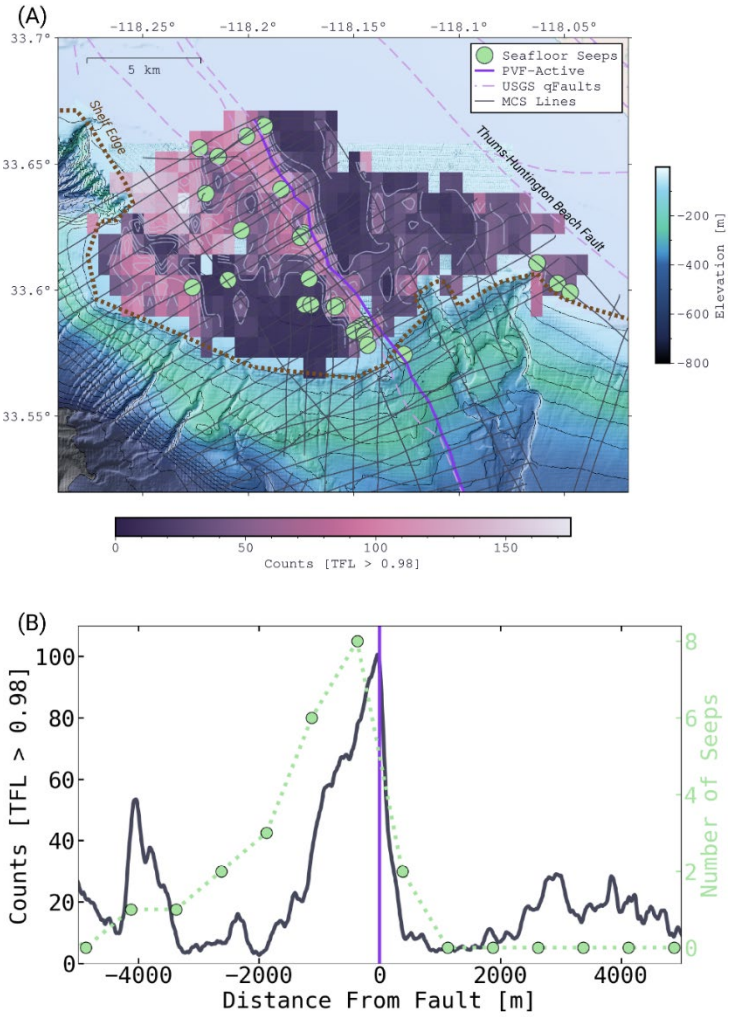

Fig. 3-11. Comparison of the thresholded thinned fault likelihood attribute (TFL) with the locations of the manually mapped seafloor seeps depicted by light green circles. (a) The TFL color palette ranges from purple at low fault detection levels, to white representing highly faulted areas. Additionally, a contour of the TFL detections is included to assist the reader. Fault detection data is displayed for shelf regions, and the shelf break is represented by a dashed brown line. (b) Comparison of binned number of seeps and thresholded TFL detections as a function of lateral distance east of the fault.

Overall, our findings highlight the complex interplay between faulting, permeability, and fluid flow dynamics in the study area, schematically shown in Fig.

3-12. The correlation between active fluid seeps and the TFL attribute suggests that fault damage acts as a preferential pathway for fluid migration and escape. Understanding the factors controlling fluid seepage in this region is crucial for comprehending the broader feedback between active tectonics and fluids.

28) 3-12 Fluid System Schematic

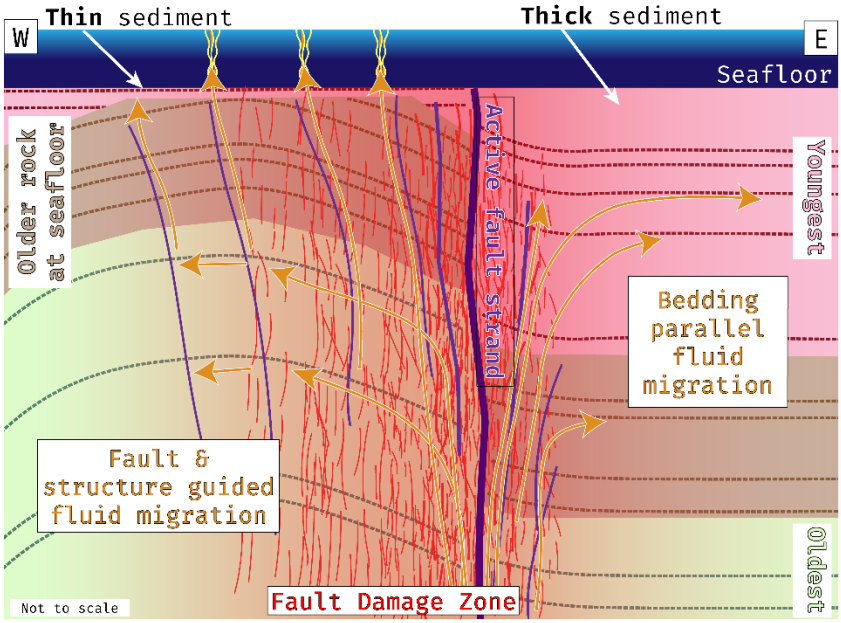

Fig. 3-12. Schematic cross-section cartoon representing the fluid system in section 3.4.5 of the text. Fluids generated at depth migrate toward the seafloor through the high permeability fault damage zone, represented by red subvertical lines. The fault damage, combined with the tectonic history of the Palos Verdes Fault region, influences the spatial distribution of fluids released at the seafloor. Long-term uplift west of the fault brings older, more damaged rock closer to the seafloor, preventing the accumulation of Quaternary sediments; this facilitates the uninhibited release of fluids. Conversely, to the east of the fault where the damage is low and a thick sediment cap exists, fluids tend to be trapped within formation beds.

3.5 Conclusion

In conclusion, our study comprehensively investigates fault damage zones, fluid seeps, and their relation to the active strand of the Palos Verdes Fault. Using high-

resolution multichannel seismic (MCS) and chirp sub-bottom profiles, we have identified the active fault strand and characterized the damage distribution along the broader fault zone. We observe the highest intensity of damage occurring at the location of the active strand. Our findings demonstrate the effectiveness of the automated fault detection method in accurately identifying the active fault strand within a complex fault network, thereby offering a valuable tool for future studies in fault analysis and seismic hazard assessment.

We note that fault zones are highly variable in signature and lateral extent in MCS cross-section profiles; however, a consistent pattern emerges when fault detections are averaged along strike. This suggests that the smoothness of fault damage zone studies observed in other geophysical studies is likely a low-passed averaged depiction of the fault zone, potentially obscuring additional complexities observed in field studies that are averaged out.

Furthermore, we establish a correlation between fault damage zone width and displacement along strike and depth, underscoring the influence of cumulative slip on the extent of the damage zone. Additionally, we uncover a connection between the degree of damage localization and the obliquity of the fault. Our findings indicate that increasing fault obliquity, whether in restraining or releasing bends, amplifies the distributed nature of the fault damage zone. This insight into fault obliquity explains the variation in fault damage observed along the length of the fault. While overall

width and distribution of damage may be controlled by displacement, fault obliquity also plays an important role.

By combining the fault damage analysis with observations of fluid seepage patterns, we uncover the role of tectonic history and sedimentation in controlling fluid mobility around the fault. The observed correlation between fault damage and fluid seeps provides insight into how faults govern subsurface fluid flow and expulsions at the seafloor. The absence of fluid seeps in areas with thick quaternary sediment suggests that the fluids are trapped in these layers without any clear pathways (faults/fractures) to the seafloor.

Appendices

Appendix A – Supplemental Information for Chapter 1

29) A-1 Event Depth Distribution

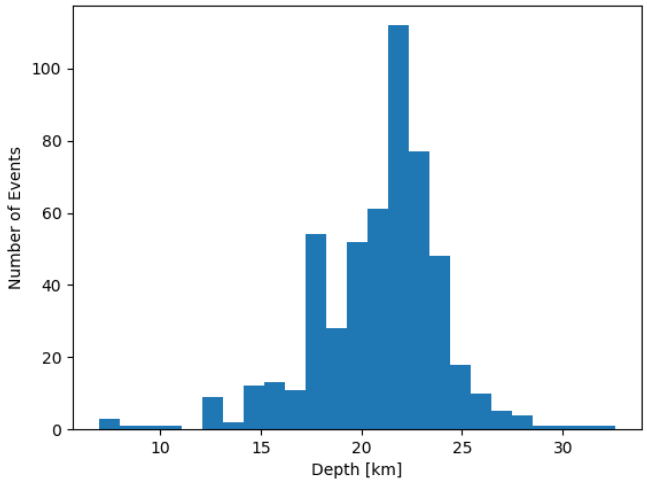

Fig. A-1. Histogram showing depth distribution for events that locate within 5 km of McCrory 2012 plate interface model. The mean of this distribution is 20.8 +/- 3.2 km.

30) A-2 Map of Events within 5 km of Plate Interface

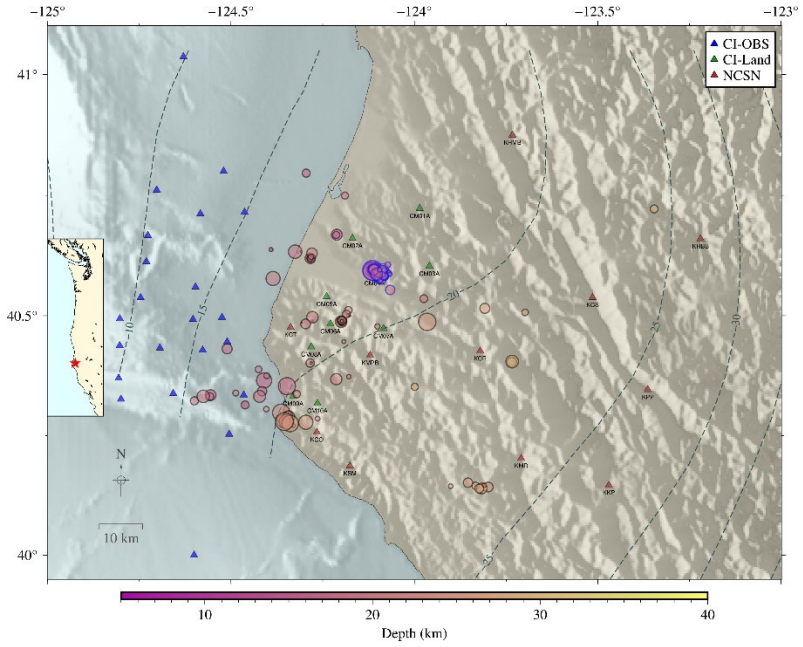

Fig. A-2. Map showing all 200 events that locate to within +/- 5 km of the plate interface that had 3 or more phase arrivals detected at permanent NCSN stations. The events are scaled by their magnitude and colored according to depth. Time series showing the detections of all events is shown in Fig. A-3. The Fortuna cluster events are outlined in blue, the time series showing these events can be found in the main text Fig. 5. All other events outside of this CM04 cluster are outlined in gray.

31) A-3 Time Series of All Plate Interface Events

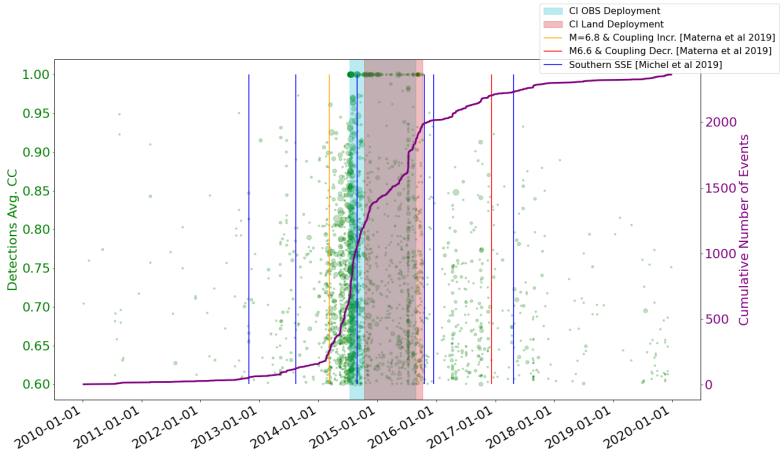

Fig. A-3. Time series of all template matched detections. All 200 template locations can be seen in Fig. A-2.

32) A-4 Map Number of Template Matched Detections

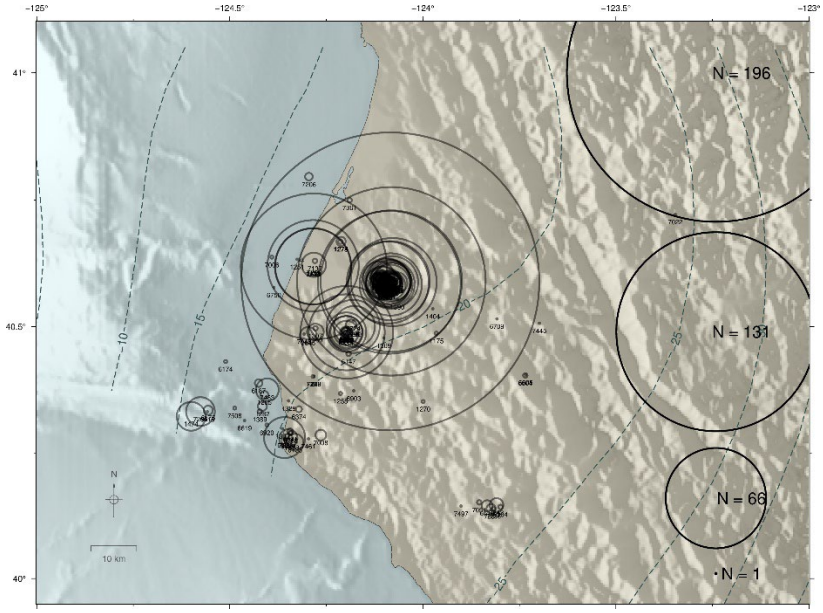

Fig. A-4. Figure showing plate interface templates where the circles are scaled by the number of match detections that the template event detected.

33) A-5 First Motion Focal Mechanism Examples

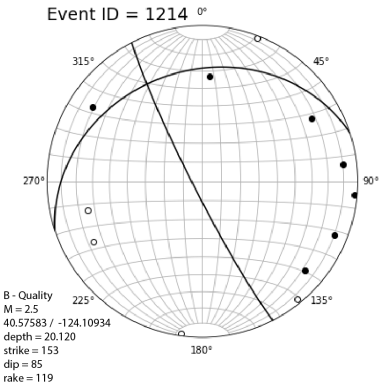

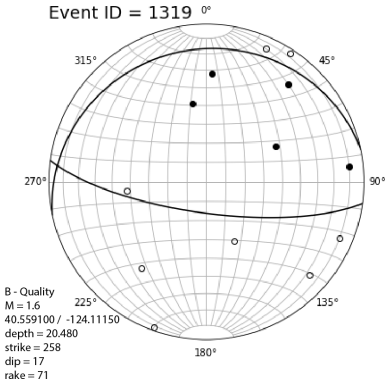

Fig. A-5. Lower hemisphere stereonet projections depicting two examples of fault planes generated by Hash, shown by great circle paths lines. Markers are plotted according to azimuth and take of angle. Take off angles that are up rather than down are translated to their lower hemisphere projection. Short period CI CM stations were installed with reverse polarity identified clearly by teleseismic event, and were corrected. Closed circles depict compression or ups on seismograms and open circles indicate dilations or downs on seismograms. (top) shows an example of a mostly strike slip event with 1 arrival that is inconsistent with the generated mechanism. (bottom) an example of a dip-slip event, that could not easily be fit with a strike-slip mechanism without violating several arrivals.

34) A-6 Comparison of Results to Existing ANSS Catalog

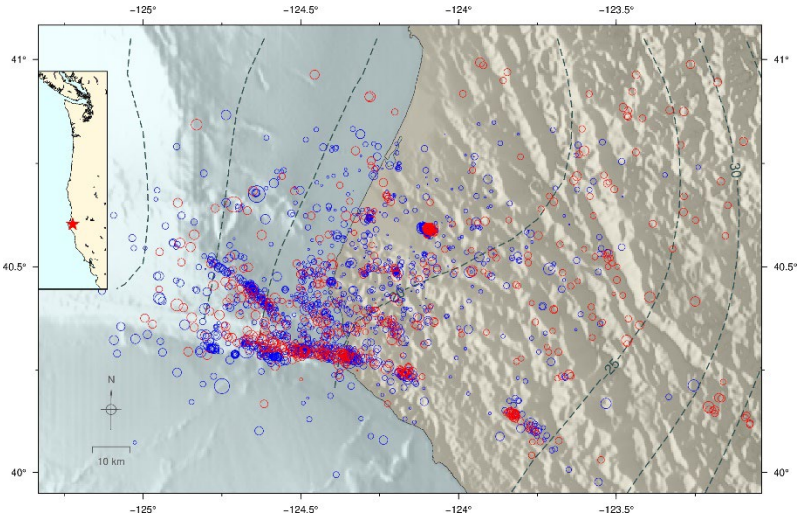

Fig. A-6. Map showing how this study's locations (n = 1452) compare those in the ANSS Comat catalog (n = 552) over the same time period (Jul 2014 - Oct 2015). Our final locations are in blue, and the existing ANSS locations are shown in red, and the

marker sizes are scaled by magnitude. Notice the linear features that are apparent in the relocations that are only hinted at in ANSS catalog, and the identification of many more small events.

35) A-7 Events and Crustal Faults?

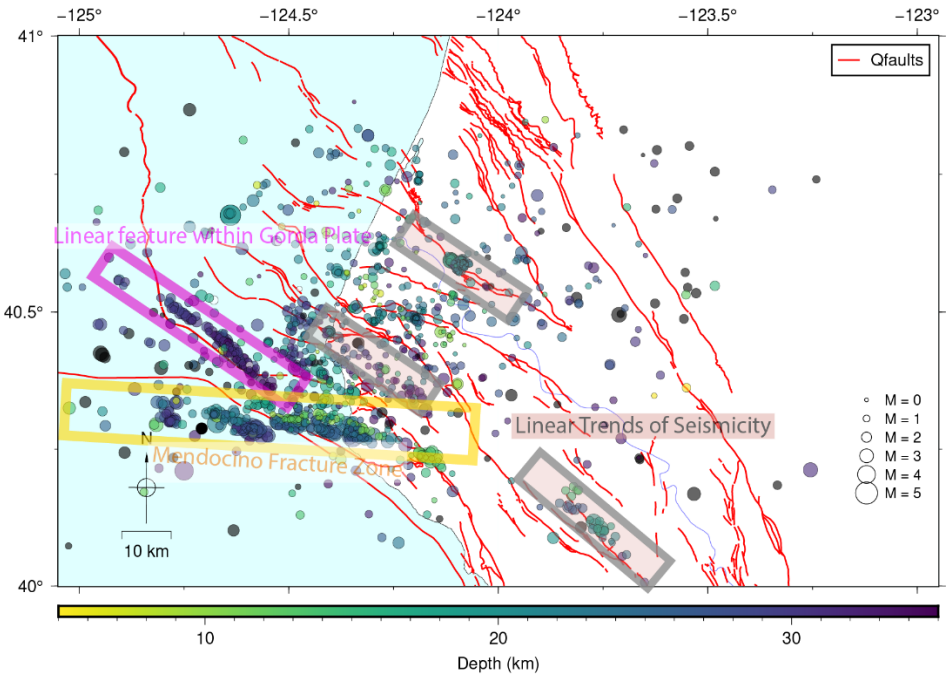

Fig. A-7. Events colored by depth and USGS q-faults database indicated with red lines. Most events are too deep to confidently correlate quaternary faults. Gray boxes pointing out linear trends of seismicity that are pointed in the Discussion section of the main text.

36) A-8 Gutenberg Richter Magnitude Distribution

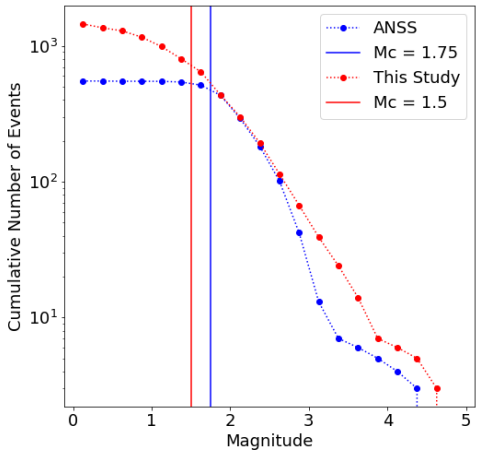

Fig. A-8. This figure shows the Gutenberg Richter plot of magnitudes vs cumulative number of events below each bin. Note the clear difference in magnitude of completeness between existing ANSS catalog over the same time period and region of interest as our study. Magnitude of completeness was calculated with maximum curvature method, using bin spacings of 0.2.

37) A-9 Fortuna Cluster Weak Migration Pattern

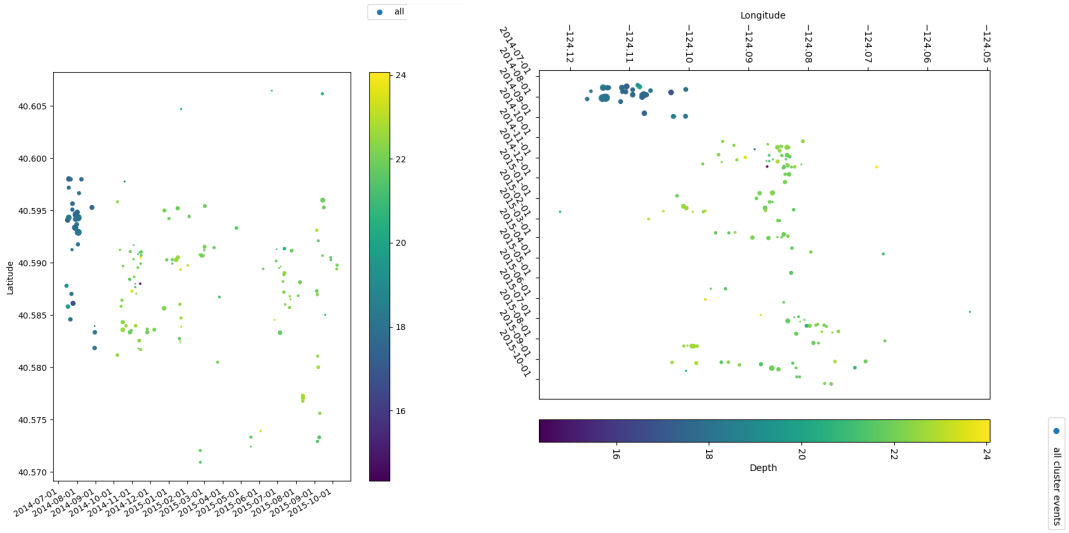

Fig. A-9. Showing cluster of events with weak migration patterns (top) latitude (bottom) longitude variation with time. A hint of migration from NE-shallower to SW - deeper

38) A-10 Temporal Relationship of Seismicity with Borehole Strain Meters

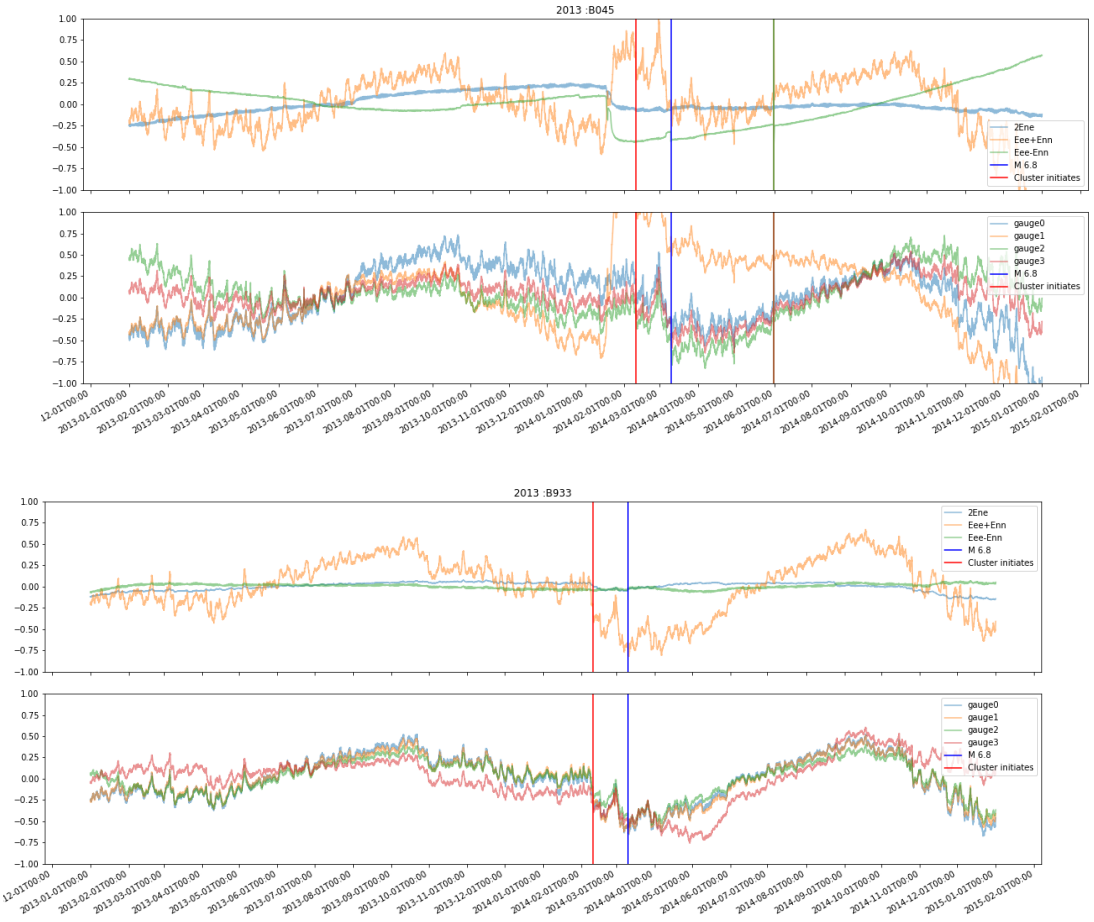

Fig. A-10. Figure showing nearby borehole strainmeters B045 (top) & B933 (bottom). Station B935 is not shown because of instrumental malfunctioning, documented on Unavco website. For station locations see Fig. 1. 2Ene, Eee + Enn, and Eee - Enn components are corrected strain data level 2, and the raw gauge 0,1,2,3 are shown in the figure below. The red line indicates the timing of cluster initiation as shown in Fig. 5,(Feb 2014). Blue line shows the timing of the M 6.8 earthquake. Note the drop in the areal strain at the time cluster initiation.

Appendix B – Supplemental Information for Chapter 2

1-B. Merging well and seismic data

The delta time log from the well LAS files (in depth) were used to create velocity models for each well, in order to import and combine with the seismic data (in two-way travel time). We used a moving average over a 100-sample window (sampling rate of 6 inches) of the delta time logs, dropping the first 200 samples because these were often providing unrealistic values. The delta time data were then converted to velocity in meters per second. We then interpolated the velocity values as a function of depth and extrapolated to water velocity at the seafloor. The 1D velocity models could then be imported into interpretation software and display the well track in two-way travel-time rather than depth. The stratigraphic logs that indicating unit changes which are in measured depth can then be imported into interpretation software and displayed in two-way travel-time (Fig. A-3 & A-7). We then use arbitrarily oriented seismic lines within the 3D volume to connect wells and interpret the horizon first at well log and then map in full 3D space.

2-B. Seismic Resolution

The resolution of seismic images and volumes are dependent on several parameters intrinsic to acquisition.

The horizontal resolution is limited by the Fresnel zone of the spherically expanding wavefront from the seismic source that forms a circular area on a reflection surface. This can be expressed as:

$$r = \frac{v}{2}\sqrt{(\frac{t}{f})}$$

Where v is the velocity of the medium, t is two-way travel time, and f is the dominant frequency. If we assume v = 2500 m/s which is a typical velocity at t = 1 s two-way travel time and dominate frequency f = 30 Hz from the source given by the power spectral density (Fig. 3). Fresnel horizontal resolution limit is ~ 230 m. However, seismic migration seeks to restores diffracted energy to its correct location, the reflection or diffraction point, it is often assumed that the horizontal resolution of fully 3D migrated seismic data is approximately equal to the seismic bin spacing. For the Chevron volume this is 50 x 25 m (crossline x inline directions) and the Shell volume the seismic bin spacing is 25 x 12.5 m (crossline x inline directions).

The vertical resolution in seismic data is dictated by the Rayleigh limit of resolution that describes two reflecting events should be separated by a half cycle otherwise the events will constructively interference and be unresolvable:

$$h = \frac{\lambda}{4}$$

Where h is the thickness limit of resolution and λ is the dominate wavelength of the source. Using $\lambda = v/f$ and substituting in we have

$$h = \frac{v}{4f}$$

Using the same values as before, v = 2500 m/s and f = 30 Hz gives a horizontal resolution limit of ~ 20 m. Vertical resolution is unaffected by migration and the dominant frequency doesn't change much with depth; however, rock velocities increase with depth (Fig. B-1) so vertical resolution decreases. Even at velocity 4000 m/s the vertical resolution is still ~ 30 m.

The spatial resolution for these seismic datasets is approximately the rectangular cuboid (voxel) of the seismic bin dimension x the vertical resolution. These spatial dimensions and limits of resolution are larger than many geologic attempts at quantifying damage (resolutions undefined) and many of the fine scale features seen at outcrops are unresolvable these seismic datasets. The grid cell size (typically ~ 1x1 km) for tomographic studies of fault zones are generally 2 orders of magnitude larger than those of the present study.

39) B-1 Well Derived 1D Velocity Models

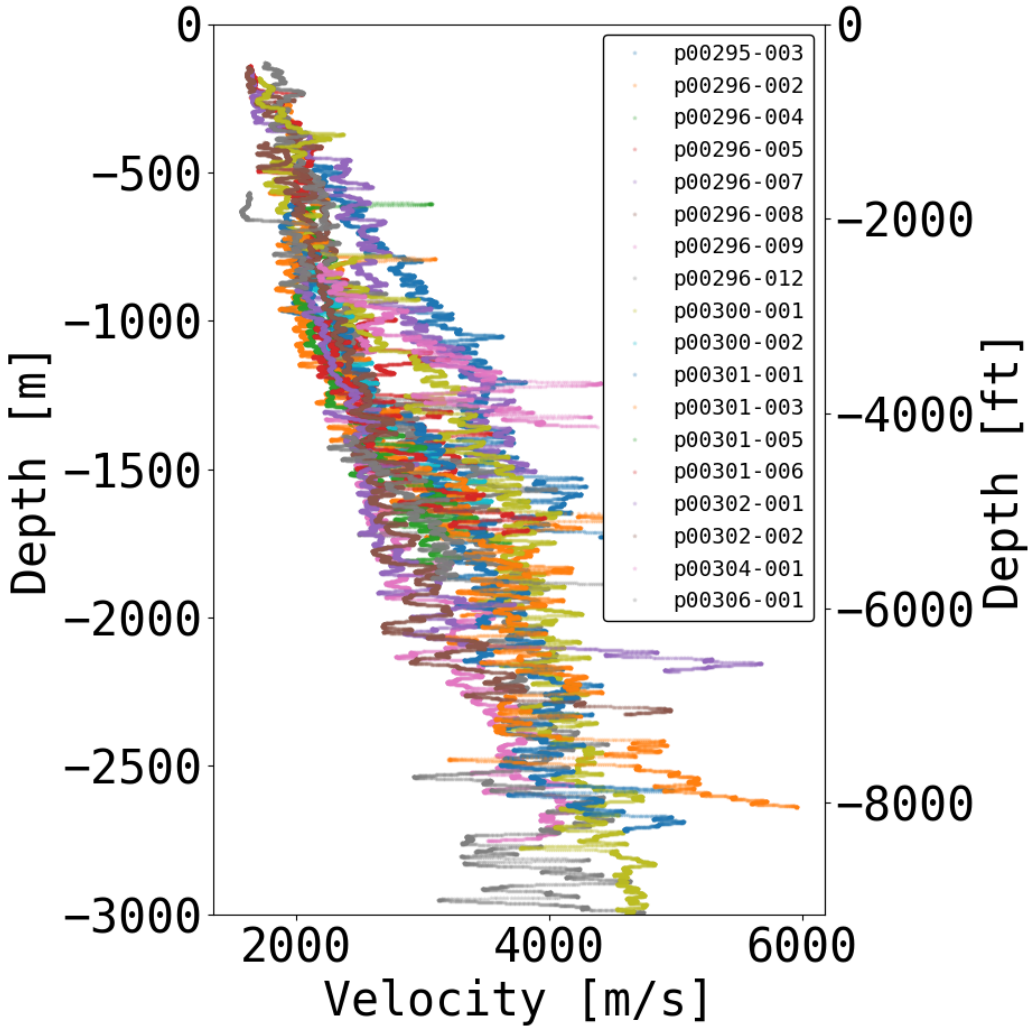

Fig. B-1. Showing calculated velocity models (described above) used to convert two-way travel time to depth and depth to two-way travel time. The data were and smoothed using a moving hamming taper window.

40) B-2 Fault Detections in 2D and 3D

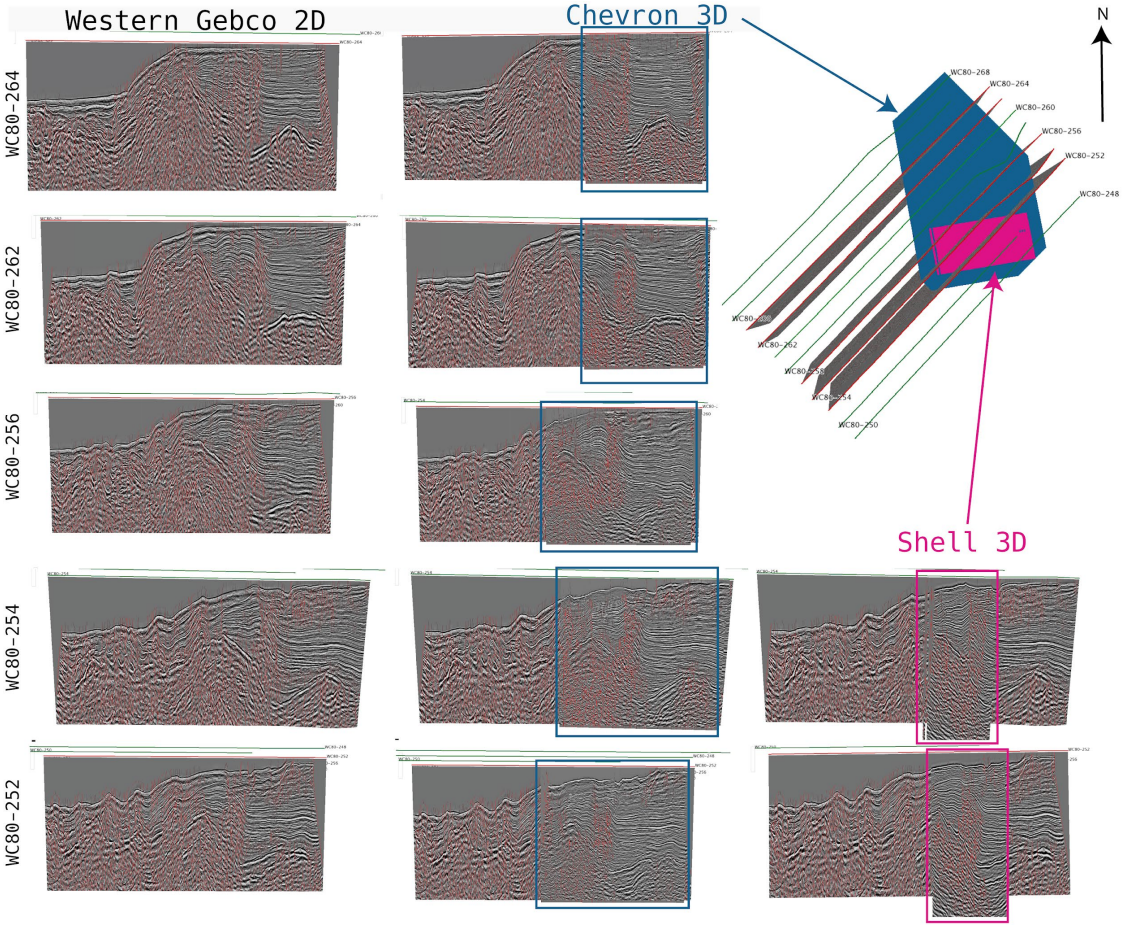

Fig. B-2. Selected two-dimensional (2D) seismic lines that were processed with dip-steered diffusion filtering, and 2D thinned fault likelihood computed, shown in red. The map in the upper right shows the 2D lines that intersect the volume. The lines in red are the examples shown. The left panels show 2D Western Gebco seismic lines, the center panel shows a line oriented in the same orientation as the 2D lines through the Chevron volume that are outlined in dark blue, with chevron seismics and thinned fault likelihood computed on the three-dimensional (3D) volume. The right panel shows lines oriented to the 2D lines of the shell seismics and thinned fault likelihood computed on the 3D volume.

41) B-3 Example of Well Logs, Horizons, and Reflection Profiles

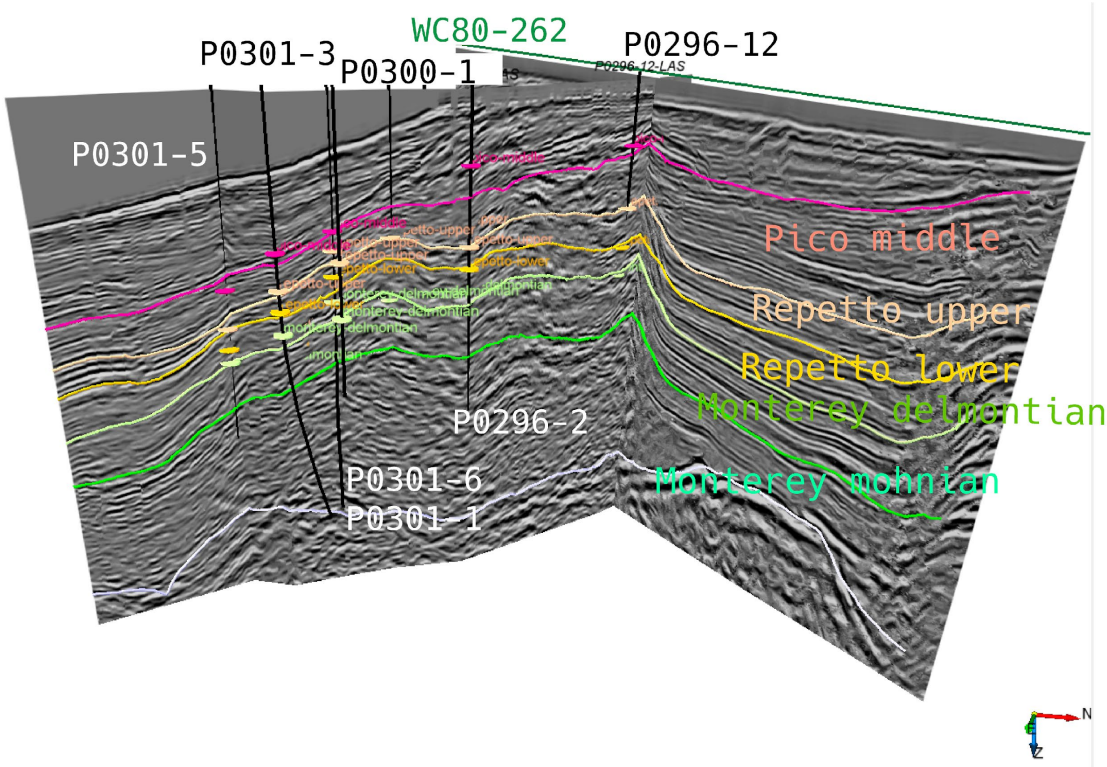

Fig. B-3. Perspective view looking from east to west of seismics, well logs, and horizons. The seismic line running through the near vertical wells is an arbitrary line running through most of the wells, the gray scale shows the dip-steered diffusion filtered Chevron volume seismics. The perpendicular line shows two-dimensional (2D) Western-Gebco seismic line (WC80-262) also with dip-steered diffusion filtering. Overlain on the seismics are the mapped horizons shown in bright colors. Note the agreement with the 2D seismics. The black near vertical wells contain colored disk at the lithology contacts.

42) B-4 Impact of Binning on Exponential Fits

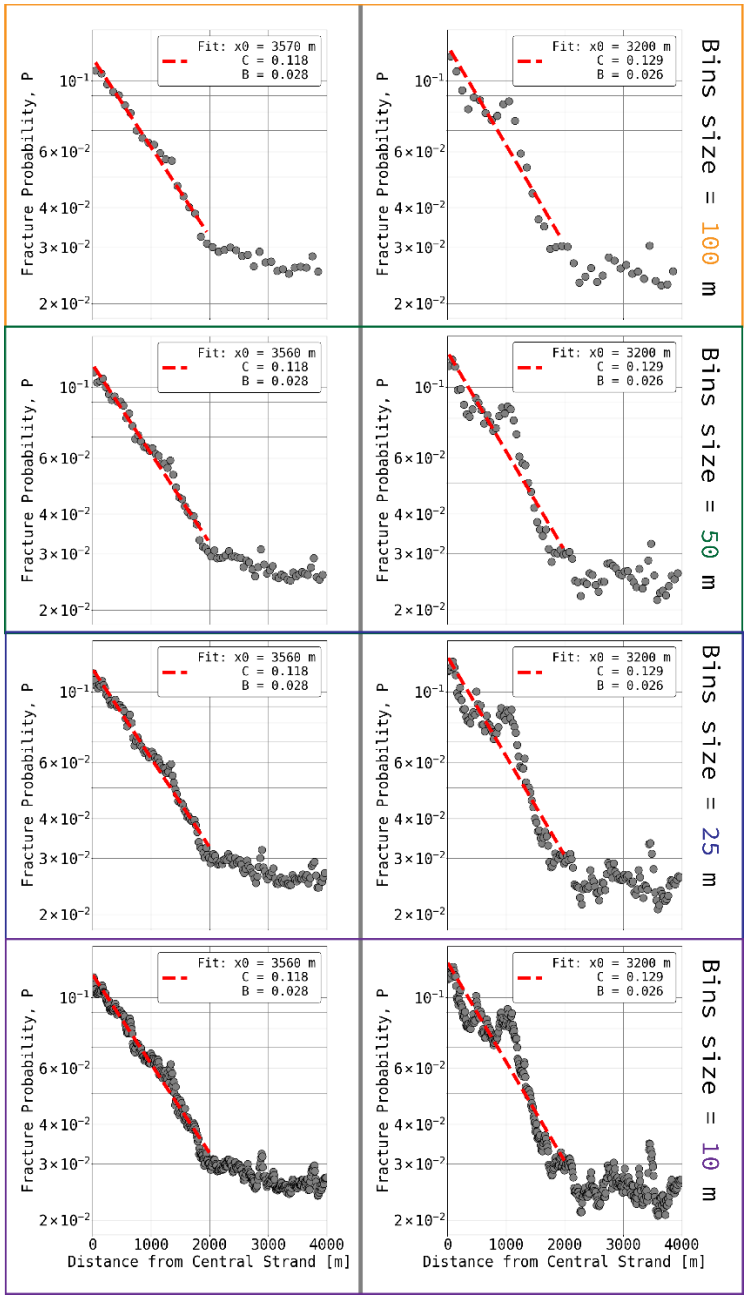

Fig. B-4. Showing tests of bin sizes 100, 50, 25, 10 m from top to bottom. (left) plots show results for the Chevron volume and (right) shows results for the Shell volume. Note Xo, C, and B are insensitive to the tested bin dimensions.

43) B-5 Bootstrap Results for Exponential Fit Parameters

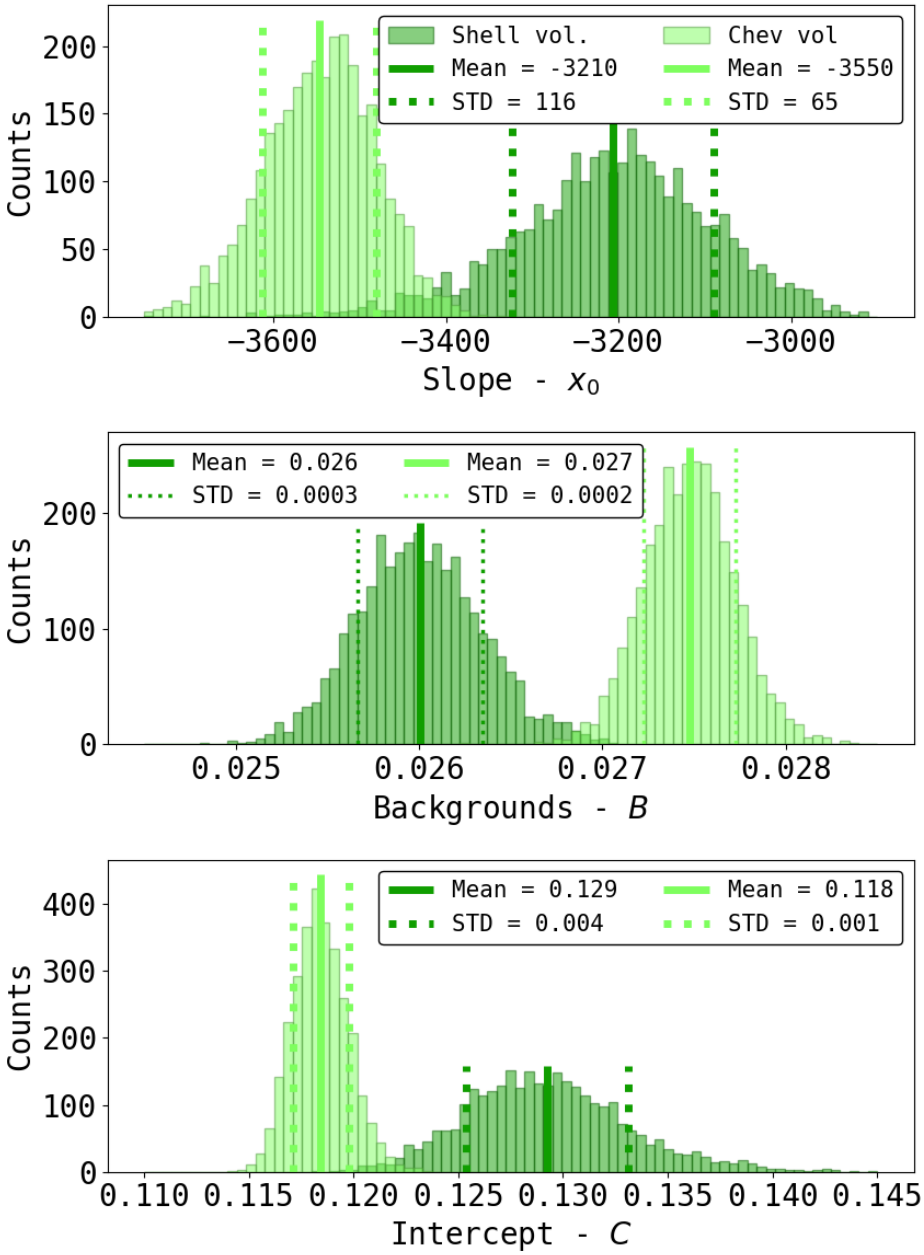

Fig. B-5. Bootstrapping histograms & distributions for exponential fit parameters Xo, C, and for the background B from Fig. 2-5 and Table 1. Lime green and forest green represent the Chevron and Shell volumes. Data were randomly resampled with replacement 3000 times and least squares fits were performed.

44) B-6 Bootstrap Results for Exponential Fit Parameters - Lithology

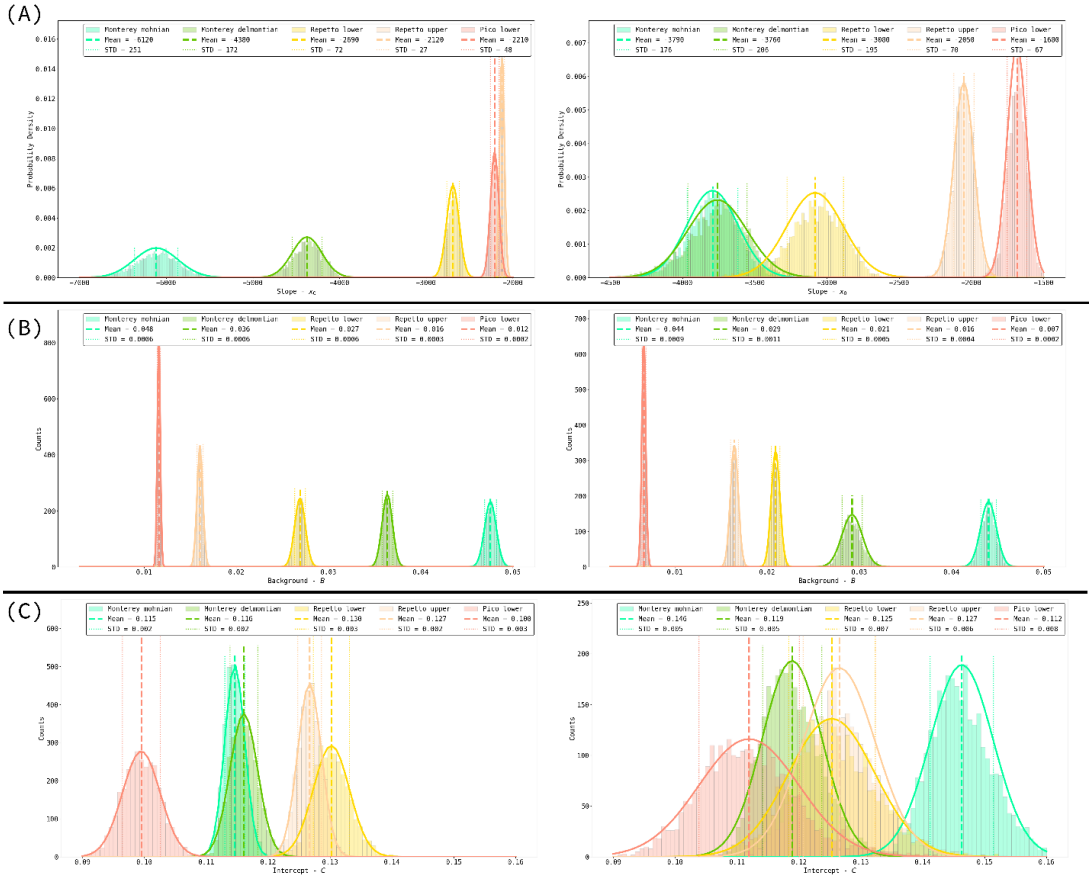

Fig. B-6. Bootstrapping distributions for exponential fit parameters Xo, C, and background B from Fig. 2-6 and Table 1. (A) Exponential slopes Xo, (B) backgrounds B (mean of fracture probability from distances, 2000 – 3500 m), (C) Intercepts C. (Left) plots are results for the Chevron dataset, and (right) are results for the shell dataset. Data were randomly resampled with replacement 3000 times and least squares fits were performed to obtain Xo and C.

45) B-7 Example of Constrained Lithology

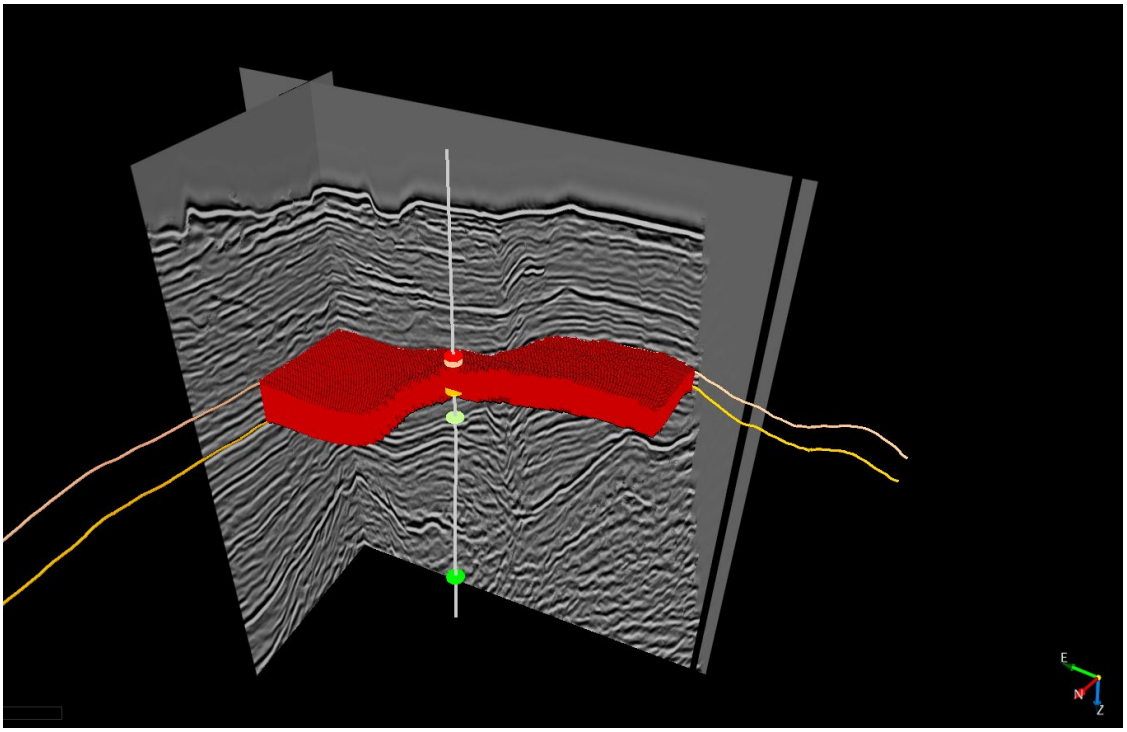

Fig. B-7. Perspective view looking at Shell Seismic inline 1325 and crossline 1700 along with Repetto upper and lower horizons projected onto the seismic sections. The vertical well line log P301-1 in white, with oval markers indicating the location of lithology changes converted from depth to two-way travel time that were used to constrain the horizons. The red volume has been constrained to between the upper and lower surfaces and cut back to reveal the agreement between the well-contacts, horizons, and subset of volume.

46) B-9 Fault Damage Width Comparison with Compilation

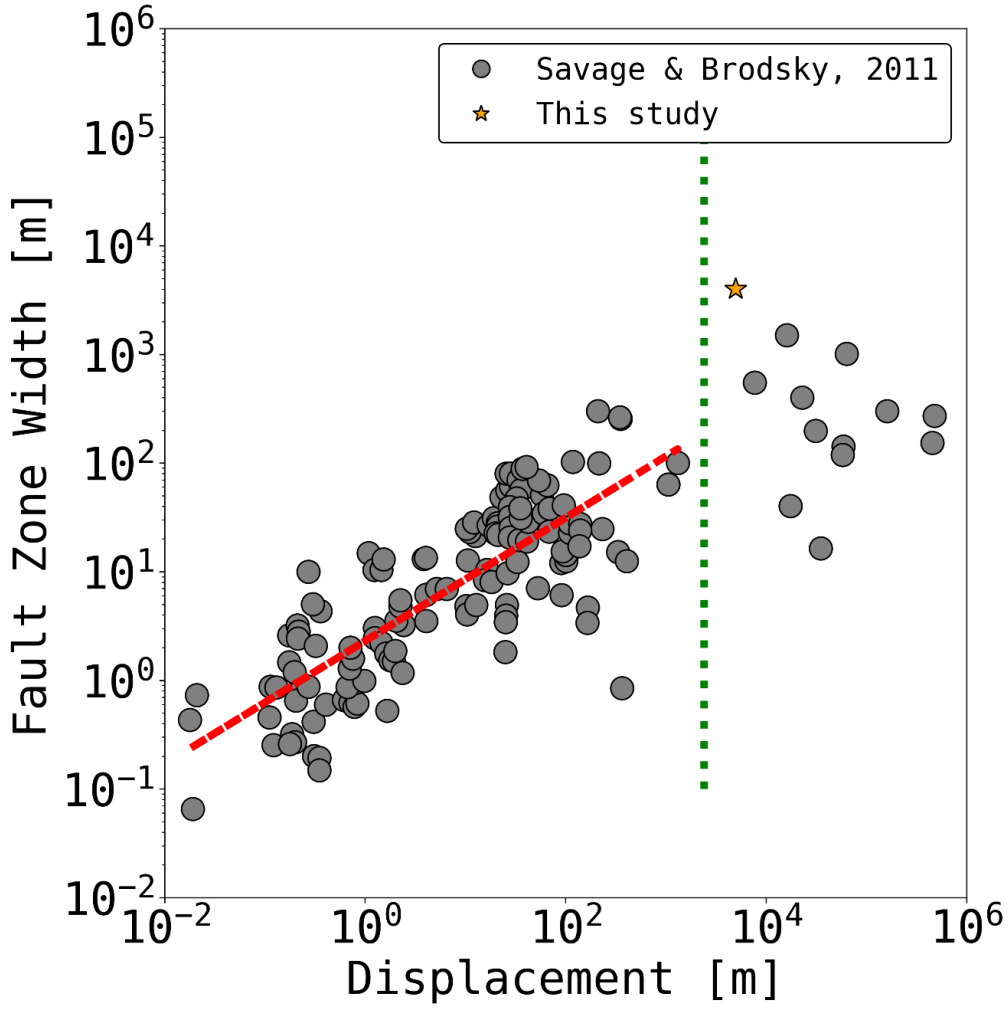

Fig. B-8. Showing results from the present study to compilation of fault zone widths vs displacements results (Savage and Brodsky, 2011). Dashed green line shows the most likely change point determined using Bayesian information criteria, see their

paper for more details. Dashed red line is a power law fit through the data (first slope), of the form $W = Cx^m$, and $m = 0.56$. We take displacement = 5 km (Brankman and Shaw, 2009) and total width = 4 km.

47) B-9 Comparison to Other Automated Damage Detection Study

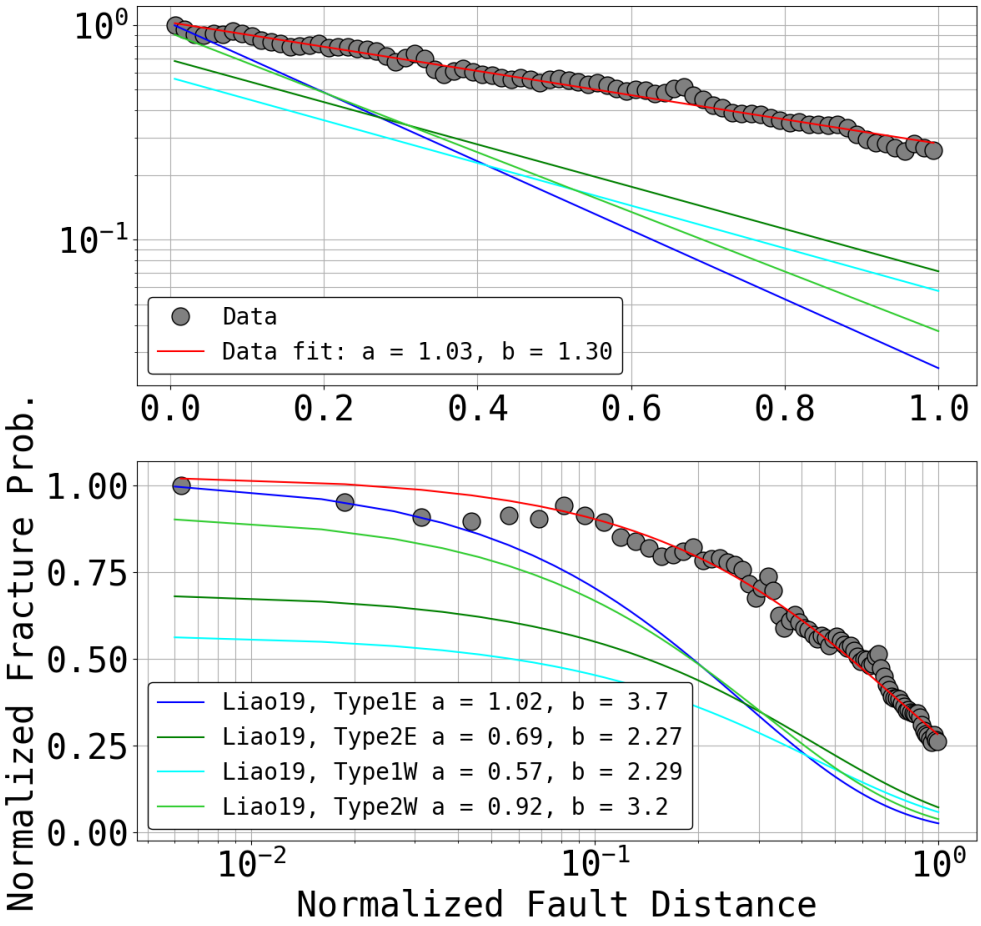

Fig. B-9. showing exponential decay results of this study and Liao et al., 2019. The gray circles (same data as Fig. 2-5. Chevron) are normalized fracture probability with normalized distance from the fault, where normalization is done at the edge of the damage zone (2000 m). The red line is the exponential fit to the data P = ae-bx to match the results in the Liao et al., study. The blues and greens are fits done in the

Liao et al., study. (top) is semilogy and (bottom) is semilogx, to match Fig. 8 in Liao et al., 2019. The mean R2 value for the reported Liao19 fits was 0.72 and ours is 0.99.

48) B-10 Fracture Probability Lithologies for 4.5 of Fault Length

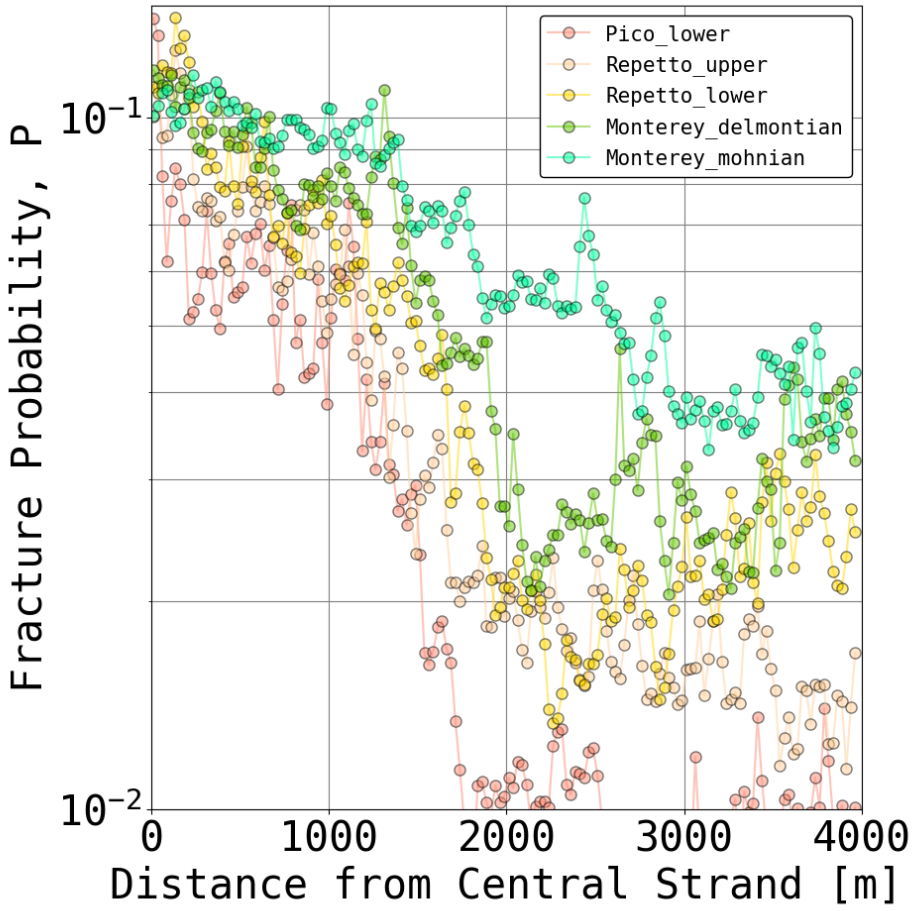

Appendix C – Supplemental Information for Chapter 3

1-C. 2021 Sproul MCS seismic processing

The collected high-resolution multichannel seismic (MCS) and coincident Chirp data were acquired during field operations (2021-614-FA) aboard the R/V Sproul from May 13, 2021, to May 22, 2021. The survey was conducted offshore of southern California, specifically in the inner continental borderlands tectonic region. The focus of the survey was to collect seismic lines perpendicular to the Palos Verdes Fault with close adjacent line spacing of approximately 500 meters to explore the spatial properties and distribution of faulting in the shallow subsurface.

For the MCS data acquisition, a SIG multi-tip sparker sound source was used, towed several meters below the sea surface. The source signal was recorded using hydrophones, although the recorded data were not used in subsequent processing steps. The seismic reflection data was recorded using a ~120 m Geometrics GeoEel 40-channel streamer, with group spacings of 3.125 meters and a sampling rate of 0.25 ms. The tow depth of the streamer was controlled using Geospace Navigator birds, maintaining a depth of approximately 2 meters below the sea surface. The acquisition vessels operated at a speed of ~ 4 knots during data collection.

Prior to any interpretation or application of fault detection attributes several processing steps were conducted on the MCS data. The following describes the processing steps undertaken.

Shearwater Reveal 4 and 5 were used to process the raw seismic data:

1. Raw data import: the raw SEGD files were imported, and navigation and timing headers were populated from shipboard GPS records. The latitude and longitude navigation were converted to Universal Transverse Mercator zone 11 North datum. Static corrections were performed.

2. Source and receiver geometry were calculated by projecting the survey setup geometry back from measured distances from shipboard GPS antennae. The distance from the antennae was 37 m and 78 m for the source and channel 1 respectively. We used a seismic bin spacing of 3.125 meters and the data were bandpass filters 30-60-1100-1800 in freq. domain using filter length 500 ms.

3. Traces were renumbered and a brut stack of data was done at water velocity for quality control and so water bottom (seafloor) could be picked. Picking was done manually approximately every ~ 100 CMP (~150 m) on slope and ~ 400 CMP (~600 meters) on the shelf about 15 ms above the seafloor.

4. Trim-statics were performed to correct for any inconsistencies in stream tow depth (slanted or sagging streamer). Pre-stack data were moved out at water velocity and cross correlation were performed on low pass filtered data windowed around the seafloor reflection in order to make small shifts in the traces and ‘flatten’ the streamer.

5. RMS Seismic velocities were determined by semblance analysis. Seismic velocity was determined as a function of depth by finding the velocity that maximizes multi-trace similarity over a time window.

6. Surface Related Multiple Elimination was carried out in a multi-step workflow that was designed with the help of Shearwater. 10 extra near source offset traces were extrapolated from the data. The now 50 (10 + 40) channel data were interpolated by a factor of 2 to a value of 100 channels per shot with offsets ranging from 0 - 200 m from the source. Sea Surface related multiples are calculated from the data using an internal algorithm (Verschuur et al., 1992). The estimated multiple was top muted at 2 x the water bottom pick to avoid contamination of data. A two-step (global with larger patch sizes and local with shorter patch sizes) adaptive subtraction was done using the renumbered data and the muted predicted multiple.

7. Deconvolution was done pre-stack. A spiking gap length of 2.9 ms was used, and it was determined using the second crossing of the autocorrelation on stacked gathers. An operator length of 15 ms, designed over 21 traces and prewhitening of 3% was used. The filter was designed in a window around the water bottom time (WBT - 50 ms and WBT + 200 ms)

8. Normal moveout was calculated using the previously determined RMS velocity pick table. A stretch mute was applied at 180% with a taper of 15

ms. A bandpass filter (50-100-700-900 Hz) and top mute (WBT) was applied.

9. Trim Statics was done prior to common midpoint stacking. The reference trace was determined by stacking gathers - 100/30db - 200/60db limit offsets for gather stacking 0-100 m (gives a non-stretched pilot to match to) compute correlations in a window FB_TIME - 3 ms to FB_TIME + 6 ms (FB_TIME was computed using an autopicker)

10. Migration was done post-stack. Mutes were applied above the seafloor and at depths beyond 1400 ms TWTT below the seafloor. The migration was done at 1400 m/s at frequencies less than 750 Hz.

11. Structurally oriented denoising was done in 3 steps:

    a. Seismic dips were estimated on low passed data (50-100-130-200 Hz). Dip search increments were 20 CMPs by 30 ms TWTT. The dip search radius was calculated over 5 increment binds and a semblance window of 50 ms.

    b. A bottom mute was applied to the dip estimate (WBT + 400 ms) to eliminate the dip estimation and denoising of low signal to noise data beyond 400 ms.

    c. Use SODenoise (Reveal) tool to use the dip table median filter the data.

12. Export data as segy files.

49) C-1 Track Line Map - 2021 Sproul Cruise

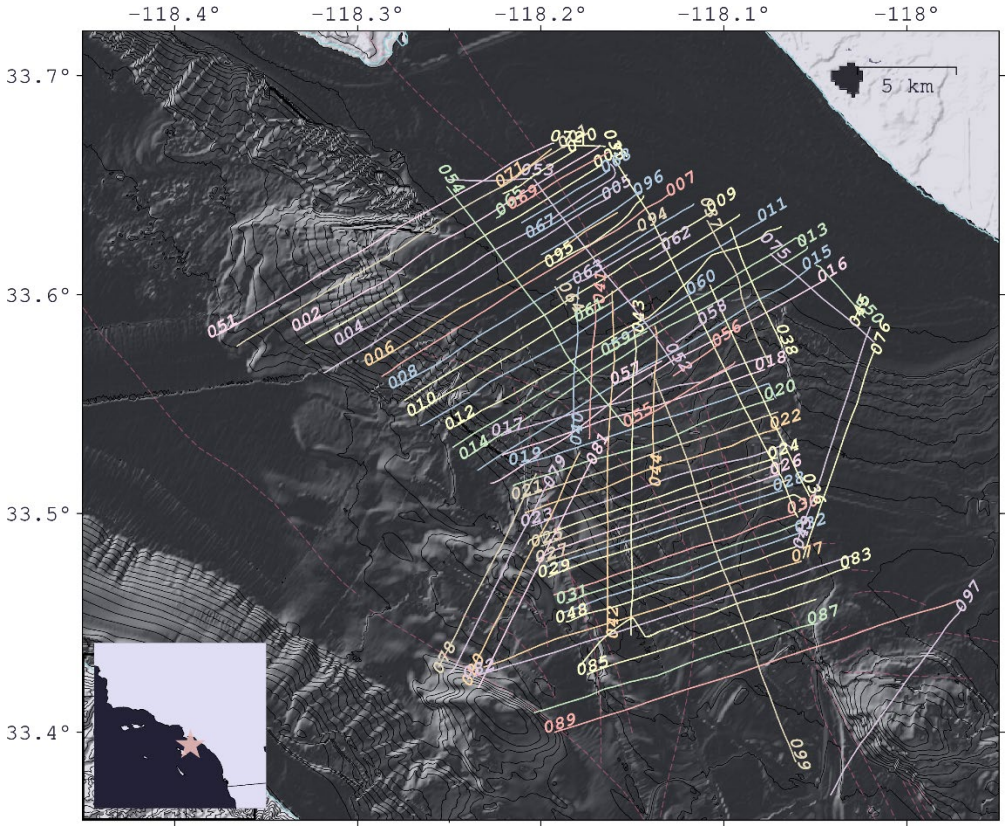

Fig. C-1. Lines map highlighting the study area and corresponding seismic survey similar to Fig. 1-1 in the main text. The solid lines are colored-coded and labeled in various pastel colors for clarity. The dashed pink lines represent the Offshore Quaternary United States Geology Survey Faults (Walton et al., 2020). The green polygons depict the bounds of the three-dimensional (3D) marine active source datasets used in Alongi et al. (2022) study of the fault damage zone. The lime green line depicts the boundaries of the 1976 Unocal (Chevron) volume and forest green depicts the boundaries of the 1984 Shell volume.

50) C-2 Frequency Spectral Comparison

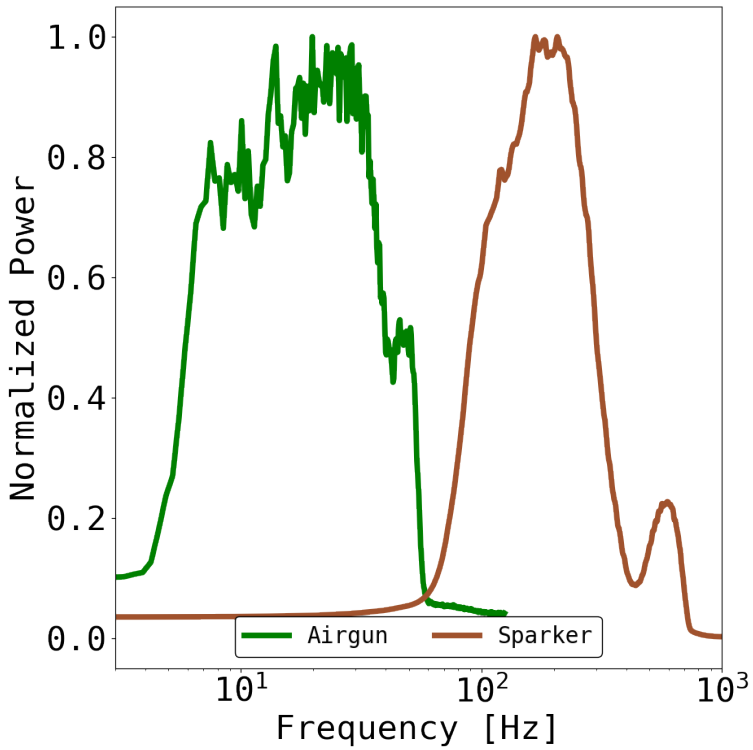

Fig. C-2. Frequency spectra comparison of the data used in the present study represented by the (brown curve), and Alongi et al., (2022) (green line). The plot highlights the significant difference in frequency content between the two datasets.

51) C-3 Shelf Scarp Height Measurements

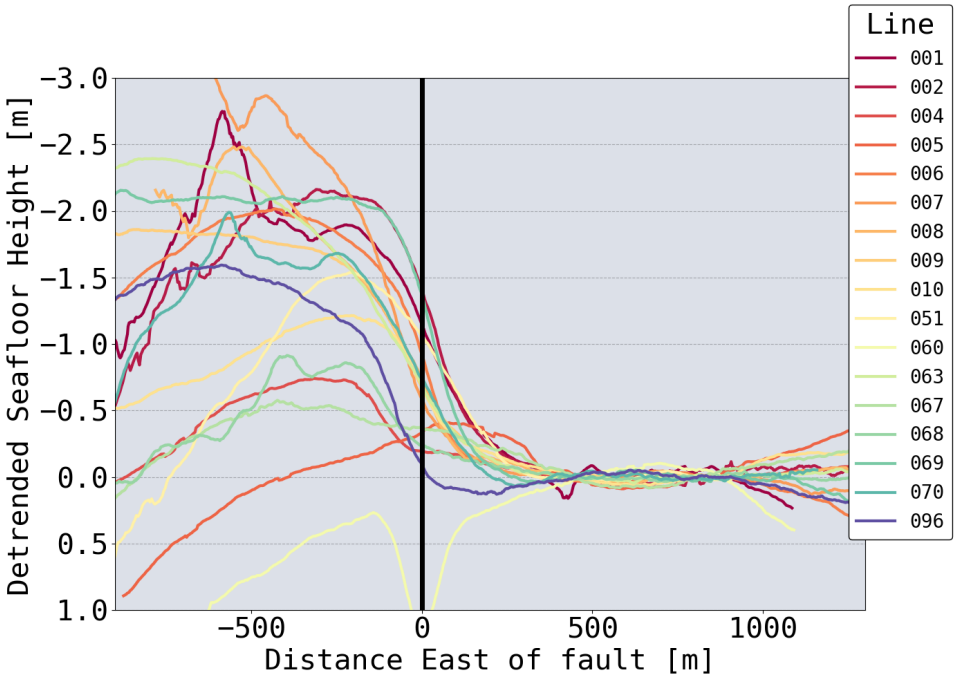

Fig. C-3. Detrended profiles showing fault-related scarps on chirp sub-bottom profiles along the San Pedro Shelf. Each colored curve represents a unique profile of the mapped seafloor reflection. The curves are detrended by the trend of the seafloor east of the fault to highlight the relative scarp height.

52) C-4 Histograms of Thinned Fault Likelihood from MCS

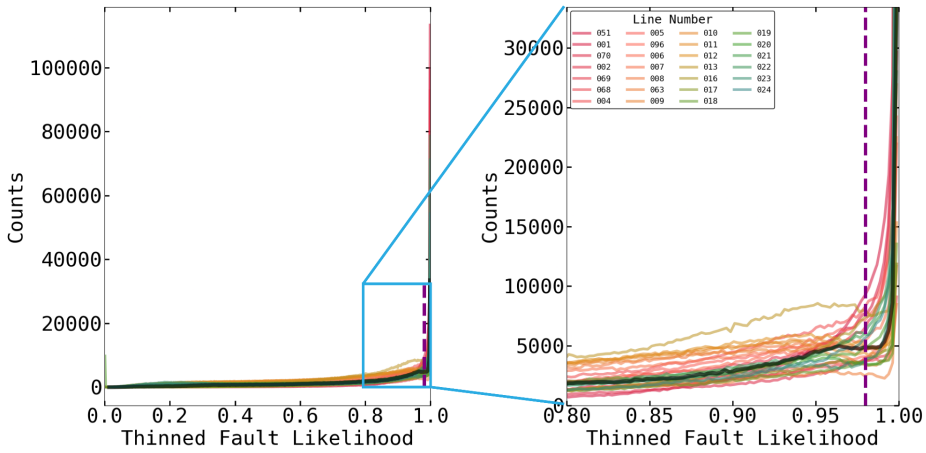

Fig. C-4. Histograms of thinned fault likelihood for lines perpendicular to the fault. Results are shown for depth ranges from the seafloor to seafloor + 400 ms two-way travel time and cover a lateral distance of 6 km from the fault. Each line is depicted individually in color and arranged according to its position along the fault, reds indicating northern locations and the blues representing southern positions. The dark line depicts the median stack of all the lines shown, and the dashed purple line shows the thinned fault likelihood threshold utilized in the study. (Left) The full range of thinned fault likelihood and (right) shows a zoomed in view.

53) C-5 Azimuth Distribution from Active Fault Strand

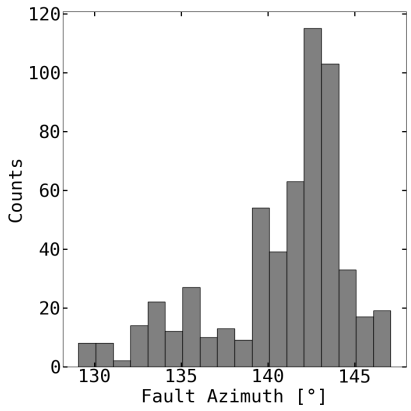

Fig. C-5. Histogram of the azimuths calculated for the fault trace that are shown in Fig. 3-5.

54) C-6 Estimating Displacement from Fault Length

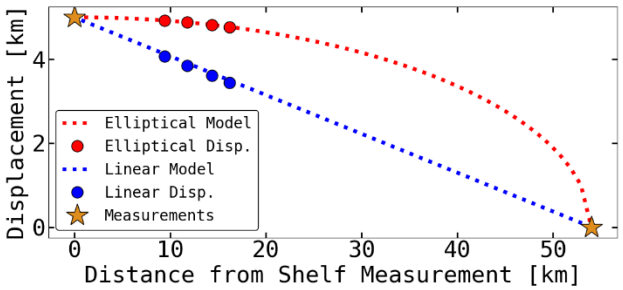

Fig. C-6. Displaying the difference in modeled displacement fault length scaling relationship (dashed lines) on the overall displacement on the 4 subsections (circles) of the southern extent of the study area. The yellow stars show the measured points (on the shelf and 27 km away at Lasuen Knoll)

55) C-7 Shelf TFL – Subdivided by Depth

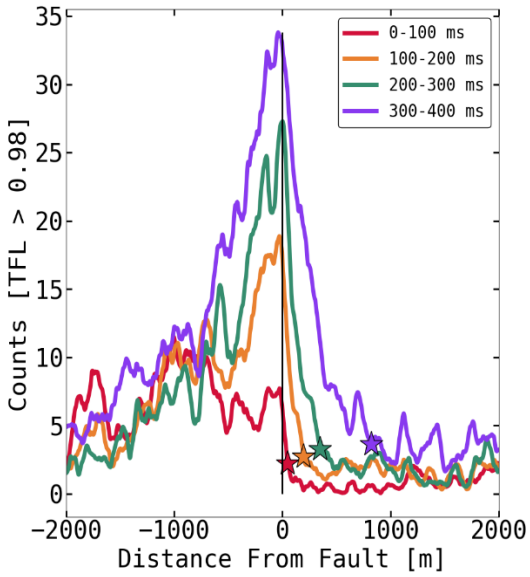

Fig. C-7. Displaying the Thresholded thinned fault likelihood plotted versus distance east of the fault, presented in different colors to represent different depths. Depth ranges are shown in the legend in the upper right of the figure where the numbers indicate the depth below the seafloor. The stars denote the location of 5% of the peak TFL value.

References

Abercrombie, R. E., & Rice, J. R. (2005). Can observations of earthquake scaling constrain slip weakening? Geophysical Journal International, 162(2), 406–424. https://doi.org/10.1111/j.1365-246X.2005.02579.x

Alaei, B., & Torabi, A. (2017). Seismic imaging of fault damaged zone and its scaling relation with displacement. Interpretation, 5(4), SP83–SP93. https://doi.org/10.1190/INT-2016-0230.1

Alcalde, J., Bond, C. E., Johnson, G., Ellis, J. F., & Butler, R. W. H. (2017). Impact of seismic image quality on fault interpretation uncertainty. GSA Today. https://doi.org/10.1130/GSATG282A.1

Alongi, T., Brodsky, E. E., Kluesner, J., & Brothers, D. (2022). Using active source seismology to image the Palos Verdes Fault damage zone as a function of distance, depth, and geology. Earth and Planetary Science Letters, 600, 117871. https://doi.org/10.1016/j.epsl.2022.117871

Atterholt, J., Zhan, Z., & Yang, Y. (2022). Fault Zone Imaging With Distributed Acoustic Sensing: Body-To-Surface Wave Scattering. Journal of Geophysical Research: Solid Earth, 127(11), e2022JB025052.

Atwater, T. (1970). Implications of Plate Tectonics for the Cenozoic Tectonic Evolution of Western North America. Geological Society of America Bulletin, 81(12), 3513. https://doi.org/10.1130/0016-7606(1970)81[3513:IOPTFT]2.0.CO;2

Aydin, A., & Du, Y. (1995). Surface rupture at a fault bend: The 28 June 1992 Landers, California, earthquake. Bulletin of the Seismological Society of America, 85(1), 111–128.

Aydin, A., & Nur, A. (1982). Evolution of pull-apart basins and their scale independence. Tectonics, 1(1), 91–105.

Bahorich, M., & Farmer, S. (1995). 3-D seismic discontinuity for faults and stratigraphic features: The coherence cube. The Leading Edge, 14(10), 1053–1058.

Bartlow, N. M. (2020). A Long-Term View of Episodic Tremor and Slip in Cascadia. Geophysical Research Letters, 47(3). https://doi.org/10.1029/2019GL085303

Bartlow, N. M., Miyazaki, S., Bradley, A. M., & Segall, P. (2011). Space-time correlation of slip and tremor during the 2009 Cascadia slow slip event: CASCADIA SLOW SLIP AND TREMOR MIGRATION. Geophysical Research Letters, 38(18), n/a-n/a. https://doi.org/10.1029/2011GL048714

Behl, R. J., Moores, E., Sloan, D., & Stout, D. (1999). Since Bramlette (1946): The Miocene Monterey Formation of California revisited. Classic Cordilleran Concepts: A View from California: Geological Society of America, Special Paper, 338, 301–313.

Bense, V., Gleeson, T., Loveless, S., Bour, O., & Scibek, J. (2013). Fault zone hydrogeology. Earth-Science Reviews, 127, 171–192.

Ben-Zion, Y. (1998). Properties of seismic fault zone waves and their utility for imaging low-velocity structures. Journal of Geophysical Research: Solid Earth, 103(B6), 12567–12585. https://doi.org/10.1029/98JB00768

Ben-Zion, Y., Peng, Z., Okaya, D., Seeber, L., Armbruster, J. G., Ozer, N., Michael, A. J., Baris, S., & Aktar, M. (2003). A shallow fault-zone structure illuminated by trapped waves in the Karadere-Duzce branch of the North Anatolian Fault, western Turkey. Geophysical Journal International, 152(3), 699–717. https://doi.org/10.1046/j.1365-246X.2003.01870.x

Ben-Zion, Y., & Sammis, C. G. (2003). Characterization of Fault Zones. Pure Appl. Geophys., 160, 39.

Ben-Zion, Y., & Sammis, C. G. (Eds.). (2010). Mechanics, structure and evolution of fault zones. Birkhäuser.

Berg, S. S., & Skar, T. (2005). Controls on damage zone asymmetry of a normal fault zone: Outcrop analyses of a segment of the Moab fault, SE Utah. Journal of Structural Geology, 27(10), 1803–1822. https://doi.org/10.1016/j.jsg.2005.04.012

Bilek, S. L., Lay, T., & Ruff, L. J. (2004). Radiated seismic energy and earthquake source duration variations from teleseismic source time functions for shallow subduction zone thrust earthquakes: SOURCE TIME FUNCTIONS SHALLOW SUBDUCTION. Journal of Geophysical Research: Solid Earth, 109(B9), n/a-n/a. https://doi.org/10.1029/2004JB003039

Bohannon, R. G., & Geist, E. (1998). Upper crustal structure and Neogene tectonic development of the California continental borderland. Geological Society of America Bulletin, 110(6), 779–800. https://doi.org/10.1130/0016-7606(1998)110<0779:UCSANT>2.3.CO;2

Bonnet, E., Bour, O., Odling, N. E., Davy, P., Main, I., Cowie, P., & Berkowitz, B. (2001). Scaling of fracture systems in geological media. Reviews of Geophysics, 39(3), 347–383. https://doi.org/10.1029/1999RG000074

Botter, C., Cardozo, N., Hardy, S., Lecomte, I., Paton, G., & Escalona, A. (2016). Seismic characterisation of fault damage in 3D using mechanical and seismic modelling. Marine and Petroleum Geology, 77, 973–990.

Boyd, D. (2020). Characterizing the Geometry, Kinematics, and Potential Connectivity at the Southern Termination of the Palos Verdes Fault. California State University, Long Beach.

Bramlette, M. N. (1946). The Monterey Formation of California and the origin of its siliceous rocks (Vol. 212). US Government Printing Office.

Brankman, C. M., & Shaw, J. H. (2009). Structural Geometry and Slip of the Palos Verdes Fault, Southern California: Implications for Earthquake Hazards. Bulletin

of the Seismological Society of America, 99(3), 1730–1745. https://doi.org/10.1785/0120080303

Brodsky, E. E., Mori, J. J., Anderson, L., Chester, F. M., Conin, M., Dunham, E. M., Eguchi, N., Fulton, P. M., Hino, R., Hirose, T., & others. (2020). The state of stress on the fault before, during, and after a major earthquake. Annual Review of Earth and Planetary Sciences, 48(1), 49–74.

Brothers, D. S., Conrad, J. E., Maier, K. L., Paull, C. K., McGann, M., & Caress, D. W. (2015). The Palos Verdes Fault offshore Southern California: Late Pleistocene to present tectonic geomorphology, seascape evolution, and slip rate estimate based on AUV and ROV surveys. Journal of Geophysical Research: Solid Earth, 120(7), 4734–4758. https://doi.org/10.1002/2015JB011938

Brudzinski, M. R., & Allen, R. M. (2007). Segmentation in episodic tremor and slip all along Cascadia. Geology, 35(10), 907. https://doi.org/10.1130/G23740A.1

Bürgmann, R. (2018). The geophysics, geology and mechanics of slow fault slip. Earth and Planetary Science Letters, 495, 112–134. https://doi.org/10.1016/j.epsl.2018.04.062

Bürgmann, R., Pollard, D. D., & Martel, S. J. (1994). Slip distributions on faults: Effects of stress gradients, inelastic deformation, heterogeneous host-rock stiffness, and fault interaction. Journal of Structural Geology, 16(12), 1675–1690.

Caine, J. S., Evans, J. P., & Forster, C. B. (1996). Fault zone architecture and permeability structure. Geology, 24(11), 1025. https://doi.org/10.1130/0091-7613(1996)024<1025:FZAAPS>2.3.CO;2

Cartwright, J. A., Trudgill, B. D., & Mansfield, C. S. (1995). Fault growth by segment linkage: An explanation for scatter in maximum displacement and trace length data from the Canyonlands Grabens of SE Utah. Journal of Structural Geology, 17(9), 1319–1326.

Chamberlain, C. J., Hopp, C. J., Boese, C. M., Warren-Smith, E., Chambers, D., Chu, S. X., Michailos, K., & Townend, J. (2018). EQcorrscan: Repeating and Near-Repeating Earthquake Detection and Analysis in Python. Seismological Research Letters, 89(1), 173–181. https://doi.org/10.1785/0220170151

Chaytor, J. D., Goldfinger, C., Dziak, R. P., & Fox, C. G. (2004). Active deformation of the Gorda plate: Constraining deformation models with new geophysical data. Geology, 32(4), 353. https://doi.org/10.1130/G20178.2

Chen, X., & McGuire, J. J. (2016). Measuring earthquake source parameters in the Mendocino triple junction region using a dense OBS array: Implications for fault strength variations. Earth and Planetary Science Letters, 453, 276–287. https://doi.org/10.1016/j.epsl.2016.08.022

Chester, F. M., & Chester, J. S. (2000). Stress and deformation along wavy frictional faults. Journal of Geophysical Research: Solid Earth, 105(B10), 23421–23430. https://doi.org/10.1029/2000JB900241

Chester, F. M., & Logan, J. M. (1986). Implications for mechanical properties of brittle faults from observations of the Punchbowl fault zone, California. Pure and Applied Geophysics PAGEOPH, 124(1–2), 79–106. https://doi.org/10.1007/BF00875720

Chester, J. S., Chester, F. M., & Kronenberg, A. K. (2005). Fracture surface energy of the Punchbowl fault, San Andreas system. Nature, 437(7055), 133–136. https://doi.org/10.1038/nature03942

Childs, C., Walsh, J., & Watterson, J. (1997). Complexity in fault zone structure and implications for fault seal prediction. In Norwegian petroleum society special publications (Vol. 7, pp. 61–72). Elsevier.

Choi, J.-H., Edwards, P., Ko, K., & Kim, Y.-S. (2016). Definition and classification of fault damage zones: A review and a new methodological approach. Earth-Science Reviews, 152, 70–87. https://doi.org/10.1016/j.earscirev.2015.11.006

Chopra, S., & Marfurt, K. (2008). Gleaning meaningful information from seismic attributes. 26, 11.

Chopra, S., & Marfurt, K. J. (2005). Seismic attributes—A historical perspective. Geophysics, 70(5), 3SO-28SO.

Cochran, E. S., Li, Y.-G., Shearer, P. M., Barbot, S., Fialko, Y., & Vidale, J. E. (2009). Seismic and geodetic evidence for extensive, long-lived fault damage zones. Geology, 37(4), 315–318. https://doi.org/10.1130/G25306A.1

Cowie, P. A., & Scholz, C. H. (1992a). Displacement-length scaling relationship for faults: Data synthesis and discussion. Journal of Structural Geology, 14(10), 1149–1156. https://doi.org/10.1016/0191-8141(92)90066-6

Cowie, P. A., & Scholz, C. H. (1992b). Physical explanation for the displacement-length relationship of faults using a post-yield fracture mechanics model. Journal of Structural Geology, 14(10), 1133–1148.

Cowie, P. A., & Shipton, Z. K. (1998). Fault tip displacement gradients and process zone dimensions. Journal of Structural Geology, 20(8), 983–997. https://doi.org/10.1016/S0191-8141(98)00029-7

Crouch, J. K., & Suppe, J. (1993). Late Cenozoic tectonic evolution of the Los Angeles basin and inner California borderland: A model for core complex-like crustal extension. Geological Society of America Bulletin, 105(11), 1415–1434.

Dawers, N. H., & Anders, M. H. (1995). Displacement-length scaling and fault linkage. Journal of Structural Geology, 17(5), 607–614.

DeMets, C., Gordon, R. G., & Argus, D. F. (2010). Geologically current plate motions. Geophysical Journal International, 181(1), 1–80.

Dieterich, J. (1994). A constitutive law for rate of earthquake production and its application to earthquake clustering. Journal of Geophysical Research: Solid Earth, 99(B2), 2601–2618. https://doi.org/10.1029/93JB02581

Dieterich, J. H. (1986). A model for the nucleation of earthquake slip. Earthquake Source Mechanics, 37, 37–47.

Dondurur, D. (2018). Acquisition and processing of marine seismic data. Elsevier.

Dooley, T., & McClay, K. (1997). Analog modeling of pull-apart basins. AAPG Bulletin, 81(11), 1804–1826.

Dooley, T. P., & Schreurs, G. (2012). Analogue modelling of intraplate strike-slip tectonics: A review and new experimental results. Tectonophysics, 574, 1–71.

Dragert, H. (2001). A Silent Slip Event on the Deeper Cascadia Subduction Interface. Science, 292(5521), 1525–1528. https://doi.org/10.1126/science.1060152

Dunham, E. M., Belanger, D., Cong, L., & Kozdon, J. E. (2011). Earthquake ruptures with strongly rate-weakening friction and off-fault plasticity, Part 1: Planar faults. Bulletin of the Seismological Society of America, 101(5), 2296–2307.

Efron, B., & Tibshirani, R. J. (1994). An introduction to the bootstrap. CRC press.

Ehman, K. D., Edwards, B. D., & Ponti, D. J. (2015). Sequence stratigraphic framework of upper pliocene to holocene sediments of the Los Angeles Basin, California: Implications for aquifer architecture. Pacific Section, SEPM, Society for Sedimentary Geology; USGS Publications Warehouse. http://pubs.er.usgs.gov/publication/70156831

Eichhubl, P., & Behl, R. J. (1998). Diagenesis, deformation, and fluid flow in the Miocene Monterey Formation.

Eichhubl, P., & Boles, J. R. (2000). Focused fluid flow along faults in the Monterey Formation, coastal California. GSA Bulletin, 112(11), 1667–1679.

Evans, J. R., Eberhart-Phillips, D., & Thurber, C. (1994). User's manual for SIMULPS12 for imaging vp and vp/vs; a derivative of the" Thurber" tomographic inversion SIMUL3 for local earthquakes and explosions. US Geological Survey,.

Faulkner, D. R., Jackson, C. A. L., Lunn, R. J., Schlische, R. W., Shipton, Z. K., Wibberley, C. A. J., & Withjack, M. O. (2010). A review of recent developments concerning the structure, mechanics and fluid flow properties of fault zones. Journal of Structural Geology, 32(11), 1557–1575. https://doi.org/10.1016/j.jsg.2010.06.009

Faulkner, D. R., Lewis, A. C., & Rutter, E. H. (2003). On the internal structure and mechanics of large strike-slip fault zones: Field observations of the Carboneras

fault in southeastern Spain. Tectonophysics, 367(3–4), 235–251. https://doi.org/10.1016/S0040-1951(03)00134-3

Faulkner, D. R., Mitchell, T. M., Jensen, E., & Cembrano, J. (2011). Scaling of fault damage zones with displacement and the implications for fault growth processes. Journal of Geophysical Research, 116(B5), B05403. https://doi.org/10.1029/2010JB007788

Fialko, Y. (2002). Deformation on Nearby Faults Induced by the 1999 Hector Mine Earthquake. Science, 297(5588), 1858–1862. https://doi.org/10.1126/science.1074671

Fialko, Y. (2004). Evidence of fluid-filled upper crust from observations of postseismic deformation due to the 1992 Mw7. 3 Landers earthquake. Journal of Geophysical Research: Solid Earth, 109(B8).

Fisher, M. A. (2004). The Offshore Palos Verdes Fault Zone near San Pedro, Southern California. Bulletin of the Seismological Society of America, 94(2), 506–530. https://doi.org/10.1785/0120030042

Fossen, H., & Tikoff, B. (1993). The deformation matrix for simultaneous simple shearing, pure shearing and volume change, and its application to transpression-transtension tectonics. Journal of Structural Geology, 15(3–5), 413–422.

Frank, W. B., & Brodsky, E. E. (2019). Daily measurement of slow slip from low-frequency earthquakes is consistent with ordinary earthquake scaling. Science Advances, 5(10), eaaw9386. https://doi.org/10.1126/sciadv.aaw9386

Frémont, M.-J., & Malone, S. D. (1987). High precision relative locations of earthquakes at Mount St. Helens, Washington. Journal of Geophysical Research: Solid Earth, 92(B10), 10223–10236. https://doi.org/10.1029/JB092iB10p10223

Gao, X., & Wang, K. (2017). Rheological separation of the megathrust seismogenic zone and episodic tremor and slip. Nature, 543(7645), 416–419. https://doi.org/10.1038/nature21389

Gazdag, J. (1978). Wave equation migration with the phase-shift method. Geophysics, 43(7), 1342–1351.

Geller, R. J., & Mueller, C. S. (1980). Four similar earthquakes in central California. Geophysical Research Letters, 7(10), 821–824. https://doi.org/10.1029/GL007i010p00821

Grossman, E., & Joachimski, M. (2020). Oxygen isotope stratigraphy. In Geologic Time Scale 2020 (pp. 279–307). Elsevier.

Gulick, S. P. S., Meltzer, A. S., Henstock, T. J., & Levander, A. (2001). Internal deformation of the southern Gorda plate: Fragmentation of a weak plate near the Mendocino triple junction. 4.

Gulley, A. K., Eccles, J. D., Kaipio, J. P., & Malin, P. E. (2017). The effect of gradational velocities and anisotropy on fault-zone trapped waves. Geophysical Journal International, 210(2), 964–978. https://doi.org/10.1093/gji/ggx200

Guo, H., Brodsky, E. E., Goebel, T. H. W., & Cladouhos, T. T. (2021a). Measuring Fault Zone and Host Rock Hydraulic Properties Using Tidal Responses. Geophysical Research Letters, 48(13). https://doi.org/10.1029/2021GL093986

Guo, H., Brodsky, E., Goebel, T., & Cladouhos, T. (2021b). Measuring fault zone and Host rock hydraulic properties using tidal responses. Geophysical Research Letters, 48(13), e2021GL093986.

Haines, J., Wallace, L. M., & Dimitrova, L. (2019). Slow Slip Event Detection in Cascadia Using Vertical Derivatives of Horizontal Stress Rates. Journal of Geophysical Research: Solid Earth, 2018JB016898. https://doi.org/10.1029/2018JB016898

Hale, D. (2009). Structure-oriented smoothing and semblance. CWP Report, 635(635).

Hale, D. (2013). Methods to compute fault images, extract fault surfaces, and estimate fault throws from 3D seismic images. GEOPHYSICS, 78(2), O33–O43. https://doi.org/10.1190/geo2012-0331.1

Hardebeck, J. L. (2002). A New Method for Determining First-Motion Focal Mechanisms. Bulletin of the Seismological Society of America, 92(6), 2264–2276. https://doi.org/10.1785/0120010200

Harding, T. P. (1985). Seismic characteristics and identification of negative flower structures, positive flower structures, and positive structural inversion. AAPG Bulletin, 69(4), 582–600.

Heimann, S., Kriegerowski, M., Isken, M., Cesca, S., Daout, S., Grigoli, F., Juretzek, C., Megies, T., Nooshiri, N., Steinberg, A., & others. (2017). Pyrocko-An open-source seismology toolbox and library.

Hobbs, D. W. (1967). The Formation of Tension Joints in Sedimentary Rocks: An Explanation. Geological Magazine, 104(6), 550–556. https://doi.org/10.1017/S0016756800050226

Hole, J. A., Beaudoin, B. C., & Klemperer, S. L. (2000). Vertical extent of the newborn San Andreas fault at the Mendocino triple junction. 4.

Holtkamp, S. G., & Brudzinski, M. R. (2011). Earthquake swarms in circum-Pacific subduction zones. Earth and Planetary Science Letters, 305(1–2), 215–225. https://doi.org/10.1016/j.epsl.2011.03.004

Huang, Y., Ampuero, J.-P., & Helmberger, D. V. (2014). Earthquake ruptures modulated by waves in damaged fault zones. Journal of Geophysical Research: Solid Earth, 119(4), 3133–3154.

Hubbard, J., Shaw, J. H., Dolan, J., Pratt, T. L., McAuliffe, L., & Rockwell, T. K. (2014). Structure and Seismic Hazard of the Ventura Avenue Anticline and Ventura Fault, California: Prospect for Large, Multisegment Ruptures in the Western Transverse Ranges. Bulletin of the Seismological Society of America, 104(3), 1070–1087. https://doi.org/10.1785/0120130125

Hubbert, M. K., & Rubey, W. W. (1959). Role of fluid pressure in mechanics of overthrust faultingi. Mechanics of fluid-filled porous solids and its application to overthrust faulting. GSA Bulletin, 70(2), 115–166.

Hyndman, R. D. (2013). Downdip landward limit of Cascadia great earthquake rupture: CASCADIA GREAT EARTHQUAKE RUPTURE LIMIT. Journal of Geophysical Research: Solid Earth, 118(10), 5530–5549. https://doi.org/10.1002/jgrb.50390

Iacopini, D., Butler, R. W. H., Purves, S., McArdle, N., & De Freslon, N. (2016). Exploring the seismic expression of fault zones in 3D seismic volumes. Journal of Structural Geology, 89, 54–73. https://doi.org/10.1016/j.jsg.2016.05.005

Igarashi, T., Matsuzawa, T., & Hasegawa, A. (2003). Repeating earthquakes and interplate aseismic slip in the northeastern Japan subduction zone: REPEATING EARTHQUAKES AND ASEISMIC SLIP. Journal of Geophysical Research: Solid Earth, 108(B5). https://doi.org/10.1029/2002JB001920

Kame, N., Rice, J. R., & Dmowska, R. (2003). Effects of prestress state and rupture velocity on dynamic fault branching. Journal of Geophysical Research: Solid Earth, 108(B5).

Ke, C.-Y., McLaskey, G. C., & Kammer, D. S. (2022). Earthquake breakdown energy scaling despite constant fracture energy. Nature Communications, 13(1), 1005.

Keren, T. T., & Kirkpatrick, J. D. (2016). The damage is done: Low fault friction recorded in the damage zone of the shallow Japan Trench décollement. Journal of Geophysical Research: Solid Earth, 121(5), 3804–3824. https://doi.org/10.1002/2015JB012311

Kim, Y.-S., & Sanderson, D. J. (2005). The relationship between displacement and length of faults: A review. Earth-Science Reviews, 68(3–4), 317–334. https://doi.org/10.1016/j.earscirev.2004.06.003

Kluesner, J., Brothers, D., Hart, P., Miller, N., & Hatcher, G. (2019). Practical approaches to maximizing the resolution of sparker seismic reflection data. Marine Geophysical Research, 40(3), 279–301. https://doi.org/10.1007/s11001-018-9367-2

Kluesner, J. W., & Brothers, D. S. (2016). Seismic attribute detection of faults and fluid pathways within an active strike-slip shear zone: New insights from high-resolution 3D P-Cable™ seismic data along the Hosgri Fault, offshore California. Interpretation, 4(1), SB131–SB148. https://doi.org/10.1190/INT-2015-0143.1

Kluesner, J. W., Silver, E. A., Bangs, N. L., McIntosh, K. D., Gibson, J., Orange, D., Ranero, C. R., & Von Huene, R. (2013). High density of structurally controlled, shallow to deep water fluid seep indicators imaged offshore Costa Rica. Geochemistry, Geophysics, Geosystems, 14(3), 519–539.

Kurzon, I., Vernon, F. L., Ben-Zion, Y., & Atkinson, G. (2014). Ground motion prediction equations in the San Jacinto fault zone: Significant effects of rupture directivity and fault zone amplification. Pure and Applied Geophysics, 171, 3045–3081.

Lapusta, N., & Rice, J. R. (2003). Nucleation and early seismic propagation of small and large events in a crustal earthquake model: NUCLEATION AND EARLY SEISMIC PROPAGATION. Journal of Geophysical Research: Solid Earth, 108(B4). https://doi.org/10.1029/2001JB000793

Lay, T., Kanamori, H., Ammon, C. J., Koper, K. D., Hutko, A. R., Ye, L., Yue, H., & Rushing, T. M. (2012). Depth-varying rupture properties of subduction zone megathrust faults. Journal of Geophysical Research: Solid Earth, 117(B4).

Lay, T., Liu, C., & Kanamori, H. (2019). Enhancing Tsunami Warning Using P Wave Coda. Journal of Geophysical Research: Solid Earth, 124(10), 10583–10609. https://doi.org/10.1029/2019JB018221

Lewis, M. A., & Ben-Zion, Y. (2010). Diversity of fault zone damage and trapping structures in the Parkfield section of the San Andreas Fault from comprehensive analysis of near fault seismograms: Diversity of fault zone damage at Parkfield. Geophysical Journal International, 183(3), 1579–1595. https://doi.org/10.1111/j.1365-246X.2010.04816.x

Li, S., Freymueller, J., & McCaffrey, R. (2016). Slow slip events and time-dependent variations in locking beneath Lower Cook Inlet of the Alaska-Aleutian subduction zone. Journal of Geophysical Research: Solid Earth, 121(2), 1060–1079. https://doi.org/10.1002/2015JB012491

Li, S., Wang, K., Wang, Y., Jiang, Y., & Dosso, S. E. (2018). Geodetically Inferred Locking State of the Cascadia Megathrust Based on a Viscoelastic Earth Model. Journal of Geophysical Research: Solid Earth, 123(9), 8056–8072. https://doi.org/10.1029/2018JB015620

Li, Y., Catchings, R. D., & Goldman, M. R. (2016). Subsurface Fault Damage Zone of the 2014 M w 6.0 South Napa, California, Earthquake Viewed from Fault-Zone Trapped Waves. Bulletin of the Seismological Society of America, 106(6), 2747–2763. https://doi.org/10.1785/0120160039

Li, Y.-G., Ellsworth, W. L., Thurber, C. H., Malin, P. E., & Aki, K. (n.d.). Fault-Zone Guided Waves from Explosions in the San Andreas Fault at Parkfield and Cienega Valley, California. 12.

Li, Y.-G., Ellsworth, W. L., Thurber, C. H., Malin, P. E., & Aki, K. (1997). Fault-zone guided waves from explosions in the San Andreas fault at Parkfield and

Cienega Valley, California. Bulletin of the Seismological Society of America, 87(1), 210–221.

Li, Y.-G., Vidale, J. E., & Cochran, E. S. (2004). Low-velocity damaged structure of the San Andreas Fault at Parkfield from fault zone trapped waves: LOW-VELOCITY DAMAGED STRUCTURE OF THE SAN ANDREAS FAULT. Geophysical Research Letters, 31(12), n/a-n/a. https://doi.org/10.1029/2003GL019044

Liao, Z., Hu, L., Huang, X., Carpenter, B. M., Marfurt, K. J., Vasileva, S., & Zhou, Y. (2020). Characterizing damage zones of normal faults using seismic variance in the Wangxuzhuang oilfield, China. Interpretation, 8(4), SP53–SP60.

Liao, Z., Liu, H., Carpenter, B. M., Marfurt, K. J., & Reches, Z. (2019). Analysis of fault damage zones using three-dimensional seismic coherence in the Anadarko Basin, Oklahoma. AAPG Bulletin, 103(8), 1771–1785.

Lindsey, E. O., Mallick, R., Hubbard, J. A., Bradley, K. E., Almeida, R. V., Moore, J. D. P., Bürgmann, R., & Hill, E. M. (2021). Slip rate deficit and earthquake potential on shallow megathrusts. Nature Geoscience, 14(5), 321–326. https://doi.org/10.1038/s41561-021-00736-x

Lohman, R. B., & McGuire, J. J. (2007). Earthquake swarms driven by aseismic creep in the Salton Trough, California: OBSIDIAN BUTTES SWARM. Journal of Geophysical Research: Solid Earth, 112(B4). https://doi.org/10.1029/2006JB004596

Ma, D.-B., Wu, G.-H., Scarselli, N., Luo, X.-S., Han, J.-F., & Chen, Z.-Y. (2019). Seismic damage zone and width–throw scaling along the strike-slip faults in the Ordovician carbonates in the Tarim Basin. Petroleum Science, 16(4), 752–762.

Manighetti, I., Campillo, M., Sammis, C., Mai, P., & King, G. (2005). Evidence for self-similar, triangular slip distributions on earthquakes: Implications for earthquake and fault mechanics. Journal of Geophysical Research: Solid Earth, 110(B5).

Manighetti, I., King, G., & Sammis, C. G. (2004). The role of off-fault damage in the evolution of normal faults. Earth and Planetary Science Letters, 217(3–4), 399–408.

Mann, P. (2007). Global catalogue, classification and tectonic origins of restraining- and releasing bends on active and ancient strike-slip fault systems. Geological Society, London, Special Publications, 290(1), 13–142.

Marfurt, K. J., Kirlin, R. L., Farmer, S. L., & Bahorich, M. S. (1998a). 3-D seismic attributes using a semblance-based coherency algorithm. Geophysics, 63(4), 1150–1165.

Marfurt, K. J., Kirlin, R. L., Farmer, S. L., & Bahorich, M. S. (1998b). 3-D seismic attributes using a semblance-based coherency algorithm. GEOPHYSICS, 63(4), 1150–1165. https://doi.org/10.1190/1.1444415

Martel, S. J., & Pollard, D. D. (1989). Mechanics of slip and fracture along small faults and simple strike-slip fault zones in granitic rock. Journal of Geophysical Research, 94(B7), 9417. https://doi.org/10.1029/JB094iB07p09417

Materna, K., Bartlow, N., Wech, A., Williams, C., & Bürgmann, R. (2019). Dynamically Triggered Changes of Plate Interface Coupling in Southern Cascadia. Geophysical Research Letters, 46(22), 12890–12899. https://doi.org/10.1029/2019GL084395

Materna, K., & Bürgmann, R. (2016). Contrasts in compliant fault zone properties inferred from geodetic measurements in the San Francisco Bay area. Journal of Geophysical Research: Solid Earth, 121(9), 6916–6931. https://doi.org/10.1002/2016JB013243

Materna, K., Taira, T., & Bürgmann, R. (2018). Aseismic Transform Fault Slip at the Mendocino Triple Junction From Characteristically Repeating Earthquakes. Geophysical Research Letters, 45(2), 699–707. https://doi.org/10.1002/2017GL075899

McCaffrey, R., Qamar, A. I., King, R. W., Wells, R., Khazaradze, G., Williams, C. A., Stevens, C. W., Vollick, J. J., & Zwick, P. C. (2007). Fault locking, block rotation and crustal deformation in the Pacific Northwest. Geophysical Journal International, 169(3), 1315–1340. https://doi.org/10.1111/j.1365-246X.2007.03371.x

McClay, K., & Bonora, M. (2001). Analog models of restraining stepovers in strike-slip fault systems. AAPG Bulletin, 85(2), 233–260.

McCrory, P. A., Blair, J. L., Waldhauser, F., & Oppenheimer, D. H. (2012). Juan de Fuca slab geometry and its relation to Wadati-Benioff zone seismicity: JDF SLAB GEOMETRY AND WBZ SEISMICITY. Journal of Geophysical Research: Solid Earth, 117(B9). https://doi.org/10.1029/2012JB009407

McNeilan, T. W., Rockwell, T. K., & Resnick, G. S. (1996). Style and rate of Holocene slip, Palos Verdes fault, southern California. Journal of Geophysical Research: Solid Earth, 101(B4), 8317–8334. https://doi.org/10.1029/95JB02251

Merrill, R., & Bostock, M. (n.d.). An Earthquake Nest in Cascadia. 15.

Michel, S., Gualandi, A., & Avouac, J.-P. (2019). Interseismic Coupling and Slow Slip Events on the Cascadia Megathrust. Pure and Applied Geophysics, 176(9), 3867–3891. https://doi.org/10.1007/s00024-018-1991-x

Miller, S. A., Collettini, C., Chiaraluce, L., Cocco, M., Barchi, M., & Kaus, B. J. P. (2004). Aftershocks driven by a high-pressure CO2 source at depth. Nature, 427(6976), 724–727. https://doi.org/10.1038/nature02251

Milliner, C., Donnellan, A., Aati, S., Avouac, J.-P., Zinke, R., Dolan, J. F., Wang, K., & Bürgmann, R. (2021). Bookshelf kinematics and the effect of dilatation on fault zone inelastic deformation: Examples from optical image correlation measurements of the 2019 Ridgecrest earthquake sequence. Journal of Geophysical Research: Solid Earth, 126(3), e2020JB020551.

Mitchell, T. M., & Faulkner, D. R. (2009). The nature and origin of off-fault damage surrounding strike-slip fault zones with a wide range of displacements: A field study from the Atacama fault system, northern Chile. Journal of Structural Geology, 31(8), 802–816. https://doi.org/10.1016/j.jsg.2009.05.002

Mogi, K. (1963). Some discussions on aftershocks, foreshocks and earthquake swarms-the fracture of a semi finite body caused by an inner stress origin and its relation to the earthquake phenomena. Bull. Earthq. Res. Inst., 41, 615–658.

Mynatt, I., Bergbauer, S., & Pollard, D. D. (2007). Using differential geometry to describe 3-D folds. Journal of Structural Geology, 29(7), 1256–1266.

Nabavi, S. T., & Fossen, H. (2021). Fold geometry and folding–a review. Earth-Science Reviews, 222, 103812.

Nadeau, R. M. (2004). Periodic Pulsing of Characteristic Microearthquakes on the San Andreas Fault. Science, 303(5655), 220–222. https://doi.org/10.1126/science.1090353

Narr, W., & Suppe, J. (1991). Joint spacing in sedimentary rocks. Journal of Structural Geology, 13(9), 1037–1048. https://doi.org/10.1016/0191-8141(91)90055-N

Naylor, M., Mandl, G. t, & Supesteijn, C. (1986). Fault geometries in basement-induced wrench faulting under different initial stress states. Journal of Structural Geology, 8(7), 737–752.

Nishikawa, T., & Ide, S. (2017). Detection of earthquake swarms at subduction zones globally: Insights into tectonic controls on swarm activity: Detection of Earthquake Swarms. Journal of Geophysical Research: Solid Earth, 122(7), 5325–5343. https://doi.org/10.1002/2017JB014188

Nuyen, C., & Schmidt, D. A. (2021). Filling the Gap in Cascadia: The Emergence of Low-Amplitude Long-Term Slow Slip. Geochemistry, Geophysics, Geosystems. https://doi.org/10.1029/2020GC009477

Pavlis, G. L., Vernon, F., Harvey, D., & Quinlan, D. (2004). The generalized earthquake-location (GENLOC) package: An earthquake-location library. Computers & Geosciences, 30(9–10), 1079–1091. https://doi.org/10.1016/j.cageo.2004.06.010

Plesch, A., Shaw, J. H., Benson, C., Bryant, W. A., Carena, S., Cooke, M., Dolan, J., Fuis, G., Gath, E., Grant, L., Hauksson, E., Jordan, T., Kamerling, M., Legg, M., Lindvall, S., Magistrale, H., Nicholson, C., Niemi, N., Oskin, M., … Yeats, R.

(2007). Community Fault Model (CFM) for Southern California. Bulletin of the Seismological Society of America, 97(6), 1793–1802. https://doi.org/10.1785/0120050211

Pollard, D., Segall, P., & Atkinson, B. (1987). Fracture mechanics of rock. In Theoretical Displacements and Stresses near Fractures in Rock: With Applications to Faults, Joints, Veins, Dikes, and Solution Surfaces (pp. 277–349). Academic Press.

Pollitz, F. F., & Evans, E. L. (2017). Implications of the earthquake cycle for inferring fault locking on the Cascadia megathrust. Geophysical Journal International, ggx009. https://doi.org/10.1093/gji/ggx009

Ponti, D. J., Ehman, K. D., Edwards, B. D., Tinsley, J., Hildenbrand, T., Hillhouse, J. W., Hanson, R. T., McDougall, K., Powell, C. L., Wan, E., & others. (2007). A 3-dimensional model of water-bearing sequences in the Dominguez Gap region, Long Beach, California. US Geol Surv Open-File Rep, 1013.

Prieto, G. A., Beroza, G. C., Barrett, S. A., López, G. A., & Florez, M. (2012). Earthquake nests as natural laboratories for the study of intermediate-depth earthquake mechanics. Tectonophysics, 570–571, 42–56. https://doi.org/10.1016/j.tecto.2012.07.019

Prouty, N. G., Brothers, D. S., Kluesner, J. W., Barrie, J. V., Andrews, B. D., Lauer, R. M., Greene, H. G., Conrad, J. E., Lorenson, T. D., Law, M. D., & others. (2020). Focused fluid flow and methane venting along the Queen Charlotte fault, offshore Alaska (USA) and British Columbia (Canada). Geosphere, 16(6), 1336–1357.

Qiu, H., Ben-Zion, Y., Catchings, R., Goldman, M. R., Allam, A. A., & Steidl, J. (2021). Seismic imaging of the Mw 7.1 Ridgecrest earthquake rupture zone from data recorded by dense linear arrays. Journal of Geophysical Research: Solid Earth, 126(7), e2021JB022043.

Rigor, A. W. (2003). Structure and deformation of the Palos Verdes fault in San Pedro Bay, California [PhD Thesis]. San Diego State University.

Roberts, A. (2001). Curvature attributes and their application to 3 D interpreted horizons. First Break, 19(2), 85–100.

Rodriguez Padilla, A. M., Oskin, M. E., Milliner, C. W., & Plesch, A. (2022). Accrual of widespread rock damage from the 2019 Ridgecrest earthquakes. Nature Geoscience, 15(3), 222–226.

Roland, E., & McGuire, J. J. (2009). Earthquake swarms on transform faults. Geophysical Journal International, 178(3), 1677–1690. https://doi.org/10.1111/j.1365-246X.2009.04214.x

Ross, Z. E., Cochran, E. S., Trugman, D. T., & Smith, J. D. (2020). 3D fault architecture controls the dynamism of earthquake swarms. Science, 368(6497), 1357–1361. https://doi.org/10.1126/science.abb0779

Rouet-Leduc, B., Hulbert, C., & Johnson, P. A. (2019). Continuous chatter of the Cascadia subduction zone revealed by machine learning. Nature Geoscience, 12(1), 75–79. https://doi.org/10.1038/s41561-018-0274-6

Rudebusch, J. A., Prouty, N. G., Conrad, J. E., Watt, J. T., Kluesner, J., Hill, J. C., Miller, N. C., Watson, S. J., & Hillman, J. I. (2023). Diving Deeper Into Seep Distribution Along the Cascadia Convergent Margin, USA. Frontiers in Earth Science, 11, 1205211.

Sagy, A., & Brodsky, E. E. (2009). Geometric and rheological asperities in an exposed fault zone. Journal of Geophysical Research, 114(B2), B02301. https://doi.org/10.1029/2008JB005701

Sanderson, D. J., & Marchini, W. (1984). Transpression. Journal of Structural Geology, 6(5), 449–458.

Satake, K., Wang, K., & Atwater, B. F. (2003). Fault slip and seismic moment of the 1700 Cascadia earthquake inferred from Japanese tsunami descriptions. Journal of Geophysical Research: Solid Earth, 108(B11). https://doi.org/10.1029/2003JB002521

Savage, H. M., & Brodsky, E. E. (2011). Collateral damage: Evolution with displacement of fracture distribution and secondary fault strands in fault damage zones. Journal of Geophysical Research, 116(B3). https://doi.org/10.1029/2010JB007665

Schmalzle, G. M., McCaffrey, R., & Creager, K. C. (2014). Central Cascadia subduction zone creep. Geochemistry, Geophysics, Geosystems, 15(4), 1515–1532. https://doi.org/10.1002/2013GC005172

Scholz, C. H., Dawers, N. H., Yu, J.-Z., Anders, M. H., & Cowie, P. A. (1993). Fault growth and fault scaling laws: Preliminary results. Journal of Geophysical Research: Solid Earth, 98(B12), 21951–21961. https://doi.org/10.1029/93JB01008

Schwartz, S. Y., & Rokosky, J. M. (2007). Slow slip events and seismic tremor at circum-Pacific subduction zones. Reviews of Geophysics, 45(3).

Scott, C. P., Arrowsmith, J. R., Nissen, E., Lajoie, L., Maruyama, T., & Chiba, T. (2018). The M 7 2016 Kumamoto, Japan, Earthquake: 3-D Deformation Along the Fault and Within the Damage Zone Constrained From Differential Lidar Topography. Journal of Geophysical Research: Solid Earth, 123(7), 6138–6155. https://doi.org/10.1029/2018JB015581

Segall, P. (2010). Earthquake and volcano deformation. Princeton University Press.

Segall, P., & Bradley, A. M. (2012). Slow-slip evolves into megathrust earthquakes in 2D numerical simulations. Geophysical Research Letters, 39(18).

Segall, P., & Pollard, D. (1980). Mechanics of discontinuous faults. Journal of Geophysical Research: Solid Earth, 85(B8), 4337–4350.

Shaddox, H. R., & Schwartz, S. Y. (2019). Subducted seamount diverts shallow slow slip to the forearc of the northern Hikurangi subduction zone, New Zealand. Geology, 47(5), 415–418. https://doi.org/10.1130/G45810.1

Shaw, J. H., & Suppe, J. (1996). Earthquake hazards of active blind-thrust faults under the central Los Angeles basin, California. Journal of Geophysical Research: Solid Earth, 101(B4), 8623–8642. https://doi.org/10.1029/95JB03453

Shelly, D. R., Beroza, G. C., & Ide, S. (2007). Non-volcanic tremor and low-frequency earthquake swarms. Nature, 446(7133), 305–307. https://doi.org/10.1038/nature05666

Sheriff, R. E., & Geldart, L. P. (1995). Exploration seismology. Cambridge university press.

Shipton, Z. K., & Cowie, P. A. (2001). Damage zone and slip-surface evolution over mm to km scales in high-porosity Navajo sandstone, Utah. Journal of Structural Geology, 20.

Shipton, Z. K., & Cowie, P. A. (2003). A conceptual model for the origin of fault damage zone structures in high-porosity sandstone. Journal of Structural Geology, 25(3), 333–344. https://doi.org/10.1016/S0191-8141(02)00037-8

Shipton, Z. K., Soden, A. M., Kirkpatrick, J. D., Bright, A. M., & Lunn, R. J. (2006). How thick is a fault? Fault displacement-thickness scaling revisited. In R. Abercrombie, A. McGarr, H. Kanamori, & G. Di Toro (Eds.), Geophysical Monograph Series (Vol. 170, pp. 193–198). American Geophysical Union. https://doi.org/10.1029/170GM19

Sorlien, C. C., Seeber, L., Broderick, K. G., Luyendyk, B. P., Fisher, M. A., Sliter, R. W., & Normark, W. R. (2013). The Palos Verdes anticlinorium along the Los Angeles, California coast: Implications for underlying thrust faulting: PALOS VERDES ANTICLINORIUM CALIFORNIA. Geochemistry, Geophysics, Geosystems, 14(6), 1866–1890. https://doi.org/10.1002/ggge.20112

Spudich, P., & Olsen, K. (2001). Fault zone amplified waves as a possible seismic hazard along the Calaveras fault in central California. Geophysical Research Letters, 28(13), 2533–2536.

Stone, I., Vidale, J. E., Han, S., & Roland, E. (2018). Catalog of Offshore Seismicity in Cascadia: Insights Into the Regional Distribution of Microseismicity and its Relation to Subduction Processes. Journal of Geophysical Research: Solid Earth, 123(1), 641–652. https://doi.org/10.1002/2017JB014966

Suess, E. (2020). Marine cold seeps: Background and recent advances. Hydrocarbons, Oils and Lipids: Diversity, Origin, Chemistry and Fate, 747–767.

Sylvester, A. G. (1988). Strike-slip faults. Geological Society of America Bulletin, 100(11), 1666–1703.

Tada, H., Paris, P. C., & Irwin, G. R. (1973). The stress analysis of cracks. Handbook, Del Research Corporation, 34(1973).

Teran, O. J., Fletcher, J. M., Oskin, M. E., Rockwell, T. K., Hudnut, K. W., Spelz, R. M., Akciz, S. O., Hernandez-Flores, A. P., & Morelan, A. E. (2015). Geologic and structural controls on rupture zone fabric: A field-based study of the 2010 Mw 7.2 El Mayor–Cucapah earthquake surface rupture. Geosphere, 11(3), 899–920.

Thakur, P., Huang, Y., & Kaneko, Y. (2020). Effects of low-velocity fault damage zones on long-term earthquake behaviors on mature strike-slip faults. Journal of Geophysical Research: Solid Earth. https://doi.org/10.1029/2020JB019587

Thurber, C., Roecker, S., Ellsworth, W., Chen, Y., Lutter, W., & Sessions, R. (1997). Two-dimensional seismic image of the San Andreas Fault in the Northern Gabilan Range, central California: Evidence for fluids in the fault zone. Geophysical Research Letters, 24(13), 1591–1594. https://doi.org/10.1029/97GL01435

Tingdahl, K. M., & De Rooij, M. (2005). Semi-automatic detection of faults in 3D seismic data. Geophysical Prospecting, 53(4), 533–542.

Toomey, D., Allen, R., Barclay, A., Bell, S., Bromirski, P., Carlson, R., Chen, X., Collins, J., Dziak, R., Evers, B., Forsyth, D., Gerstoft, P., Hooft, E., Livelybrooks, D., Lodewyk, J., Luther, D., McGuire, J., Schwartz, S., Tolstoy, M., … Wilcock, W. (2014). The Cascadia Initiative: A Sea Change In Seismological Studies of Subduction Zones. Oceanography, 27(2), 138–150. https://doi.org/10.5670/oceanog.2014.49

Torabi, A., Alaei, B., & Kolyukhin, D. (2017). Analysis of fault scaling relations using fault seismic attributes: Analysis of fault scaling relations. Geophysical Prospecting, 65(2), 581–595. https://doi.org/10.1111/1365-2478.12440

Torabi, A., & Berg, S. S. (2011). Scaling of fault attributes: A review. Marine and Petroleum Geology, 28(8), 1444–1460. https://doi.org/10.1016/j.marpetgeo.2011.04.003

Tréhu, A. M., Torres, M. E., Moore, G. F., Suess, E., & Bohrmann, G. (1999). Temporal and spatial evolution of a gas hydrate–bearing accretionary ridge on the Oregon continental margin. Geology, 27(10), 939–942.

Triezenberg, P., Hart, P., & Childs, J. (2016). National Archive of Marine Seismic Surveys (NAMSS)—A USGS data website of marineseismic reflection data within the U.S. exclusive economic zone (EEZ). U.S. Geological Survey. https://walrus.wr.usgs.gov/NAMSS/

Trugman, D. T., & Shearer, P. M. (2017). GrowClust: A Hierarchical Clustering Algorithm for Relative Earthquake Relocation, with Application to the Spanish

Springs and Sheldon, Nevada, Earthquake Sequences. Seismological Research Letters, 88(2A), 379–391. https://doi.org/10.1785/0220160188

Uchida, N., Takagi, R., Asano, Y., & Obara, K. (2020). Migration of shallow and deep slow earthquakes toward the locked segment of the Nankai megathrust. Earth and Planetary Science Letters, 531, 115986.

Verschuur, D. J., Berkhout, A., & Wapenaar, C. (1992). Adaptive surface-related multiple elimination. Geophysics, 57(9), 1166–1177.

Vidale, J. E., & Li, Y.-G. (2003). Damage to the shallow Landers fault from the nearby Hector Mine earthquake. Nature, 421(6922), 524–526. https://doi.org/10.1038/nature01354

Vidale, J. E., & Shearer, P. M. (2006). A survey of 71 earthquake bursts across southern California: Exploring the role of pore fluid pressure fluctuations and aseismic slip as drivers: SEISMICITY BURSTS IN SOUTHERN CALIFORNIA. Journal of Geophysical Research: Solid Earth, 111(B5), n/a-n/a. https://doi.org/10.1029/2005JB004034

Walter, J. I., Schwartz, S. Y., Protti, M., & Gonzalez, V. (2013). The synchronous occurrence of shallow tremor and very low frequency earthquakes offshore of the Nicoya Peninsula, Costa Rica. Geophysical Research Letters, 40(8), 1517–1522.

Walton, M. A. L., Staisch, L. M., Dura, T., Pearl, J. K., Sherrod, B., Gomberg, J., Engelhart, S., Tréhu, A., Watt, J., Perkins, J., Witter, R. C., Bartlow, N., Goldfinger, C., Kelsey, H., Morey, A. E., Sahakian, V. J., Tobin, H., Wang, K., Wells, R., & Wirth, E. (2021). Toward an Integrative Geological and Geophysical View of Cascadia Subduction Zone Earthquakes. Annual Review of Earth and Planetary Sciences, 49(1), annurev-earth-071620-065605. https://doi.org/10.1146/annurev-earth-071620-065605

Walton, M., Papesh, A., Johnson, S., & Brothers, D. (2020). Quaternary faults offshore of California. U.S. Geological Survey Data Release. https://doi.org/10.5066/P91RYEZ4

Wang, K., & Tréhu, A. M. (2016). Invited review paper: Some outstanding issues in the study of great megathrust earthquakes—The Cascadia example. Journal of Geodynamics, 98, 1–18. https://doi.org/10.1016/j.jog.2016.03.010

Ward, S. N., & Valensise, G. (1994). The Palos Verdes terraces, California: Bathtub rings from a buried reverse fault. Journal of Geophysical Research: Solid Earth, 99(B3), 4485–4494. https://doi.org/10.1029/93JB03362

Webb, T. H., & Kanamori, H. (1985). EARTHQUAKE FOCAL MECHANISMS IN THE EASTERN TRANSVERSE RANGES AND SAN EMIGDIO MOUNTAINS, SOUTHERN CALIFORNIA AND EVIDENCE FOR A REGIONAL DECOLLEMENT. 21.

White, M. C., Fang, H., Catchings, R. D., Goldman, M. R., Steidl, J. H., & Ben-Zion, Y. (2021). Detailed traveltime tomography and seismic catalogue around the 2019 M w7. 1 Ridgecrest, California, earthquake using dense rapid-response seismic data. Geophysical Journal International, 227(1), 204–227.

Wilson, J. E., Chester, J. S., & Chester, F. M. (2003). Microfracture analysis of fault growth and wear processes, Punchbowl Fault, San Andreas system, California. Journal of Structural Geology, 25(11), 1855–1873. https://doi.org/10.1016/S0191-8141(03)00036-1

Wolfe, F. D., Shaw, J. H., & Plesch, A. (2022). Origin of the Palos Verdes Restraining Bend and Its Implications for the 3D Geometry of the Fault and Earthquake Hazards in Los Angeles, California. Bulletin of the Seismological Society of America, 112(5), 2689–2714.

Wong, T. (1982). Shear fracture energy of Westerly granite from post-failure behavior. Journal of Geophysical Research: Solid Earth, 87(B2), 990–1000. https://doi.org/10.1029/JB087iB02p00990

Wright, T. (1991). Active margin basins. In American Association of Petroleum Geologists Memoir 52 (pp. 35–134).

Wu, C., Peng, Z., & Ben-Zion, Y. (2009). Non-linearity and temporal changes of fault zone site response associated with strong ground motion. Geophysical Journal International, 176(1), 265–278.

Wu, J., Hole, J. A., Snoke, J. A., & Imhof, M. G. (2008). Depth extent of the fault-zone seismic waveguide: Effects of increasing velocity with depth. Geophysical Journal International, 173(2), 611–622. https://doi.org/10.1111/j.1365-246X.2008.03755.x

Xu, X., Liu, D., & Lavier, L. (2023). Constraining fault damage zone properties from geodesy: A case study near the 2019 Ridgecrest earthquake sequence. Geophysical Research Letters, 50(5), e2022GL101692.

Xue, L., Bürgmann, R., Shelly, D. R., Johnson, C. W., & Taira, T. (2018). Kinematics of the 2015 San Ramon, California earthquake swarm: Implications for fault zone structure and driving mechanisms. Earth and Planetary Science Letters, 489, 135–144. https://doi.org/10.1016/j.epsl.2018.02.018

Yang, H., Li, Z., Peng, Z., Ben-Zion, Y., & Vernon, F. (2014). Low-velocity zones along the San Jacinto Fault, Southern California, from body waves recorded in dense linear arrays: Damage zones of the San Jacinto Fault. Journal of Geophysical Research: Solid Earth, 119(12), 8976–8990. https://doi.org/10.1002/2014JB011548

Yang, H., Zhu, L., & Cochran, E. S. (2011). Seismic structures of the Calico fault zone inferred from local earthquake travel time modelling: Seismic structures of the Calico fault zone. Geophysical Journal International, 186(2), 760–770. https://doi.org/10.1111/j.1365-246X.2011.05055.x

Yeats, R. S., & Beall, J. M. (1991). Stratigraphic Controls of Oil Fields in the Los Angeles Basin A Guide to Migration History: Chapter 7.
Yilmaz, Ö. (2001). Seismic data analysis: Processing, inversion, and interpretation of seismic data. Society of exploration geophysicists.